

REVIEW ARTICLE

Phase-field-crystal models for condensed matter dynamics on atomic length and diffusive time scales: an overview

Heike Emmerich^{a*}, Hartmut Löwen^{b*}, Raphael Wittkowski^b, Thomas Gruhn^a, Gyula I. Tóth^c,
György Tegze^c and László Gránásy^{c,d*}

^aLehrstuhl für Material- und Prozesssimulation, Universität Bayreuth, D-95440 Bayreuth, Germany;

^bInstitut für Theoretische Physik II, Weiche Materie, Heinrich-Heine-Universität Düsseldorf, D-40225

Düsseldorf, Germany; ^cInstitute for Solid State Physics and Optics, Wigner Research Centre for Physics, PO Box 49, H-1525 Budapest, Hungary; ^dBCAST, Brunel University, Uxbridge, Middlesex UB8 3PH, UK

(Received 27 June 2012; final version received 18 September 2012)

Here, we review the basic concepts and applications of the *phase-field-crystal* (PFC) method, which is one of the latest simulation methodologies in materials science for problems, where atomic- and microscales are tightly coupled. The PFC method operates on atomic length and diffusive time scales, and thus constitutes a computationally efficient alternative to molecular simulation methods. Its intense development in materials science started fairly recently following the work by Elder *et al.* [Phys. Rev. Lett. 88 (2002), p. 245701]. Since these initial studies, dynamical density functional theory and thermodynamic concepts have been linked to the PFC approach to serve as further theoretical fundamentals for the latter. In this review, we summarize these methodological development steps as well as the most important applications of the PFC method with a special focus on the interaction of development steps taken in hard and soft matter physics, respectively. Doing so, we hope to present today's state of the art in PFC modelling as well as the potential, which might still arise from this method in physics and materials science in the nearby future.

PACS: 64.70.D- Solid–liquid transitions; 81.10.Aj Theory and models of crystal growth; physics and chemistry of crystal growth, crystal morphology, and orientation; 68.08.-p Liquid–solid interfaces; 61.30.-v Liquid crystals

Keywords: phase-field-crystal models; static and dynamical density functional theory; condensed matter dynamics of liquid crystals; nucleation and pattern formation; simulations in materials science; colloidal crystal growth and growth anisotropy

Contents

	PAGE
1 Introduction	668
2 From DFT to phase-field-crystal models	671
2.1. Density functional theory	672
2.2. Dynamical density functional theory	675
2.2.1. Basic equations	675
2.2.2. Brownian dynamics: Langevin and Smoluchowski picture	676
2.2.3. Derivation of DDFT	677
2.2.4. Application of DDFT to colloidal crystal growth	678
2.3. Derivation of the PFC model for isotropic particles from DFT	678
2.3.1. Free-energy functional	678
2.3.2. Dynamical equations	681

*Corresponding authors. Email: heike.emmerich@uni-bayreuth.de; hlowen@thphy.uni-duesseldorf.de; granasy.laszlo@wigner.mta.hu

2.3.3. Colloidal crystal growth: DDFT versus PFC modelling	682
3 Phase-field-crystal modelling in condensed matter physics	683
3.1. The original PFC model and its generalizations	684
3.1.1. Single-component PFC models	684
3.1.1.1 The free energy.	684
3.1.1.2 The equation of motion.	687
3.1.1.3 The Euler–Lagrange equation.	689
3.1.2. Binary PFC models	689
3.1.2.1 The free energy.	689
3.1.2.2 The equations of motion.	691
3.1.2.3 The Euler–Lagrange equations.	692
3.1.3. PFC models for liquid crystals	692
3.1.3.1 Statics.	693
3.1.3.2 Two spatial dimensions.	694
3.1.3.3 Three spatial dimensions.	697
3.1.3.4 Dynamics.	698
3.1.4. Numerical methods	700
3.1.4.1 The equation of motion.	700
3.1.4.2 The Euler–Lagrange equation and other saddle point finding methods.	700
3.1.5. Coarse-graining the PFC models	700
3.1.5.1 Amplitude equations based on renormalization group theory.	700
3.1.5.2 Phenomenological amplitude equations.	701
3.2. Phase diagrams the PFC models realize	701
3.2.1. Phase diagram of single-component and binary systems	701
3.2.2. Phase diagram of two-dimensional liquid crystals	704
3.3. Anisotropies in the PFC models	707
3.3.1. Free energy of the liquid–solid interface	708
3.3.1.1 Numerical results.	708
3.3.1.2 Analytical results.	708
3.3.2. Growth anisotropy	709
3.4. Glass formation	709
3.5. Phase-field-crystal modelling of foams	710
3.6. Coupling to hydrodynamics	710
4 Phase-field-crystal models applied to nucleation and pattern formation in metals	712
4.1. Properties of nuclei from extremum principles	712
4.1.1. Homogeneous nucleation	712
4.1.2. Heterogeneous nucleation	714
4.2. Pattern formation	714
4.2.1. PFC modelling of surface patterns	715
4.2.2. Pattern formation during binary solidification	717
4.2.2.1 Dendritic freezing.	717
4.2.2.2 Eutectic solidification.	717
4.3. Phenomena in the solid state	718
4.3.1. Dislocation dynamics and grain-boundary melting	720
4.3.2. Crack formation and propagation	721
4.3.3. Strain-induced morphologies	722
4.3.4. Kirkendall effect	722
4.3.5. Density/solute trapping	722

4.3.6. Vacancy/atom transport in the VPFC model	723
5 Phase-field-crystal modelling in soft matter physics	723
5.1. Applications to colloids	723
5.1.1. Nucleation in colloidal crystal aggregation	724
5.1.1.1 Homogeneous nucleation.	724
5.1.1.2 Heterogeneous nucleation.	726
5.1.2. Pattern formation in colloidal crystal aggregation	728
5.1.2.1 Colloid patterns in two dimensions.	728
5.1.2.2 Colloid patterns in three dimensions.	728
5.1.3. Colloid patterning	730
5.2. Application to liquid crystals	732
6 Summary and outlook	732
Acknowledgements	734
Notes	734
References	734
Appendix	741

List of abbreviations

2D	two spatial dimensions
3D	three spatial dimensions
1M-PFC model	single-mode PFC model
2M-PFC model	two-mode PFC model
APFC model	anisotropic PFC model
ATG instability	Asaro-Tiller-Grinfeld instability
bcc crystal structure	body-centred cubic crystal structure
bct crystal structure	body-centred tetragonal crystal structure
BVP	boundary value problem
CMA	constant-mobility approximation
DDFT	dynamical DFT
DFT	density functional theory
DLVO potential	Derjaguin-Landau-Verwey-Overbeek potential
DMD simulation	diffusive MD simulation
EAP-MD simulation	embedded-atom-potential MD simulation
ELE	Euler-Lagrange equation
EOF-PFC model	eighth-order fitting PFC model
EOM	equation of motion
fcc crystal structure	face-centred cubic crystal structure
FD scheme	finite-difference scheme
FMT	fundamental-measure theory
GRP-PFC model	Greenwood-Rottler-Provatas PFC model
hcp crystal structure	hexagonal close packed crystal structure
HS potential	hard-sphere potential
LJ potential	Lennard-Jones potential
MCT	mode-coupling theory
MD simulation	molecular-dynamics simulation
Model B	relaxational dynamical equation for a conserved order parameter
MPFC model	modified PFC model

NS equation	Navier-Stokes equation
PFC model	phase-field-crystal model
PFC1 model	dynamical equation for the original PFC model without CMA
PFC2 model	dynamical equation for the original PFC model with CMA
PF model	phase-field model
RLV	reciprocal lattice vector
sc crystal structure	simple cubic crystal structure
SH model	Swift-Hohenberg model
VPFC model	vacancy PFC model

1. Introduction

Pattern formation has been observed in complex systems from microscopic to cosmic scales (for examples, see Figure 1), a phenomenon that has been exciting the fantasy of humanity for a long time. Non-equilibrium systems in physics, chemistry, biology, mathematics, cosmology, and other fields produce an amazingly rich and visually fascinating variety of spatio-temporal behaviour. Experiments and simulations show that many of such systems – reacting chemicals, bacteria colonies, granular matter, plasmas – often display analogous dynamical behaviour. The wish to find the origin of the common behaviour has been driving the efforts for finding unifying schemes that allow the assigning of many of these processes into a few universality classes. Pattern formation and the associated nonlinear dynamics have received a continuous attention of the statistical physics community over the past decades. Reviews of the advances made in different directions are available in the literature and range from early works on critical dynamics [1] via phase-separation [2] and pattern formation in non-equilibrium systems [3,4] to recent detailed treatments of the field in books [5–7]. In particular, Seul and Andelman [4] described pattern formation on the mesoscale as manifestation of modulated structures. Within this approach, the modulated phases are stabilized by competing attractive and repulsive interactions, which favour inhomogeneities characterized by a certain modulation length scale. The modulations are described by a single scalar order parameter. As outlined in reference [4], the idea of Seul and Andelman can be applied to a large variety of systems ranging from Langmuir films over semiconductor surfaces and magnet garnets to polyelectrolyte solutions. Furthermore, the pioneering theories of spontaneous domain formation in magnetic materials and in the intermediate state of type I superconductors has been reinterpreted within this framework.

In the past decade, special attention has been paid to a similar model, whose mathematical formulation has been laid down decades earlier to address hydrodynamic instabilities [10] and to describe the transition to the antiferromagnetic state in liquid ^3He or to a non-uniform state in cholesteric liquid crystals [11], whereas recently it has been employed for the modelling of crystallization in undercooled liquids on the atomic scale [12]. This approach is known to the materials science community as the phase-field-crystal (PFC) model [12], and has proved to be an amazingly efficient tool for addressing crystalline self-organization/pattern formation on the *atomistic* scale.

The PFC approach attracts attention owing to a unique situation: the crystallization of liquids is traditionally addressed on this scale by the density functional theory (DFT) [13–15], whose best developed non-perturbative version, known as the fundamental-measure theory (FMT) [16], leads to unprecedented accuracy for such properties as the liquid–solid interfacial free energy [17,18] or the nucleation barrier [17]. However, handling of large systems is hampered by the complexity of such models. In turn, the PFC model, being a simplistic DFT itself, incorporates most of the essential physics required to handle freezing: it is atomistic, anisotropies and elasticity are

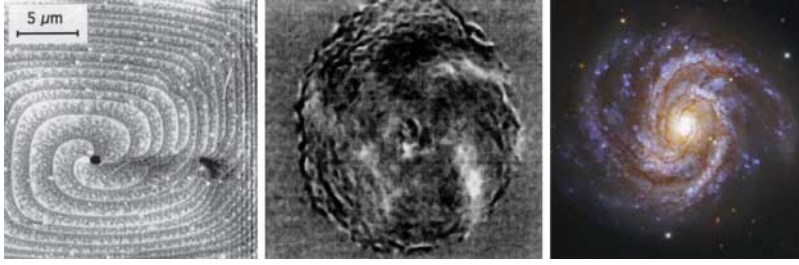


Figure 1. Pattern formation on microscopic to cosmic length scales. From left to right: multiple spiralling nanoscale terraces starting from a central heterogeneity. (Reproduced with permission from Klemenž [8] © 1998 by Elsevier.) Cellular slime mould self-organized into a five-arm spiral structure. (Reproduced with permission from Vasiev *et al.* [9] © 1997 by the American Physical Society.) Messier 100, a multi-arm spiral galaxy in the Virgo Supercluster, 60 million light-years from earth. (Credit: ESO/IDA/Danish 1.5 m/R. Gendler, J.-E. Ovaldsen, C.C. Thöne, and C. Féron.)

automatically there, the system may choose from a variety of periodic states (such as body-centred cubic (bcc), face-centred cubic (fcc), and hexagonal close packed (hcp)) besides the homogeneous fluid, etc. The free-energy functional is fairly simple having the well-known Swift-Hohenberg (SH) form

$$\tilde{\mathcal{F}} = \int d\tilde{\mathbf{r}} \left(\frac{\tilde{\psi}}{2} (-\beta + (k_0^2 + \nabla_{\tilde{\mathbf{r}}}^2)^2) \tilde{\psi} + \frac{\tilde{\psi}^4}{4} \right), \quad (1)$$

where $\tilde{\psi}$ is the reduced particle density and β a reduced temperature, while k_0 is the absolute value of the wave number vector the system prefers. (In Equation (1), all quantities are dimensionless.) This together with the assumption of overdamped conservative (diffusive) dynamics (a major deviation from the non-conservative dynamics of the SH model) leads to a relatively simple equation of motion (EOM) that, in turn, allows the handling of a few times 10^7 atoms on the diffusive time scale. Such abilities can be further amplified by the amplitude equation versions [19] obtained by renormalization group theory, which combined with advanced numerics [20] allows for the handling of relatively big chunks of material, while retaining all the atomic scale physics. Such a coarse-grained PFC model, relying on equations of motion for the amplitudes and phases, can be viewed as a physically motivated continuum model akin to the highly successful and popular phase-field (PF) models [21–25], which however usually contain *ad hoc* assumptions. Accordingly, the combination of the PFC model with coarse graining establishes a link between DFT and conventional PF models, offering a way for deriving the latter on physical grounds.

In its simplest formulation, defined above, the PFC model consists of only a single model parameter β (provided that length is measured in k_0^{-1} units). Still it has a fairly complex phase diagram in three spatial dimensions (3D), which has stability domains for the bcc, fcc, and hcp structures, as opposed to the single triangular crystal structure appearing in two spatial dimensions (2D). Introducing additional model parameters, recent extensions of the PFC model either aim at further controlling of the predicted crystal structure or attempt to refine the description of real materials. Other extensions address binary systems, yet others modify the dynamics via considering further modes of density relaxation besides the diffusive one, while adopting a free energy that ensures particle conservation and allows assigning inertia to the particles. In a few cases, PFC models tailored to specific applications have reached the level of being quantitative. Via the PFC models, a broad range of exciting phenomena became accessible for

atomistic simulations (Table 1), a situation that motivates our review of the present status of PFC modelling.

While Table 1 contains a fairly impressive list, it is expected to be only the beginning of the model's employment in materials science and engineering. For example, true knowledge-based tailoring of materials via predictive PFC calculations is yet an open vision, for which a number of difficulties need to be overcome. We are going to review a few of the most fundamental ones of these open issues. For example, the PFC models still have to establish themselves as widely accepted simulation tools in materials engineering/design, which requires methodological advances in various directions such as (a) ensuring the quantitateness of PFC predictions for practically relevant (multi-phase multi-component) materials and (b) a consistent extension of PFC modelling to some essential circumstances such as non-isothermal problems, coupling to hydrodynamics, or handling of non-spherical molecules.

So far, only limited reviews of PFC modelling are available [25,71]. Therefore, we give a comprehensive overview of PFC modelling in the present review. Especially, we present the main achievements of PFC modelling and demonstrate the potential these models offer for addressing problems in physics and materials science. We pay special attention to the similarities and differences of development steps taken in hard and soft matter physics, respectively. The rest of our review article is structured as follows: in Section 2, we present a detailed theoretical derivation of the PFC model on the basis of dynamical density functional theory (DDFT). Section 3 is devoted to some essential features of the PFC model and its generalizations including the realization of different crystal lattices, the predicted phase diagrams, anisotropy, and some specific issues such as glass formation, application to foams, and the possibility for coupling to hydrodynamics. Section 4 addresses nucleation and pattern formation in metallic alloys, whereas Section 5 deals with the application of the PFC models to prominent soft matter systems. Finally, in Section 6, we offer a few concluding remarks and an outlook to probable developments in the near future.

Table 1. A non-exclusive collection of phenomena addressed using PFC techniques.

Phenomena	References
Liquid–solid transition:	
Dendrites	[26–30]
Eutectics	[26,28,29,31]
Homogeneous nucleation	[28,30–33]
Heterogeneous nucleation	[30,31,34,35]
Grain-boundary melting	[36,37]
Fractal growth	[38,39]
Crystal anisotropy	[33,38,40–44]
Density/solute trapping	[38,39,45]
Glass formation	[35,46,47]
Surface alloying	[48–50]
Epitaxy/heteroepitaxy	[12,26,43,48,50–53]
Surface ordering	[50,54–58]
Colloid patterning	[33]
Grain-boundary dynamics	[59]
Crack propagation	[59]
Elasticity, plasticity, dislocation dynamics	[12,51,59–63]
Kirkendall effect	[64]
Vacancy transport	[65]
Liquid phase-separation with colloid accumulation at phase boundaries	[66]
Transitions in liquid crystals	[67–69]
Formation of foams	[70]

2. From DFT to phase-field-crystal models

Freezing and crystallization phenomena are described best on the most fundamental level of individual particles, which involves the microscopic size and interaction length scale of the particles (Figure 2). The individual dynamics of the particles happens correspondingly on a microscopic time scale. In the following, two different classes of materials, namely *molecular* and *colloidal* materials, need clear distinction. The former comprise metals as well as molecular insulators and semiconductors. We consider these molecular systems as classical particles, where the quantum-mechanical nature of the electrons merely enters via effective molecular force fields. The corresponding molecular dynamics (MD) is governed by Newton's second law. Hence the length scale is atomic (about a few Angstroms) and the typical time scale is roughly a picosecond.

The latter material class of colloidal systems involves typically mesoscopic particles immersed in a molecular viscous fluid as a solvent that are interacting via effective forces [72]. These colloidal

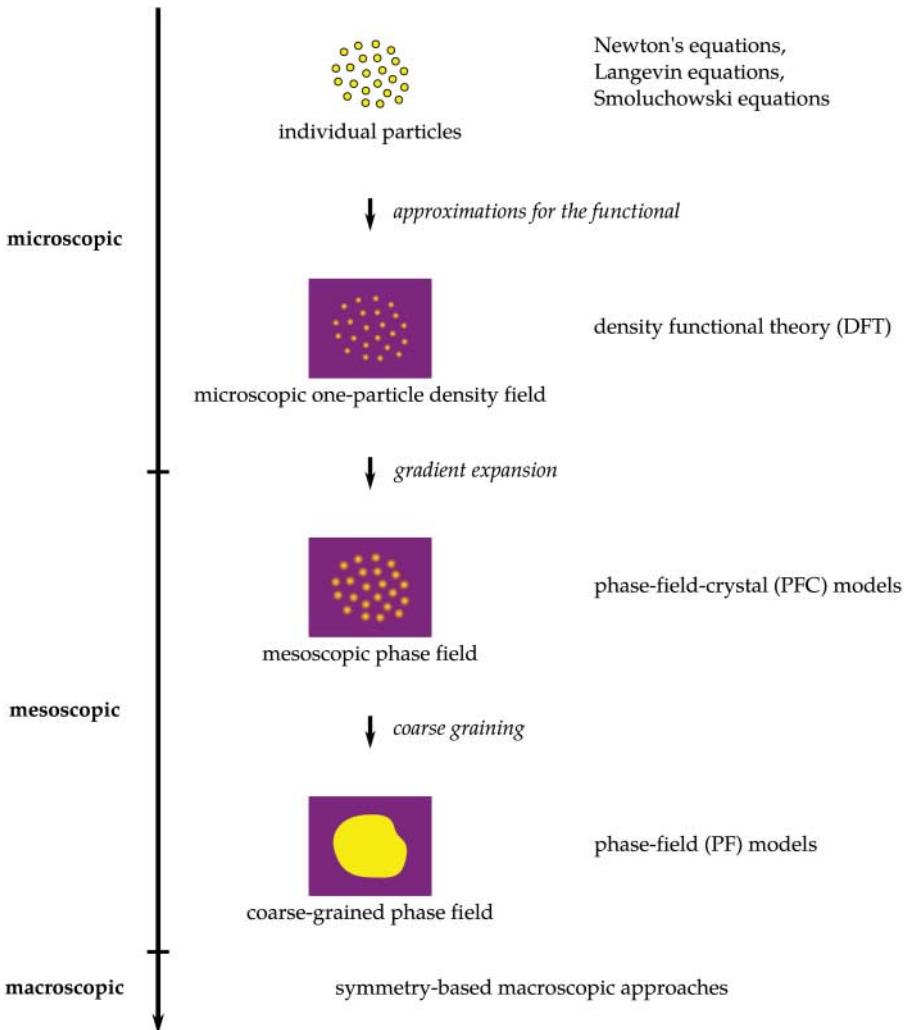


Figure 2. Levels of description with the corresponding methods and theories (schematic).

suspensions have a dimension typically in the range between a nanometre and a micrometre and are therefore classical particles. Thus, the corresponding “microscopic” length scale describing their extension and interaction range is much bigger than for the molecular materials. The individual particle dynamics is *Brownian motion* [73,74], that is, it is completely overdamped¹ superimposed with stochastic kicks of the solvent. The corresponding coarse-grained Brownian time scale upon which individual particle motion occurs is much longer (about a microsecond) [77].

In terms of static equilibrium properties (such as structural correlations and phase transitions), both metals and colloids can just be regarded as classical interacting many-body systems. For this purpose, DFT was developed [14,15,78]: DFT is a microscopic theory, that is, it starts with the (effective) interparticle interactions and predicts the free energy and the static many-body correlations. In principle, DFT is exact, but for practical applications one has to rely on approximations.

In the past years, it has become clear that DFT is an ideal theoretical framework to justify and to derive the free-energy functional of coarse-grained models as the PFC approach [26,53,79]. PFC models keep the microscopic length scale, but describe the microscopically structured density field in a very rough way, for example, by keeping only its first Fourier modes for a crystal. Although some microscopic details are lost, the basic picture of the crystal is kept and much larger system sizes can be explored numerically. The PFC models are superior to simple PF models, which work with a single order parameter on a more coarse-grained regime. Finally, there are also phenomenological hydrodynamic approaches that are operating on the macroscopic length and time scale.

This pretty transparent hierarchy of length scales for static equilibrium properties gets more complex for the dynamics. In order to discuss this in more detail, it is advantageous to start with the colloidal systems first. Here, the individual dynamics is already dissipative and overdamped: the “microscopic” equations governing the colloidal Brownian dynamics are either the *Langevin equation* for the individual particle trajectories or the *Smoluchowski equation* for the time evolution of the many-body probability density [80,81]. Both approaches are stochastically equivalent [82]. In the end of the past century, it has been shown that there is a dynamic generalization of DFT, the DDFT, which describes the time evolution of the many-body system within the time-dependent one-body density as a generalized deterministic diffusion equation. This provides a significant simplification of the many-body problem. Unfortunately, DDFT is not on the same level as the Smoluchowski or Langevin picture since an additional adiabaticity approximation is needed to derive it. This approximation implies, that the one-body density is a slowly relaxing variable and all higher density correlations relax much faster to thermodynamic equilibrium [83]. Fortunately, the adiabaticity approximation is reasonable for many practical applications except for situations, where fluctuations play a significant role. Now, DDFT can be used as an (approximate) starting point to derive the dynamics of a PFC model systematically [79]. This also points to alternative dynamical equations, which can be implemented within a numerically similar effort as compared to ordinary PFC equations, but are a bit closer to DDFT.

For Newtonian dynamics, on the other hand, intense research is going on to derive a similar kind of DDFT [84–87]. Still the diffusive (or model B) dynamics for a conserved order-parameter field can be used as an effective dynamics on mesoscopic time scales with an effective friction. Then, the long-time self-diffusion coefficient sets the time scale of this process. One should, however, point out that the PFC dynamics for molecular systems is dynamically more coarse-grained than for their colloidal counterparts.

2.1. Density functional theory

DFT is a microscopic theory for inhomogeneous complex fluids in equilibrium [14,15,78,88] that needs only the particle interactions and the underlying thermodynamic conditions as an input.

The central idea is to express the free energy of the many-body system as a functional of the inhomogeneous one-body density. As it stands originally, DFT is a theory for static quantities. Most of the actual applications of DFT are for spherically symmetric pairwise interactions between classical particles (mostly hard spheres) [14,78,89], but they can also be generalized to anisotropic interactions (as relevant to non-spherical hard bodies or molecules) [90–93]. One of the key applications of DFT concerns the equilibrium freezing and melting [14,15,94,95] including the fluid–solid interface [96–99]. Further information about DFT and a detailed historic overview can be found in several articles and books like references [96,100–103].

More recently, static DFT was generalized towards time-dependent processes in non-equilibrium. The extended approach is called DDFT. DDFT was first derived in 1999 for isotropic Brownian particles by Marconi and Tarazona [104,105] starting from the Langevin picture of individual particle trajectories. An alternate derivation based on the Smoluchowski picture was presented in 2004 by Archer and Evans [106]. In both schemes, an additional *adiabaticity approximation* is needed: correlations of high order in non-equilibrium are approximated by those in equilibrium for the same one-body density. These derivations were complemented by a further approach on the basis of a projection operator technique [83]. The latter approach sheds some light on the adiabaticity approximation: it can be viewed by the assumption that the one-body density relaxes much slower than any other density correlations of higher order. DDFT can be flexibly generalized towards more complex situations including mixtures [107], active particles [108], hydrodynamic interactions [109,110], shear flow [111], and non-spherical particles [112,113]. However, as already stated above, it is much more difficult to derive a DDFT for Newtonian dynamics, where inertia and flow effects invoke a treatment of the momentum density field of the particles [84–87].

In detail, DFT gives access to the free energy for a system of N classical particles, whose centre-of-mass positions are defined through the vectors \mathbf{r}_i with $i \in \{1, \dots, N\}$, by the *one-particle density* $\rho(\mathbf{r})$, which provides the probability to find a particle at position \mathbf{r} . Its microscopic definition is

$$\rho(\mathbf{r}) = \left\langle \sum_{i=1}^N \delta(\mathbf{r} - \mathbf{r}_i) \right\rangle \quad (2)$$

with the normalized classical canonical (or grand canonical) ensemble-average $\langle \cdot \rangle$. At given temperature T and chemical potential μ , the particles are interacting via a pairwise (two-body) potential $U_2(\mathbf{r}_1 - \mathbf{r}_2)$. Furthermore, the system is exposed to an external (one-body) potential $U_1(\mathbf{r})$ (describing, for example, gravity or system boundaries), which gives rise in general to an inhomogeneous one-particle density $\rho(\mathbf{r})$. DFT is based on the following variational theorem:

There exists a unique grand canonical free-energy functional $\Omega(T, \mu, [\rho(\mathbf{r})])$ of the one-particle density $\rho(\mathbf{r})$, which becomes minimal for the equilibrium one-particle density $\rho(\mathbf{r})$:

$$\frac{\delta \Omega(T, \mu, [\rho(\mathbf{r})])}{\delta \rho(\mathbf{r})} = 0. \quad (3)$$

If the grand canonical functional $\Omega(T, \mu, [\rho(\mathbf{r})])$ is evaluated at the equilibrium one-particle density $\rho(\mathbf{r})$, it is the real equilibrium grand canonical free energy of the inhomogeneous system.

Hence, DFT establishes a basis for the determination of the equilibrium one-particle density field $\rho(\mathbf{r})$ of an arbitrary classical many-body system. However, in practice, the exact form of the grand canonical free-energy density functional $\Omega(T, \mu, [\rho(\mathbf{r})])$ is not known and one has to rely on approximations. Via a Legendre transform, the grand canonical functional can be expressed by an

equivalent Helmholtz free-energy functional $\mathcal{F}(T, [\rho(\mathbf{r})])$,

$$\Omega(T, \mu, [\rho(\mathbf{r})]) = \mathcal{F}(T, [\rho(\mathbf{r})]) - \mu \int d\mathbf{r} \rho(\mathbf{r}), \quad (4)$$

with V denoting the system volume. The latter is conveniently split into three contributions:

$$\mathcal{F}(T, [\rho(\mathbf{r})]) = \mathcal{F}_{\text{id}}(T, [\rho(\mathbf{r})]) + \mathcal{F}_{\text{exc}}(T, [\rho(\mathbf{r})]) + \mathcal{F}_{\text{ext}}(T, [\rho(\mathbf{r})]). \quad (5)$$

Here, $\mathcal{F}_{\text{id}}(T, [\rho(\mathbf{r})])$ is the (exact) *ideal gas free-energy functional* [78]

$$\mathcal{F}_{\text{id}}(T, [\rho(\mathbf{r})]) = k_{\text{B}}T \int d\mathbf{r} \rho(\mathbf{r}) (\ln(\Lambda^3 \rho(\mathbf{r})) - 1), \quad (6)$$

where k_{B} is the Boltzmann constant and Λ the thermal de Broglie wavelength. The second term on the right-hand-side of Equation (5) is the *excess free-energy functional* $\mathcal{F}_{\text{exc}}(T, [\rho(\mathbf{r})])$ describing the excess free energy over the exactly known ideal-gas functional. It incorporates all correlations due to the pair interactions between the particles. In general, it is not known explicitly and therefore needs to be approximated appropriately [14,78]. The last contribution is the *external free-energy functional* [78]

$$\mathcal{F}_{\text{ext}}(T, [\rho(\mathbf{r})]) = \int d\mathbf{r} \rho(\mathbf{r}) U_1(\mathbf{r}). \quad (7)$$

A formally exact expression for $\mathcal{F}_{\text{exc}}(T, [\rho(\mathbf{r})])$ is gained by a functional Taylor expansion in the density variations $\Delta\rho(\mathbf{r}) = \rho(\mathbf{r}) - \rho_{\text{ref}}$ around a homogeneous reference density ρ_{ref} [78,94]:

$$\mathcal{F}_{\text{exc}}(T, [\rho(\mathbf{r})]) = \mathcal{F}_{\text{exc}}^{(0)}(\rho_{\text{ref}}) + k_{\text{B}}T \sum_{n=1}^{\infty} \frac{1}{n!} \mathcal{F}_{\text{exc}}^{(n)}(T, [\rho(\mathbf{r})]) \quad (8)$$

with

$$\mathcal{F}_{\text{exc}}^{(n)}(T, [\rho(\mathbf{r})]) = - \int d\mathbf{r}_1 \cdots \int d\mathbf{r}_n c^{(n)}(\mathbf{r}_1, \dots, \mathbf{r}_n) \prod_{i=1}^n \Delta\rho(\mathbf{r}_i). \quad (9)$$

Here, $c^{(n)}(\mathbf{r}_1, \dots, \mathbf{r}_n)$ denotes the n th-order direct correlation function [101] in the homogeneous reference state given by

$$c^{(n)}(\mathbf{r}_1, \dots, \mathbf{r}_n) = - \frac{1}{k_{\text{B}}T} \left. \frac{\delta^n \mathcal{F}_{\text{exc}}(T, [\rho(\mathbf{r})])}{\delta\rho(\mathbf{r}_1) \cdots \delta\rho(\mathbf{r}_n)} \right|_{\rho_{\text{ref}}} \quad (10)$$

depending parametrically on T and ρ_{ref} .

In the functional Taylor expansion (8), the constant zeroth-order contribution is irrelevant and the first-order contribution corresponding to $n = 1$ is zero.² The higher-order terms are non-local and do not vanish in general.

In the simplest non-trivial approach, the functional Taylor expansion is truncated at second order. The resulting approximation is known as the *Ramakrishnan–Yussouff theory* [94]

$$\mathcal{F}_{\text{exc}}(T, [\rho(\mathbf{r})]) = -\frac{1}{2} k_{\text{B}}T \int d\mathbf{r}_1 \int d\mathbf{r}_2 c^{(2)}(\mathbf{r}_1 - \mathbf{r}_2) \Delta\rho(\mathbf{r}_1) \Delta\rho(\mathbf{r}_2) \quad (11)$$

and predicts the freezing transition of hard spheres both in 3D [94] and 2D [114].³ The Ramakrishnan–Yussouff approximation needs the fluid direct pair-correlation function $c^{(2)}(\mathbf{r}_1 - \mathbf{r}_2)$ as an input. For example, $c^{(2)}(\mathbf{r}_1 - \mathbf{r}_2)$ can be gained from liquid integral equation

theory, which links $c^{(2)}(\mathbf{r}_1 - \mathbf{r}_2)$ to the pair-interaction potential $U_2(\mathbf{r}_1 - \mathbf{r}_2)$. Well-known analytic approximations for the direct pair-correlation function include the second-order *virial expression* [118]

$$c^{(2)}(\mathbf{r}_1 - \mathbf{r}_2) = \exp\left(-\frac{U_2(\mathbf{r}_1 - \mathbf{r}_2)}{k_B T}\right) - 1. \quad (12)$$

The resulting *Onsager functional* for the excess free energy becomes asymptotically exact in the low density limit [101]. An alternative is the *random-phase* or *mean-field approximation*

$$c^{(2)}(\mathbf{r}_1 - \mathbf{r}_2) = -\frac{U_2(\mathbf{r}_1 - \mathbf{r}_2)}{k_B T}. \quad (13)$$

For bounded potentials, this mean-field approximation becomes asymptotically exact at high densities [112,119–121]. Non-perturbative expressions for the excess free-energy functional for colloidal particles are given by *weighted-density approximations* [90,93,96,122,123] or follow from FMT [91,124]. FMT was originally introduced in 1989 by Rosenfeld for isotropic particles [16,95,100,125] and then refined later [89,126] – for a review, see reference [88]. For hard spheres, FMT provides an excellent approximation for the excess free-energy functional with an unprecedented accuracy. It was also generalized to arbitrarily shaped particles [91,124,127].

2.2. Dynamical density functional theory

2.2.1. Basic equations

DDFT is the time-dependent analogue of static DFT and can be classified as *linear-response theory*. In its basic form, it describes the slow dissipative non-equilibrium relaxation dynamics of a system of N Brownian particles close to thermodynamic equilibrium or the behaviour in a time-dependent external potential $U_1(\mathbf{r}, t)$. Now a time-dependent one-particle density field is defined via

$$\rho(\mathbf{r}, t) = \left\langle \sum_{i=1}^N \delta(\mathbf{r} - \mathbf{r}_i(t)) \right\rangle, \quad (14)$$

where $\langle \cdot \rangle$ denotes the normalized classical canonical noise-average over the particle trajectories and t is the time variable.

This one-particle density is conserved and its dynamics is assumed to be dissipative via the generalized (deterministic) diffusion equation

$$\frac{\partial \rho(\mathbf{r}, t)}{\partial t} = \frac{D_T}{k_B T} \nabla_{\mathbf{r}} \cdot \left(\rho(\mathbf{r}, t) \nabla_{\mathbf{r}} \frac{\delta \mathcal{F}(T, [\rho(\mathbf{r}, t)])}{\delta \rho(\mathbf{r}, t)} \right). \quad (15)$$

Here, D_T denotes a (short-time) translational diffusion coefficient for the Brownian system. Referring to Equations (3) and (4), the functional derivative in the DDFT equation can be interpreted as an inhomogeneous chemical potential

$$\mu(\mathbf{r}, t) = \frac{\delta \mathcal{F}(T, [\rho(\mathbf{r}, t)])}{\delta \rho(\mathbf{r}, t)} \quad (16)$$

such that the DDFT equation (15) corresponds to a generalized Fick’s law of particle diffusion. As already mentioned, DDFT was originally invented [104,106] for colloidal particles, which exhibit Brownian motion, but is less justified for metals and atomic systems whose dynamics are ballistic [84,85].

2.2.2. Brownian dynamics: Langevin and Smoluchowski picture

The DDFT equation (15) can be derived [104] from Langevin equations that describe the stochastic motion of the N isotropic colloidal particles in an incompressible liquid of viscosity η at low Reynolds number (Stokes limit). In the absence of hydrodynamic interactions between the Brownian particles, these coupled Langevin equations for the positions $\mathbf{r}_i(t)$ of the colloidal spheres with radius R_s describe completely overdamped motion plus stochastic noise [80,82]:

$$\dot{\mathbf{r}}_i = \xi^{-1}(\mathbf{F}_i + \mathbf{f}_i), \quad i = 1, \dots, N. \quad (17)$$

Here, ξ is the Stokesian friction coefficient ($\xi = 6\pi\eta R_s$ for spheres of radius R_s with stick boundary conditions) and

$$\mathbf{F}_i(t) = -\nabla_{\mathbf{r}_i} U(\mathbf{r}_1, \dots, \mathbf{r}_N, t) \quad (18)$$

are the deterministic forces caused by the total potential

$$U(\mathbf{r}_1, \dots, \mathbf{r}_N, t) = U_{\text{ext}}(\mathbf{r}_1, \dots, \mathbf{r}_N, t) + U_{\text{int}}(\mathbf{r}_1, \dots, \mathbf{r}_N) \quad (19)$$

with

$$U_{\text{ext}}(\mathbf{r}_1, \dots, \mathbf{r}_N, t) = \sum_{i=1}^N U_1(\mathbf{r}_i, t) \quad (20)$$

and

$$U_{\text{int}}(\mathbf{r}_1, \dots, \mathbf{r}_N) = \sum_{\substack{i,j=1 \\ i < j}}^N U_2(\mathbf{r}_i - \mathbf{r}_j). \quad (21)$$

On top of these deterministic forces, also stochastic forces $\mathbf{f}_i(t)$ due to thermal fluctuations act on the Brownian particles. These random forces are modelled by Gaussian white noises with vanishing mean values

$$\langle \mathbf{f}_i(t) \rangle = \mathbf{0} \quad (22)$$

and with Markovian second moments

$$\langle \mathbf{f}_i(t_1) \otimes \mathbf{f}_j(t_2) \rangle = 2\xi k_B T \mathbf{1} \delta_{ij} \delta(t_1 - t_2), \quad (23)$$

where \otimes is the ordinary (dyadic) tensor product (to make the notation compact) and $\mathbf{1}$ denotes the 3×3 -dimensional unit matrix. This modelling of the stochastic forces is dictated by the fluctuation-dissipation theorem, which for spheres yields the Stokes–Einstein relation $D_T = k_B T / \xi$ [73], that couples the short-time diffusion coefficient D_T of the colloidal particles to the Stokes friction coefficient ξ .

An alternate description of Brownian dynamics is provided by the Smoluchowski picture, which is stochastically equivalent to the Langevin picture [81,82]. The central quantity in the Smoluchowski picture is the N -particle probability density $P(\mathbf{r}_1, \dots, \mathbf{r}_N, t)$ whose time evolution is described by the Smoluchowski equation [82,128]

$$\frac{\partial}{\partial t} P(\mathbf{r}_1, \dots, \mathbf{r}_N, t) = \hat{\mathcal{L}} P(\mathbf{r}_1, \dots, \mathbf{r}_N, t) \quad (24)$$

with the Smoluchowski operator

$$\hat{\mathcal{L}} = D_T \sum_{i=1}^N \nabla_{\mathbf{r}_i} \cdot \left(\nabla_{\mathbf{r}_i} \frac{U(\mathbf{r}_1, \dots, \mathbf{r}_N, t)}{k_B T} + \nabla_{\mathbf{r}_i} \right). \quad (25)$$

While the N -particle probability density $P(\mathbf{r}_1, \dots, \mathbf{r}_N, t)$ in this Smoluchowski equation is a highly non-trivial function for interacting particles, it is often sufficient to consider one-body or two-body

densities. The one-particle probability density $P(\mathbf{r}, t)$ is proportional to the one-particle number density $\rho(\mathbf{r}, t)$. In general, all n -particle densities with $n \leq N$ can be obtained from the N -particle probability density $P(\mathbf{r}_1, \dots, \mathbf{r}_N, t)$ by integration over the remaining degrees of freedom:

$$\rho^{(n)}(\mathbf{r}_1, \dots, \mathbf{r}_n, t) = \frac{N!}{(N-n)!} \int d\mathbf{r}_{n+1} \dots \int d\mathbf{r}_N P(\mathbf{r}_1, \dots, \mathbf{r}_N, t). \quad (26)$$

2.2.3. Derivation of DDFT

We now sketch how to derive the DDFT equation (15) from the Smoluchowski picture following the idea of Archer and Evans [106]. Integrating the Smoluchowski equation (24) over the positions of $N - 1$ particles yields the exact equation

$$\dot{\rho}(\mathbf{r}, t) = D_T \nabla_{\mathbf{r}} \cdot \left(\nabla_{\mathbf{r}} \rho(\mathbf{r}, t) - \frac{\bar{F}(\mathbf{r}, t)}{k_B T} + \frac{\rho(\mathbf{r}, t)}{k_B T} \nabla_{\mathbf{r}} U_1(\mathbf{r}, t) \right) \quad (27)$$

for the one-particle density $\rho(\mathbf{r}, t)$, where

$$\bar{F}(\mathbf{r}, t) = - \int d\mathbf{r}' \rho^{(2)}(\mathbf{r}, \mathbf{r}', t) \nabla_{\mathbf{r}} U_2(\mathbf{r} - \mathbf{r}') \quad (28)$$

is an average force, that in turn depends on the non-equilibrium two-particle density $\rho^{(2)}(\mathbf{r}_1, \mathbf{r}_2, t)$. This quantity is approximated by an equilibrium expression. To derive this expression, we consider first the equilibrium state of Equation (27). This leads to

$$\bar{F}(\mathbf{r}) = k_B T \nabla_{\mathbf{r}} \rho(\mathbf{r}) + \rho(\mathbf{r}) \nabla_{\mathbf{r}} \bar{U}_1(\mathbf{r}), \quad (29)$$

which is the first equation of the Yvon-Born-Green hierarchy, with a “substitute” external potential $\bar{U}_1(\mathbf{r})$. In equilibrium, DFT implies

$$\begin{aligned} 0 &= \frac{\delta \Omega(T, \mu, [\rho(\mathbf{r})])}{\delta \rho(\mathbf{r})} = \frac{\delta \mathcal{F}(T, [\rho(\mathbf{r})])}{\delta \rho(\mathbf{r})} - \mu \\ &= k_B T \ln(\Lambda^3 \rho(\mathbf{r})) + \frac{\delta \mathcal{F}_{\text{exc}}(T, [\rho(\mathbf{r})])}{\delta \rho(\mathbf{r})} + \bar{U}_1(\mathbf{r}) \end{aligned} \quad (30)$$

and after application of the gradient operator

$$0 = k_B T \frac{\nabla_{\mathbf{r}} \rho(\mathbf{r})}{\rho(\mathbf{r})} + \nabla_{\mathbf{r}} \frac{\delta \mathcal{F}_{\text{exc}}(T, [\rho(\mathbf{r})])}{\delta \rho(\mathbf{r})} + \nabla_{\mathbf{r}} \bar{U}_1(\mathbf{r}). \quad (31)$$

A comparison of Equations (29) and (31) yields

$$\bar{F}(\mathbf{r}) = -\rho(\mathbf{r}) \nabla_{\mathbf{r}} \frac{\delta \mathcal{F}_{\text{exc}}(T, [\rho(\mathbf{r})])}{\delta \rho(\mathbf{r})}. \quad (32)$$

It is postulated, that this relation also holds in non-equilibrium. The non-equilibrium correlations are thus approximated by equilibrium ones at the same $\rho(\mathbf{r})$ via a suitable “substitute” equilibrium potential $\bar{U}_1(\mathbf{r})$. With this *adiabatic approximation*, Equation (27) becomes

$$\dot{\rho}(\mathbf{r}, t) = D_T \nabla_{\mathbf{r}} \cdot \left(\nabla_{\mathbf{r}} \rho(\mathbf{r}, t) + \frac{\rho(\mathbf{r})}{k_B T} \nabla_{\mathbf{r}} \frac{\delta \mathcal{F}_{\text{exc}}(T, [\rho(\mathbf{r})])}{\delta \rho(\mathbf{r})} + \frac{\rho(\mathbf{r}, t)}{k_B T} \nabla_{\mathbf{r}} U_1(\mathbf{r}, t) \right), \quad (33)$$

which is the DDFT equation (15).

It is important to note that the DDFT equation (15) is a deterministic equation, that is, there are no additional noise terms. If noise is added, there would be double counted fluctuations in the equilibrium limit of Equation (15) since $\mathcal{F}(T, [\rho])$ is the *exact* equilibrium functional, which in principle includes all fluctuations.⁴ The drawback of the adiabatic approximation, on the other hand, is that a system is trapped for ever in a metastable state. This unphysical behaviour can be changed by adding noise on a phenomenological level though violating the caveat noted above. A pragmatic recipe is to add noise only when fluctuations are needed to push the system out of a metastable state or to regard a fluctuating density field as an initial density profile for subsequent deterministic time evolution via DDFT. In conclusion, the drawback of the adiabatic approximation is that DDFT is some kind of mean-field theory. For example, DDFT as such is unable to predict nucleation rates. It is rather a realistic theory, if a systematic drive pushes the system, as occurs, for example, for crystal growth.

2.2.4. Application of DDFT to colloidal crystal growth

An important application of DDFT is the description of colloidal crystal growth. In reference [129], DDFT was applied to two-dimensional dipoles, whose dipole moments are perpendicular to a confining plane. These dipoles interact with a repulsive inverse power-law potential $U_2(\mathbf{r}) = u_0 r^{-3}$, where $r = |\mathbf{r}|$ is the inter-particle distance. This model can be realized, for example, by superparamagnetic colloids at a water-surface in an external magnetic field [130]. Figures 3 and 4 show DDFT results from reference [129].

In Figure 3, the time evolution of the one-particle density of an initial colloidal cluster of 19 particles arranged in a hexagonal lattice is shown. This prescribed cluster is surrounded by an undercooled fluid and can act as a nucleation seed, if its lattice constant is chosen appropriately. The initial cluster either initiates crystal growth (left column in Figure 3) or the system relaxes back to the undercooled fluid (right column).

A similar investigation is also possible for other initial configurations like rows of seed particles. Figure 4 shows the crystallization process starting with six infinitely long particle rows of a hexagonal crystal, where a gap separates the first three rows from the remaining three rows. If this gap is not too big, the density peaks rearrange and a growing crystal front emerges.

2.3. Derivation of the PFC model for isotropic particles from DFT

Though approximate in practice, DFT and DDFT can be regarded to be a high level of microscopic description, which provides a framework to calibrate the more coarse-grained PFC approach. In this section, we at first describe the derivation for spherical interactions in detail and then focus more on anisotropic particles. There are two different aspects of the PFC modelling, which can be justified from DFT, respectively, DDFT, namely statics and dynamics. The static free energy used in the PFC model was first derived from DFT by Elder *et al.* [26], while the corresponding dynamics was derived from DDFT by van Teeffelen *et al.* [79]. We follow the basic ideas of these works in the sequel.

2.3.1. Free-energy functional

For the static part, we first of all define a scalar dimensionless order-parameter field $\psi(\mathbf{r})$ ⁵ by the relative density deviation

$$\rho(\mathbf{r}) = \rho_{\text{ref}}(1 + \psi(\mathbf{r})) \quad (34)$$

around the prescribed fluid reference density ρ_{ref} . This relative density deviation $\psi(\mathbf{r})$ is considered to be small, $|\psi(\mathbf{r})| \ll 1$, and slowly varying in space (on the microscale). The basic steps to

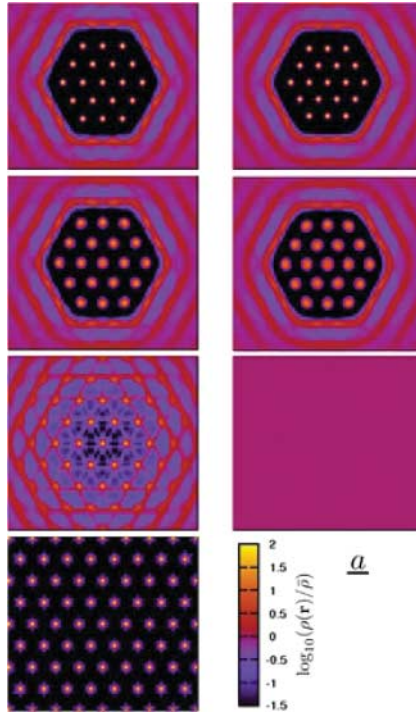


Figure 3. Crystallization starting at a colloidal cluster. The plots show DDFT results for the time-dependent density field. $A\rho_{\text{ref}} = 0.7$ (left column) and $A\rho_{\text{ref}} = 0.6$ (right column) at times $t/\tau_B = 0, 0.001, 0.1, 1$ (from top to bottom) with the area A of a unit cell of the imposed crystalline seed, the Brownian time τ_B , and the lattice constant $a = (2/(\sqrt{3}\rho_{\text{ref}}))^{1/2}$. For $A\rho_{\text{ref}} = 0.7$, the cluster is compressed in comparison to the stable bulk crystal, but there is still crystal growth possible. The initial nucleus first melts, but then an inner crystalline nucleus is formed (third panel from the top), which acts as a seed for further crystal growth. For $A\rho_{\text{ref}} = 0.6$, the compression is too high and the initial nucleus melts. (Reproduced from van Teeffelen *et al.* [129] © 2008 by the American Physical Society.)

derive the PFC free energy are threefold: (i) insert the parametrization (34) into the (microscopic) free-energy functional (5), (ii) Taylor-expand systematically in terms of powers of $\psi(\mathbf{r})$, (iii) perform a gradient expansion [78,97,131–133] of $\psi(\mathbf{r})$. Consistent with the assumption that density deviations are small, the Ramakrishnan–Yussouff approximation (11) is used as a convenient approximation for the free-energy functional.

For the local ideal gas free-energy functional (6) this yields⁶

$$\mathcal{F}_{\text{id}}[\psi(\mathbf{r})] = F_0 + \rho_{\text{ref}}k_B T \int d\mathbf{r} \left(\psi + \frac{\psi^2}{2} - \frac{\psi^3}{6} + \frac{\psi^4}{12} \right) \quad (35)$$

with the irrelevant constant $F_0 = \rho_{\text{ref}}V k_B T (\ln(\Lambda^3 \rho_{\text{ref}}) - 1)$. The Taylor expansion is performed up to the fourth order, since this is the lowest order which enables the formation of stable crystalline phases. The non-local Ramakrishnan–Yussouff approximation (11) for the approximation of the excess free-energy functional $\mathcal{F}_{\text{exc}}[\psi(\mathbf{r})]$ is gradient-expanded to make it local. For this purpose, it is important to note that – in the fluid bulk reference state – the direct pair-correlation function $c^{(2)}(\mathbf{r}_1 - \mathbf{r}_2)$ entering into the Ramakrishnan–Yussouff theory has the same symmetry as the interparticle interaction potential $U_2(\mathbf{r}_1 - \mathbf{r}_2)$. For radially symmetric interactions (i.e. spherical

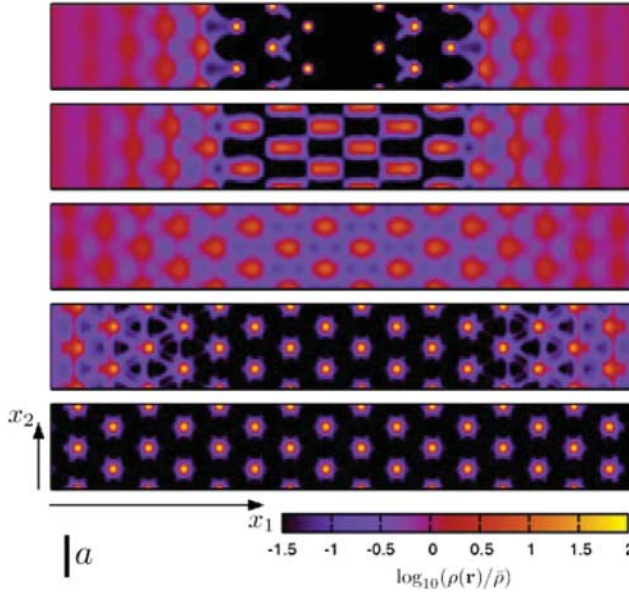


Figure 4. Crystallization starting at two triple-rows of hexagonally crystalline particles that are separated by a gap. The contour plots show the density field of a growing crystal at times $t/\tau_B = 0, 0.01, 0.1, 0.63, 1$ (from top to bottom). (Reproduced from van Teeffelen *et al.* [129] © 2008 by the American Physical Society.)

particles), there is both *translational* and *rotational* invariance implying

$$c^{(2)}(\mathbf{r}_1, \mathbf{r}_2) \equiv c^{(2)}(\mathbf{r}_1 - \mathbf{r}_2) \equiv c^{(2)}(r) \quad (36)$$

with the relative distance $r = |\mathbf{r}_1 - \mathbf{r}_2|$. Then, as a consequence of Equation (36), the Ramakrishnan–Yussouff approximation is a convolution integral. Consequently, a Taylor expansion of the Fourier transform $\tilde{c}^{(2)}(\mathbf{k})$ of the direct correlation function in Fourier space (around the wave vector $\mathbf{k} = \mathbf{0}$)

$$\tilde{c}^{(2)}(\mathbf{k}) = \tilde{c}_0^{(2)} + \tilde{c}_2^{(2)} \mathbf{k}^2 + \tilde{c}_4^{(2)} \mathbf{k}^4 + \dots \quad (37)$$

with expansion coefficients $\tilde{c}_i^{(2)}$ becomes a gradient expansion in real space

$$c^{(2)}(\mathbf{r}) = c_0^{(2)} - c_2^{(2)} \nabla_{\mathbf{r}}^2 + c_4^{(2)} \nabla_{\mathbf{r}}^4 \mp \dots \quad (38)$$

with the gradient expansion coefficients $c_i^{(2)}$. Clearly, gradients of odd order vanish due to parity inversion symmetry $c^{(2)}(-\mathbf{r}) = c^{(2)}(\mathbf{r})$ of the direct pair-correlation function.

The gradient expansion up to the fourth order is the lowest one that makes stable periodic density fields possible. We finally obtain

$$\mathcal{F}_{\text{exc}}[\psi(\mathbf{r})] = F_{\text{exc}} - \frac{\rho_{\text{ref}}}{2} k_B T \int d\mathbf{r} (A_1 \psi^2 + A_2 \psi \nabla_{\mathbf{r}}^2 \psi + A_3 \psi \nabla_{\mathbf{r}}^4 \psi) \quad (39)$$

with the irrelevant constant $F_{\text{exc}} = \mathcal{F}_{\text{exc}}^{(0)}(\rho_{\text{ref}})$ and the coefficients

$$A_1 = 4\pi\rho_{\text{ref}} \int_0^\infty dr r^2 c^{(2)}(r), \quad A_2 = \frac{2}{3}\pi\rho_{\text{ref}} \int_0^\infty dr r^4 c^{(2)}(r), \quad A_3 = \frac{\pi\rho_{\text{ref}}}{30} \int_0^\infty dr r^6 c^{(2)}(r) \quad (40)$$

that are moments of the fluid direct correlation function $c^{(2)}(r)$.

Finally, the external free-energy functional (7) can be written as

$$\mathcal{F}_{\text{ext}}[\psi(\mathbf{r})] = F_{\text{ext}} + \rho_{\text{ref}} \int d\mathbf{r} \psi(\mathbf{r}) U_1(\mathbf{r}) \quad (41)$$

with the irrelevant constant $F_{\text{ext}} = \rho_{\text{ref}} \int d\mathbf{r} U_1(\mathbf{r})$. We add as a comment here that this external part is typically neglected in most of the PFC calculations. Altogether, we obtain

$$\mathcal{F}[\psi(\mathbf{r})] = \rho_{\text{ref}} k_B T \int d\mathbf{r} \left(A'_1 \psi^2 + A'_2 \psi \nabla_{\mathbf{r}}^2 \psi + A'_3 \psi \nabla_{\mathbf{r}}^4 \psi - \frac{\psi^3}{6} + \frac{\psi^4}{12} \right) \quad (42)$$

for the total Helmholtz free-energy functional and the scaled coefficients

$$A'_1 = \frac{1}{2}(1 - A_1), \quad A'_2 = -\frac{1}{2}A_2, \quad A'_3 = -\frac{1}{2}A_3 \quad (43)$$

are used for abbreviation, where the coefficient A'_2 should be positive in order to favour non-uniform phases and the last coefficient A'_3 is assumed to be positive for stability reasons. By comparison of Equation (42) with the original PFC model (1), that was initially proposed on the basis of general symmetry considerations in reference [12], analytic expressions can be assigned to the unknown coefficients in the original PFC model: when we write the order-parameter field in Equation (1) as $\tilde{\psi}(\mathbf{r}) = \alpha(1 - 2\psi(\mathbf{r}))$ with a constant α and neglect constant contributions as well as terms linear in $\psi(\mathbf{r})$ in the free-energy density, we obtain the relations

$$\alpha = \frac{1}{\sqrt{24A'_3}}, \quad \tilde{\mathcal{F}} = \frac{1}{12\rho_{\text{ref}} k_B T A_3^2} \mathcal{F}, \quad \beta = \frac{1}{8A'_3} - \frac{A'_1}{A'_3} + \frac{A_2^2}{4A_3^2}, \quad k_0 = \sqrt{\frac{A'_2}{2A'_3}} \quad (44)$$

between the coefficients in Equations (1) and (42).⁷

2.3.2. Dynamical equations

We turn to the dynamics of the PFC model and derive it here from DDFT. Inserting the representation (34) for the one-particle density field into the DDFT equation (15), we obtain for the dynamical evolution of the order-parameter field $\psi(\mathbf{r}, t)$

$$\frac{\partial \psi(\mathbf{r}, t)}{\partial t} = D_T \nabla_{\mathbf{r}} \cdot \left((1 + \psi) \nabla_{\mathbf{r}} \left(2A'_1 \psi + 2A'_2 \nabla_{\mathbf{r}}^2 \psi + 2A'_3 \nabla_{\mathbf{r}}^4 \psi - \frac{\psi^2}{2} + \frac{\psi^3}{3} \right) \right). \quad (45)$$

This dynamical equation (called PFC1 model in reference [79]) still differs from the original dynamical equation of the PFC model. The latter can be gained by a further constant-mobility approximation (CMA), where the space- and time-dependent mobility $D_T \rho(\mathbf{r}, t)$ in the DDFT equation is replaced by the constant mobility $D_T \rho_{\text{ref}}$. The resulting dynamical equation (called PFC2 model in reference [79]) coincides with the original PFC dynamics given by

$$\frac{\partial \psi(\mathbf{r}, t)}{\partial t} = D_T \nabla_{\mathbf{r}}^2 \left(2A'_1 \psi + 2A'_2 \nabla_{\mathbf{r}}^2 \psi + 2A'_3 \nabla_{\mathbf{r}}^4 \psi - \frac{\psi^2}{2} + \frac{\psi^3}{3} \right) \quad (46)$$

for the time-dependent translational density $\psi(\mathbf{r}, t)$. We remark that this dynamical equation can also be derived from an equivalent dissipation functional \mathfrak{R} known from linear irreversible thermodynamics [135–137]. A further transformation of this equation to the standard form of the dynamic PFC model will be established in Section 3.1.1.

2.3.3. Colloidal crystal growth: DDFT versus PFC modelling

Results of the PFC1 model, the PFC2 model, and DDFT are compared for colloidal crystal growth in reference [79]. Figures 5–7 show the differences for the example of a growing crystal front starting at the edge of a prescribed hexagonal crystal. The underlying colloidal systems are the same as in Section 2.2.4. In Figure 5, the time evolution of the one-particle density is shown for DDFT and for the PFC1 model. The PFC2 model leads to results very similar to those for the PFC1 model and is therefore not included in this figure.

Two main differences in the results of DDFT and of the PFC1 model are obvious: first, the density peaks are much higher and narrower in the DDFT results than for the PFC1 model. While these peaks can be approximated by Gaussians in the case of DDFT, they are much broader

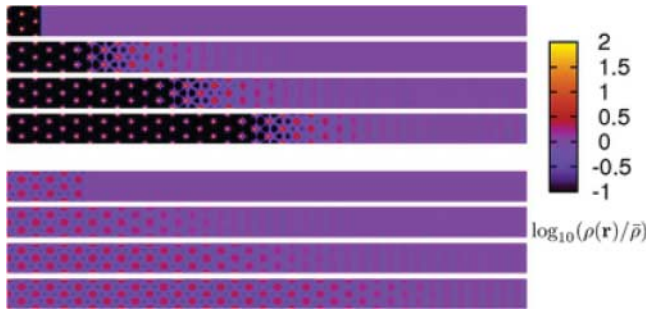


Figure 5. Colloidal crystal growth within DDFT (upper panel) and the PFC1 model (lower panel). The crystallization starts with an initial nucleus of 5 and 11 rows of hexagonally crystalline particles, respectively. The density field of the growing crystal is shown at times $t/\tau_B = 0, 0.5, 1, 1.5$. (Reproduced from van Teeffelen *et al.* [79] © 2009 by the American Physical Society.)

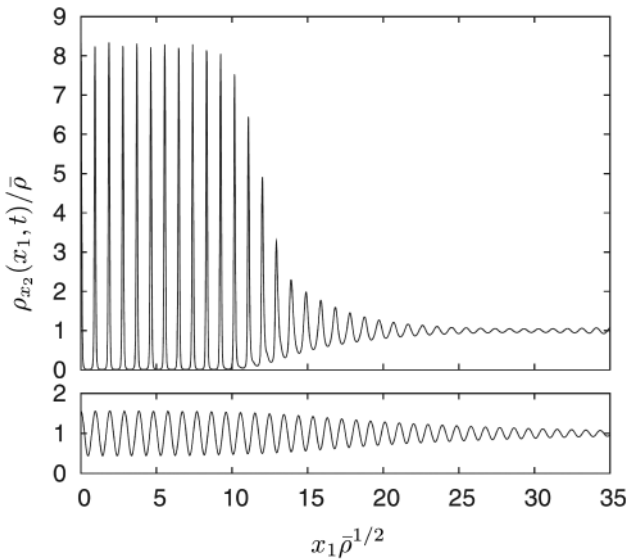


Figure 6. Comparison of DDFT (upper panel) and PFC1 (lower panel) results. For an analogous situation as in Figure 5, this plot shows the laterally averaged density $\rho_{x_2}(x_1, t) = \langle \rho(\mathbf{r}, t) \rangle_{x_2}$ at $t = \tau_B$. (Reproduced from van Teeffelen *et al.* [79] © 2009 by the American Physical Society.)

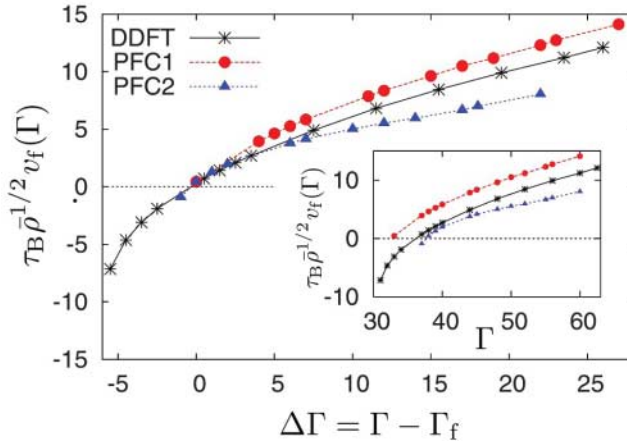


Figure 7. Comparison of DDFT, the PFC1 model, and the PFC2 model [79]. The plot shows the velocity v_f of a crystallization front in the (11)-direction in dependence of the relative coupling constant $\Delta\Gamma = \Gamma - \Gamma_f$ with the total coupling constant Γ and the coupling constant of freezing Γ_f . In the inset, the velocity v_f is shown in dependence of Γ . (Reproduced from van Teeffelen *et al.* [79] © 2009 by the American Physical Society.)

sinusoidal modulations for the PFC1 model. Second, also the width of the crystal front obtained within DDFT is considerably smaller than in the PFC approach.

These qualitative differences can also be observed in Figure 6. There, the laterally averaged density $\rho_{x_2}(x_1, t) = \langle \rho(\mathbf{r}, t) \rangle_{x_2}$ associated with the plots in Figure 5 is shown, where $\langle \cdot \rangle_{x_2}$ denotes an average with respect to x_2 . A further comparison of DDFT and the PFC approaches is possible with respect to the velocity v_f of the crystallization front. The corresponding results are shown in Figure 7 in dependence of the total coupling constant $\Gamma = u_0 v^{3/2} / (k_B T)$ and the relative coupling constant $\Delta\Gamma = \Gamma - \Gamma_f$, where Γ_f denotes the coupling constant of freezing. Due to the power-law potential of the considered colloidal particles, their behaviour is completely characterized by the dimensionless coupling parameter Γ . When plotted versus $\Delta\Gamma$, the growth velocity of the PFC1 model is in slightly better agreement than that of the PFC2 model.

3. Phase-field-crystal modelling in condensed matter physics

The original PFC model has the advantage over most other microscopic techniques, such as MD simulations, that the time evolution of the system can be studied on the diffusive time scale making the long-time behaviour and the large-scale structures accessible [12,59]. As already outlined in Section 2.2, we note that the diffusion-controlled relaxation dynamics the original PFC model assumes is relevant for micron-scale colloidal particles in carrier fluid [79,129], where the self-diffusion of the particles is expected to be the dominant way of the density relaxation. For normal liquids, the hydrodynamic mode of density relaxation is expected to dominate. The modified PFC (MPFC) model introduces linearized hydrodynamics, realized via incorporating a term proportional to the second time derivative of the particle density into the EOM [61,138], yielding a two-time-scale density relaxation: a fast acoustic process in addition to the long-time diffusive relaxation of the original PFC model. A three-time-scale extension incorporates phonons into the PFC model [139,140]. Another interesting group of models have been obtained by coarse-graining the PFC approaches [19,20,141], leading to equations of motion that describe the spatio-temporal evolution of the Fourier amplitudes and the respective phase information characterizing the particle

density field. Combined with adaptive grid schemes, the amplitude equation models are expected to become a numerically especially efficient class of the PFC models of crystallization [20].

Finally, we address here recent advances in the modelling of molecules or liquid crystalline systems, which are composed of anisotropic particles. There is a large number of molecular and colloidal realizations of these non-spherical particles. The simplest non-spherical shape is rotationally symmetric about a certain axis (like rods, platelets, and dumbbells) and is solely described by an additional orientation vector. Liquid crystalline systems show an intricate freezing behaviour in equilibrium, where mesophases occur, that can possess both orientational and translational ordering. Here, we show that the microscopic DFT approach for liquid crystals provides an excellent starting point to derive PFC-type models for liquid crystals. This gives access to the phase diagram of liquid crystalline phases and to their dynamics promising a flourishing future to predict many fundamentally important processes on the microscopic level.

3.1. The original PFC model and its generalizations

The original PFC model has several equivalent formulations and extensions that we review in this section. We first address the single-component PFC models. Then, an overview of their binary generalizations will be given. In both cases, complementing Section 2, we start with presenting different forms of the free-energy functional, followed by a summary of specific forms of the EOM and of the Euler–Lagrange equation (ELE). Finally, we review the numerical methods applied for solving the EOM and ELE as well as various approaches for the amplitude equations.

3.1.1. Single-component PFC models

3.1.1.1 *The free energy. The single-mode PFC model:* The earliest formulation of the single-mode PFC (1M-PFC) model [12,59] has been derived as a SH model with conserved dynamics to incorporate mass conservation. Accordingly, the dimensionless free energy of the heterogeneous system is given by the usual SH expression (1). We note that in Equations (1) and (8) the analogous quantities differ by only appropriate numerical factors originating from the difference in the length scales.

As already outlined in Section 2.3, the free energy of the earliest and simplest PFC model [12] has been re-derived [26] from that of the perturbative DFT of Ramakrishnan and Yussouff [94], in which the free-energy difference $\Delta\mathcal{F} = \mathcal{F} - \bar{\mathcal{F}}^8$ of the crystal relative to a reference liquid of particle density ρ_{ref} and free energy $\bar{\mathcal{F}}$ is expanded with respect to the local density difference $\Delta\rho(\mathbf{r}) = \rho(\mathbf{r}) - \rho_{\text{ref}}$, while retaining the terms up to the two-particle term (Section 2.3.1):

$$\frac{\mathcal{F}}{k_{\text{B}}T} = \int d\mathbf{r} \left(\rho \ln \left(\frac{\rho}{\rho_{\text{ref}}} \right) - \Delta\rho \right) - \frac{1}{2} \int d\mathbf{r}_1 \int d\mathbf{r}_2 \Delta\rho(\mathbf{r}_1) c^{(2)}(\mathbf{r}_1, \mathbf{r}_2) \Delta\rho(\mathbf{r}_2) + \dots \quad (47)$$

Fourier expanding the particle density, one finds that for the solid $\rho_s = \rho_{\text{ref}}(1 + \eta_s + \sum_{\mathbf{K}} A_{\mathbf{K}} \exp(i\mathbf{K} \cdot \mathbf{r}))$, where η_s is the fractional density change upon freezing, while \mathbf{K} are reciprocal lattice vectors (RLVs) and $A_{\mathbf{K}}$ the respective Fourier amplitudes. Introducing the reduced number density $\psi = (\rho - \rho_{\text{ref}})/\rho_{\text{ref}} = \eta_s + \sum_{\mathbf{K}} A_{\mathbf{K}} \exp(i\mathbf{K} \cdot \mathbf{r})$ one obtains

$$\begin{aligned} \frac{\mathcal{F}}{\rho_{\text{ref}} k_{\text{B}}T} &= \int d\mathbf{r} ((1 + \psi) \ln(1 + \psi) - \psi) \\ &\quad - \frac{\rho_{\text{ref}}}{2} \int d\mathbf{r}_1 \int d\mathbf{r}_2 \psi(\mathbf{r}_1) c^{(2)}(|\mathbf{r}_1 - \mathbf{r}_2|) \psi(\mathbf{r}_2) + \dots \end{aligned} \quad (48)$$

Expanding next $c^{(2)}(|\mathbf{r}_1 - \mathbf{r}_2|)$ in Fourier space, $\tilde{c}^{(2)}(k) \approx \tilde{c}_0^{(2)} + \tilde{c}_2^{(2)}k^2 + \tilde{c}_4^{(2)}k^4 + \dots$, where $\tilde{c}^{(2)}(k)$ has its first peak at $k = 2\pi/R_p$, the signs of the coefficients alternate. (Here, R_p is the

interparticle distance.) Introducing the dimensionless two-particle direct correlation function $c(k) = \rho_{\text{ref}} \tilde{c}^{(2)}(k) \approx \sum_{j=0}^m c_{2j} k^{2j} = \sum_{j=0}^m b_{2j} (kR_p)^{2j}$, which is related to the structure factor as $S(k) = 1/(1 - c(k))$, and integrating the second term on the right-hand-side of Equation (48) with respect to \mathbf{r}_2 and finally replacing \mathbf{r}_1 by \mathbf{r} , the free-energy difference can be rewritten as

$$\frac{\mathcal{F}}{\rho_{\text{ref}} k_B T} \approx \int d\mathbf{r} \left((1 + \psi) \ln(1 + \psi) - \psi - \frac{\psi}{2} \left(\sum_{j=0}^m (-1)^j c_{2j} \nabla_{\mathbf{r}}^{2j} \right) \psi \right). \quad (49)$$

The reference liquid is not necessarily the initial liquid. Thus, we have here two parameters to control the driving force for solidification: the initial liquid number density ρ_0 (corresponding to a reduced initial density of ψ_0) and the temperature T , if the direct correlation function depends on temperature. Taylor-expanding $\ln(1 + \psi)$ for small ψ one obtains

$$\frac{\mathcal{F}}{\rho_{\text{ref}} k_B T} \approx \int d\mathbf{r} \left(\frac{\psi^2}{2} - \frac{\psi^3}{6} + \frac{\psi^4}{12} - \frac{\psi}{2} \left(\sum_{j=0}^m (-1)^j c_{2j} \nabla_{\mathbf{r}}^{2j} \right) \psi \right). \quad (50)$$

For $m = 2$, corresponding to the earliest version of the PFC model [12], and taking the alternating sign of the expansion coefficients of $\tilde{c}_i^{(2)}$ into account, Equation (49) transforms to the following form:

$$\frac{\mathcal{F}}{\rho_{\text{ref}} k_B T} \approx \int d\mathbf{r} \left(\frac{\psi^2}{2} (1 + |b_0|) + \frac{\psi}{2} (|b_2| R_p^2 \nabla_{\mathbf{r}}^2 + |b_4| R_p^4 \nabla_{\mathbf{r}}^4) \psi - \frac{\psi^3}{6} + \frac{\psi^4}{12} \right). \quad (51)$$

Introducing the new variables

$$B_1 = 1 + |b_0| = 1 - c_0 \quad [= (1/\kappa)/(\rho_{\text{ref}} k_B T), \text{ where } \kappa \text{ is the compressibility}],$$

$$B_s = |b_2|^2 / (4|b_4|) \quad [= K/(\rho_{\text{ref}} k_B T), \text{ where } K \text{ is the bulk modulus}],$$

$$R = R_p (2|b_4|/|b_2|)^{1/2} \quad [= \text{the new length scale } (x = R\tilde{x}), \text{ which is now related to the position of the maximum of the Taylor expanded } \tilde{c}^{(2)}(k)],$$

and a multiplier v for the ψ^3 -term (that accounts for the zeroth-order contribution from three-particle correlations), one obtains the form used by Berry *et al.* [36,46]:

$$\mathcal{F} = \int d\mathbf{r} f[\psi] = \rho_{\text{ref}} k_B T \int d\mathbf{r} \left(\frac{\psi}{2} (B_1 + B_s (2R^2 \nabla_{\mathbf{r}}^2 + R^4 \nabla_{\mathbf{r}}^4)) \psi - v \frac{\psi^3}{6} + \frac{\psi^4}{12} \right). \quad (52)$$

Here, $f[\psi]$ denotes the full (dimensional) free-energy density. Note that the inclusion of the coefficient v into Equation (52) (and another coefficient for the fourth-order term) has been discussed in references [44,53,142,143]. Higher-order correlation functions are expected to contribute to these coefficients.

The SH-type dimensionless form: Introducing a new set of variables, $x = R\tilde{x}$, $\psi = (3B_s)^{1/2} \tilde{\psi}$, $\mathcal{F} = (3\rho_{\text{ref}} k_B T R^d B_s^2) \tilde{\mathcal{F}}$, where d is the number of spatial dimensions, the free energy can be transcribed into the following dimensionless form:

$$\tilde{\mathcal{F}} = \int d\tilde{\mathbf{r}} \left(\frac{\tilde{\psi}}{2} (-\epsilon + (1 + \nabla_{\tilde{\mathbf{r}}}^2)^2) \tilde{\psi} + p \frac{\tilde{\psi}^3}{3} + \frac{\tilde{\psi}^4}{4} \right). \quad (53)$$

Here, $p = -(v/2)(3/B_s)^{1/2} = -v(3|b_4|/|b_2|^2)^{1/2}$ and $\epsilon = -\Delta B/B_s = -((1 + |b_0|)/(|b_2|^2/(4|b_4|)) - 1)$, while $\tilde{\psi} = \psi/(3B_s)^{1/2}$. The quantities involved in Equation (53) are all dimensionless. Using the appropriate length unit, this expression becomes equivalent to Equation (1) for $p = 0$.

Equation (53) suggests that the $m = 2$ PFC model contains only two dimensionless similarity parameters, ϵ and p , composed of the original model parameters. We note finally that even the third-order term can be eliminated. In the respective $p' = 0$ SH model (1), the state ($\epsilon' = \epsilon + p^2/3$, $\psi' = \tilde{\psi} + p/3$) corresponds to the state ($\epsilon, \tilde{\psi}$) of the original $p \neq 0$ model. This transformation leaves the grand canonical potential difference, the ELE (Section 3.1.1.3), and the EOM (Section 3.1.1.2.) invariant. Accordingly, it is sufficient to address the case $p = 0$.

We stress here that in these models, the approximation for the two-particle direct correlation function leads to a well-defined wavelength of the density waves the system tends to realize (hence the name “single-mode PFC” (1M-PFC) model). Accordingly, any periodic density distribution that honours this wavelength represents a local minimum of the free energy. Indeed, the 1M-PFC model has stability domains for the bcc, fcc, and hcp structures (Section 3.1.1.1). Furthermore, elasticity and crystal anisotropies are automatically present in the model. Model parameters of the SH formulation have been deduced to fit into the properties of bcc Fe by Wu and Karma [40].

The two-mode PFC model: An attempt has been made to formulate a free energy that prefers the fcc structure at small ϵ values [144], where a linear elastic behaviour persists. To achieve this, two well defined wavelengths were used (first and second neighbour RLVs), hence the name “two-mode PFC” (2M-PFC) model. The respective free-energy functional contains two new parameters:

$$\tilde{\mathcal{F}} = \int d\tilde{\mathbf{r}} \left(\frac{\tilde{\psi}}{2} (-\epsilon + (1 + \nabla_{\tilde{\mathbf{r}}}^2)(R_1 + (k_{\text{rel}}^2 + \nabla_{\tilde{\mathbf{r}}}^2)^2)) \tilde{\psi} + \frac{\tilde{\psi}^4}{4} \right). \quad (54)$$

Here, R_1 controls the relative stability of the fcc and bcc structures, while k_{rel} is the ratio of the two wave numbers ($k_{\text{rel}} = 2/\sqrt{3}$ for fcc, using the (111) and (200) RLVs). Remarkably, the 1M-PFC model can be recovered for $R_1 \rightarrow \infty$. Model parameters have been deduced to fit into the properties of fcc Fe by Wu and Karma [144].

We note finally that the 1M-PFC and 2M-PFC models can be cast into a form that interpolates between them by varying a single parameter $\lambda = R_1/(1 + R_1) \in [0, 1]$ as follows [35]:

$$\tilde{\mathcal{F}} = \int d\tilde{\mathbf{r}} \left(\frac{\tilde{\psi}}{2} (-\epsilon + (1 + \nabla_{\tilde{\mathbf{r}}}^2)(\lambda + (1 - \lambda)(k_{\text{rel}}^2 + \nabla_{\tilde{\mathbf{r}}}^2)^2)) \tilde{\psi} + \frac{\tilde{\psi}^4}{4} \right). \quad (55)$$

This expression recovers the 1M-PFC model limit for $\lambda = 1$ ($R_1 \rightarrow \infty$).

The eighth-order fitting PFC model: To approximate real bcc materials better, an eighth-order expansion of the Fourier transform of the direct correlation function around its maximum ($k = k_m$) has been performed recently, leading to what is termed the eighth-order fitting version of the phase-field-crystal (EOF-PFC) model [142]:

$$\tilde{c}^{(2)}(k) \approx \tilde{c}^{(2)}(k_m) - \Gamma \left(\frac{k^2}{k_m^2} - 1 \right)^2 - E_B \left(\frac{k^2}{k_m^2} - 1 \right)^4. \quad (56)$$

The expansion parameters were then fixed so that the position, height, and the second derivative of $\tilde{c}^{(2)}(k)$ are accurately recovered. This is ensured by

$$\Gamma = -\frac{k_m^2 (\tilde{c}^{(2)})''(k_m)}{8} \quad \text{and} \quad E_B = \tilde{c}^{(2)}(k_m) - \tilde{c}^{(2)}(0) - \Gamma. \quad (57)$$

With this choice of the model parameters and using relevant data for Fe from reference [40], they reported a fair agreement with MD simulation results for the volume change upon melting, the bulk moduli of the liquid and solid phases, and for the magnitude and anisotropy of the bcc-liquid interfacial free energy [142].

Attempts to control the crystal structure in PFC models: Greenwood and co-workers [145,146] (GRP-PFC model) have manipulated the two-particle direct correlation function so that its peaks prefer the desired structural correlations – an approach that enables them to study transitions between the bcc, fcc, hcp, and sc structures. Wu *et al.* [147] have investigated the possibility to control crystal symmetries within the PFC method via tuning nonlinear resonances. They have proposed a general recipe for developing free-energy functionals that realize coexistence between the liquid and periodic phases of desired crystal symmetries, and have illustrated this via presenting a free-energy functional that leads to square-lattice-liquid coexistence in 2D. A possible extension of the method to the 3D case for simple cubic (sc) structures has also been discussed.

The vacancy PFC model: The vacancy PFC (VPFC) model is an important extension of the PFC model that adds a term to the free energy that penalizes the negative values of the particle density, allowing thus for an explicit treatment of vacancies [65]:

$$\tilde{\mathcal{F}} = \int d\tilde{\mathbf{r}} \left(\frac{\tilde{\psi}}{2} (-\beta + (k_0^2 + \nabla_{\tilde{\mathbf{r}}}^2)^2) \tilde{\psi} + \frac{\tilde{\psi}^4}{4} + h(|\tilde{\psi}^3| - \tilde{\psi}^3) \right). \quad (58)$$

Here, h in the last term on the right-hand-side is a constant. The new term is a piecewise function that is zero for $\tilde{\psi} > 0$ and positive for $\tilde{\psi} < 0$. It is then possible to obtain a mixture of density peaks (particles) and vacant areas (where $\tilde{\psi} \approx 0$), resembling thus to snapshots of liquid configurations or crystalline structures with defects. This allows structural modelling of the fluid phase and is an important step towards combining the PFC model with fluid flow. The same approach has been used to address the dynamics of glasses [47].

The anisotropic PFC model: Recently, Prieler *et al.* [148] have extended the PFC approach by replacing the Laplacian in Equation (1) by more general differential operators allowing spatial anisotropy. Doing so and setting $\tau = -(k_0^2 - \beta)$ one arrives at the dimensionless free-energy functional of the so-called anisotropic PFC (APFC) model:

$$\tilde{\mathcal{F}} = \int d\tilde{\mathbf{r}} \left(\frac{\tilde{\psi}}{2} \left(-\tau + a_{ij} \frac{\partial^2}{\partial \tilde{x}_i \partial \tilde{x}_j} + b_{ijkl} \frac{\partial^4}{\partial \tilde{x}_i \partial \tilde{x}_j \partial \tilde{x}_k \partial \tilde{x}_l} \right) \tilde{\psi} + \frac{\tilde{\psi}^4}{4} \right). \quad (59)$$

Here, a_{ij} is a symmetric matrix and b_{ijkl} is a tensor of rank 4 with the symmetry of an elastic tensor: $i \leftrightarrow j, k \leftrightarrow l, (i, j) \leftrightarrow (k, l)$ [148]. Choudhary *et al.* [149,150] proved that based on a functional of the form (59) further crystal lattices can be assessed as hexagonal, bcc, and corresponding sheared structures, for which they have presented the elastic parameters and identified the stationary states.

3.1.1.2 The equation of motion. In the PFC models, different versions of the EOM have been employed. In all cases, conservative dynamics is assumed on the ground that mass conservation needs to be satisfied. (The original SH model differs from the 1M-PFC model only in the EOM, for which the SH model assumes non-conserved dynamics.) Most of the PFC models rely on an overdamped conservative EOM [12,26–39,43,46,59,79,144,148,151]. In fact, this means that the particle density relaxes diffusively, a feature more characteristic to colloidal systems than to molten metals: in colloidal systems of particles floating in a carrier fluid, Brownian motion is the dominant mechanism of particle motion, whose properties are captured reasonably well by overdamped dynamics [38,79,129] (see also Section 2.2). On the contrary, in molten metals density deficit can be reduced by hydrodynamic flow of particles. Apparently, a proper dynamics of the solid (presence of phonons) requires three time scales [139,140]. While the overdamped model has only the long diffusive time scale, the MPFC model realizes linearized hydrodynamics via adding a term proportional to the second time derivative of the density field. This new term leads to the appearance of an acoustic relaxation of the density (not true acoustic phonons) on a fast time

scale, in addition to the slow diffusive relaxation at later stages [61,138]. In a recent work, phonon dynamics, that acts on a third time scale, has also been introduced into the PFC model [139]. It has been shown that there exists a scale window, in which the longitudinal part of the full three-scale model reduces to the MPFC model, whereas the linearized hydrodynamics of the latter converges to the diffusive dynamics of the original PFC model for sufficiently long times [139,140].

The overdamped EOM: In the majority of the PFC simulations, an overdamped conserved dynamics is assumed [that is analogous to the DDFE EOM (15) for colloidal systems, however, assuming here a constant mobility coefficient, $M_\rho = \rho_0 D_T / (k_B T)$]. Accordingly, the (dimensional) EOM has the form

$$\frac{\partial \rho}{\partial t} = \nabla_{\mathbf{r}} \cdot \left(M_\rho \nabla_{\mathbf{r}} \frac{\delta \mathcal{F}}{\delta \rho} \right) + \zeta_\rho, \quad (60)$$

where ζ_ρ stands for the fluctuations of the density flux, whose correlator reads as $\langle \zeta_\rho(\mathbf{r}, t) \zeta_\rho(\mathbf{r}', t') \rangle = -2M_\rho k_B T \nabla_{\mathbf{r}}^2 \delta(\mathbf{r} - \mathbf{r}') \delta(t - t')$. (For a discretized form of the conserved noise, see references [152–154].)

Changing from variable ρ to ψ , introducing $M_\psi = ((1 + \psi_0) D_T / (\rho_{\text{ref}} k_B T))$, scaling time and distance as $t = \tau \tilde{t}$ and $x = R_p \tilde{x}$, where $\tau = R_p / (D_T (1 + \psi_0))$, and inserting the free energy from Equation (51), one obtains the following dimensionless EOM:

$$\frac{\partial \psi}{\partial \tilde{t}} = \nabla_{\tilde{\mathbf{r}}}^2 \left(\psi (1 + |b_0|) + \sum_{j=1}^m |b_{2j}| \nabla_{\tilde{\mathbf{r}}}^{2j} \psi - \frac{\psi^2}{2} + \frac{\psi^3}{3} \right) + \zeta_\psi \quad (61)$$

with $\langle \zeta_\psi(\tilde{\mathbf{r}}, \tilde{t}) \zeta_\psi(\tilde{\mathbf{r}}', \tilde{t}') \rangle = -(2 / (\rho_{\text{ref}} R_p^d)) \nabla_{\tilde{\mathbf{r}}}^2 \delta(\tilde{\mathbf{r}} - \tilde{\mathbf{r}}') \delta(\tilde{t} - \tilde{t}')$. Analogously, the EOM corresponding to Equation (52) has the form

$$\frac{\partial \psi}{\partial t} = \nabla_{\mathbf{r}} \cdot \left(M_\psi \rho_{\text{ref}} k_B T \nabla_{\mathbf{r}} \left((B_1 + B_s (R^2 \nabla_{\mathbf{r}}^2 + R^4 \nabla_{\mathbf{r}}^4)) \psi - v \frac{\psi^2}{2} + \frac{\psi^3}{3} \right) \right) + \zeta'_\psi, \quad (62)$$

where $\langle \zeta'_\psi(\mathbf{r}, t) \zeta'_\psi(\mathbf{r}', t') \rangle = -2M_\psi k_B T \nabla_{\mathbf{r}}^2 \delta(\mathbf{r} - \mathbf{r}') \delta(t - t')$.

Dimensionless form in SH fashion: Introducing the variables $t = \tau \tilde{t}$, $x = R \tilde{x}$, and $\psi = (3B_s)^{1/2} \tilde{\psi} = (3B_s)^{1/2} (\psi' - p/3)$ into Equation (62), where $\tau = R^2 / (B_s M_\psi \rho_{\text{ref}} k_B T)$, the EOM can be written in the form

$$\frac{\partial \psi'}{\partial \tilde{t}} = \nabla_{\tilde{\mathbf{r}}}^2 ((-\epsilon' + (1 + \nabla_{\tilde{\mathbf{r}}}^2)^2) \psi' + \psi'^3) + \zeta, \quad (63)$$

where $\epsilon' = \epsilon + p^2/3 = -(\Delta B - (v/2)^2) / B_s = -((1 + |b_0|) / (|b_2|^2 / (4|b_4|)) - (1 + v^2 (|b_4| / |b_2|^2)))$ and the dimensionless noise strength is $\alpha = 2 / (3B_s^2 \rho_{\text{ref}} R^d) = 2^{5-d/2} |b_4|^{2-d/2} / (3R_p^d \rho_{\text{ref}} |b_2|^{4-d/2})$, while the correlator for the dimensionless noise reads as $\langle \zeta(\tilde{\mathbf{r}}, \tilde{t}) \zeta(\tilde{\mathbf{r}}', \tilde{t}') \rangle = -\alpha \nabla_{\tilde{\mathbf{r}}}^2 \delta(\tilde{\mathbf{r}} - \tilde{\mathbf{r}}') \delta(\tilde{t} - \tilde{t}')$.

Summarizing, the dynamical $m = 2$ 1M-PFC model has two dimensionless similarity parameters ϵ' and α composed of the original (physical) model parameters. This is the generic form of the $m = 2$ 1M-PFC model; some other formulations [36,46] can be transformed into this form.

The MPFC model: Acoustic relaxation has been partly incorporated by applying an underdamped EOM. Stefanovic *et al.* [61] have incorporated a second order time derivative into the

EOM of their MPFC model, which extends the previous PFC formalism by generating dynamics on two time scales:

$$\frac{\partial^2 \rho}{\partial t^2} + \kappa \frac{\partial \rho}{\partial t} = \lambda^2 \frac{\delta \mathcal{F}}{\delta \rho}, \quad (64)$$

where κ and λ are constants. At early times, molecular positions relax fast, consistently with elasticity theory, whereas at late times diffusive dynamics dominates the kinetics of phase transformations, the diffusion of vacancies, the motion of grain boundaries, and dislocation climb. In other words, elastic interactions mediated by wave modes have been incorporated, which travel on time scales that are orders of magnitude slower than the molecular vibrations yet considerably faster than the diffusive time scale. A similar EOM has been proposed for the VPFC model, whose free-energy functional forces the order parameter to be non-negative. The resulting approach dictates the number of atoms and describes the motion of each of them. Solution of the respective EOM might be viewed as essentially performing MD simulations on diffusive time scales [65]. A similar approach has been adapted to study the dynamics of monatomic and binary glasses, however, using the MPFT-type free-energy functionals and temperature-dependent noise terms [47].

3.1.1.3 The Euler–Lagrange equation. The ELE can be used to study equilibrium features including the mapping of the phase diagram [28] as well as the evaluation of the free energy of the liquid–solid interface [28] and of the nucleation barrier [35]. We note that noise may influence the phase diagram and other physical properties. Therefore, the results from the ELE and EOM are expected to converge for $\zeta \rightarrow 0$. We also call attention to the fact that so far as the equilibrium results (obtained by ELE) are concerned, the SH and 1M-PFC models are equivalent.

Once the free-energy functional is defined for the specific PFC model, its extremes can be found by solving the respective ELE, which reads as

$$\left. \frac{\delta \tilde{\mathcal{F}}}{\delta \tilde{\psi}} = \frac{\delta \tilde{\mathcal{F}}}{\delta \tilde{\psi}} \right|_{\tilde{\psi}_0}, \quad (65)$$

where $\tilde{\psi}_0$ is the reduced particle number density of the unperturbed initial liquid, while a no-flux boundary condition is prescribed at the boundaries of the simulation window ($\mathbf{n} \cdot \nabla_{\tilde{\mathbf{r}}} \tilde{\psi} = 0$ and $(\mathbf{n} \cdot \nabla_{\tilde{\mathbf{r}}}) \nabla_{\tilde{\mathbf{r}}}^2 \tilde{\psi} = 0$, where \mathbf{n} is the normal vector of the boundary). For example, inserting the 1M-PFC free energy and rearranging the terms, one arrives at

$$(-\epsilon + (1 + \nabla_{\tilde{\mathbf{r}}}^2)^2)(\tilde{\psi} - \tilde{\psi}_0) + p(\tilde{\psi}^2 - \tilde{\psi}_0^2) - (\tilde{\psi}^3 - \tilde{\psi}_0^3) = 0. \quad (66)$$

Equation (66) together with the boundary conditions represents a fourth-order boundary value problem (BVP).

Multiplicity of solutions of the ELE: It is worth noting that in the case of the PFC/SH-type models, a multiplicity of solutions can be usually found for the same BVP, defined by the boundary conditions and the ELE. This feature of the stationary solutions has been recently addressed in some detail in 2D for the SH [155] and in 1D for the VPFC [156] models. (Figure 8 illustrates this phenomenon via showing the bifurcation diagram for compact hexagonal clusters in the SH model [155].)

3.1.2. Binary PFC models

3.1.2.1 The free energy. Binary SH form: The earliest binary extension of the PFC model has been proposed in the seminal paper of Elder *et al.* [12] obtained by adding an interaction term

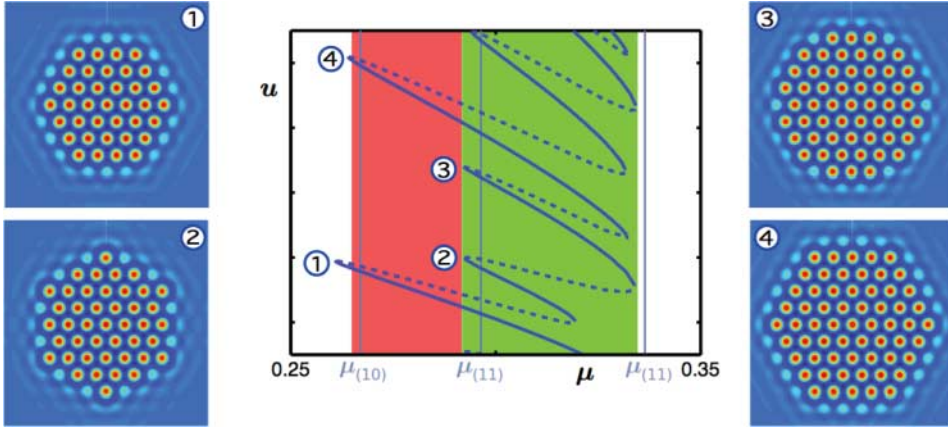


Figure 8. Multiplicity of localized hexagonal cluster solutions for the dynamic SH equation $\partial u/\partial t = -(1 + \nabla_{\mathbf{r}}^2)^2 u - \mu u + \nu u^2 - u^3$ with $\nu = 1.6$. The central panel displays a part of the bifurcation diagram for localized hexagonal patches (for details see reference [155]). The solid and dashed lines stand for the stable and unstable solutions, respectively. The vertical lines in grey correspond to the fold limits of planar (10) and (11) hexagon pulses. The red and green regions indicate where temporal self-completion does or does not occur, respectively. Panels 1–4 show colour plots of the hexagon patches at the inner and outer left folds. A different parametrization is used here: $\mu = -\epsilon + 3\psi_0^2$. (Reproduced with permission from Lloyd *et al.* [155] © 2008 by the Society for Industrial and Applied Mathematics.)

with coefficient A to the free energy of two mixed single-component SH free energies. Working with particle densities $\tilde{\psi}_1$ and $\tilde{\psi}_2$, this yields the free energy

$$\tilde{\mathcal{F}} = \int d\mathbf{r} \left(\frac{\tilde{\psi}_1}{2} (-\beta_1 + (k_1^2 + \nabla_{\mathbf{r}}^2)^2) \tilde{\psi}_1 + \frac{\tilde{\psi}_1^4}{4} + \frac{\tilde{\psi}_2}{2} (-\beta_2 + (k_2^2 + \nabla_{\mathbf{r}}^2)^2) \tilde{\psi}_2 + \frac{\tilde{\psi}_2^4}{4} + A \tilde{\psi}_1 \tilde{\psi}_2 \right). \tag{67}$$

Here, the physical properties (bulk moduli, lattice constants, etc.) of the individual species are controlled by the parameters with subscripts 1 and 2, respectively, and by the average values of the particle densities $\tilde{\psi}_1$ and $\tilde{\psi}_2$. It has been shown that the model can be used for studying structural phase transitions [12].

DFT-based binary PFC model: The most extensively used binary generalization of the 1M-PFC model has been derived starting from a binary perturbative DFT, where the free energy is Taylor expanded relative to the liquid state denoted by $\bar{\rho}_A$ and $\bar{\rho}_B$, respectively, up to the second order in the density differences $\Delta\rho_A = \rho_A - \bar{\rho}_A$ and $\Delta\rho_B = \rho_B - \bar{\rho}_B$ (up to two-particle correlations) [26]:

$$\begin{aligned} \frac{\mathcal{F}}{k_B T} = & \int d\mathbf{r} \left(\rho_A \ln \left(\frac{\rho_A}{\bar{\rho}_A} \right) - \Delta\rho_A + \rho_B \ln \left(\frac{\rho_B}{\bar{\rho}_B} \right) - \Delta\rho_B \right) \\ & - \frac{1}{2} \int d\mathbf{r}_1 \int d\mathbf{r}_2 (\Delta\rho_A(\mathbf{r}_1) c_{AA}^{(2)}(\mathbf{r}_1, \mathbf{r}_2) \Delta\rho_A(\mathbf{r}_2) \\ & + \Delta\rho_B(\mathbf{r}_1) c_{BB}^{(2)}(\mathbf{r}_1, \mathbf{r}_2) \Delta\rho_B(\mathbf{r}_2) + 2\Delta\rho_A(\mathbf{r}_1) c_{AB}^{(2)}(\mathbf{r}_1, \mathbf{r}_2) \Delta\rho_B(\mathbf{r}_2)). \end{aligned} \tag{68}$$

It is assumed here that all two-point correlation functions are isotropic, that is, $c_{ij}^{(2)}(\mathbf{r}_1, \mathbf{r}_2) = c_{ij}^{(2)}(|\mathbf{r}_1 - \mathbf{r}_2|)$. Taylor expanding the direct correlation functions in Fourier space up to fourth

order, one obtains $c_{ij}^{(2)}(|\mathbf{r}_1 - \mathbf{r}_2|) = (c_{ij,0}^{(2)} - c_{ij,2}^{(2)}\nabla_{\mathbf{r}_2}^2 + c_{ij,4}^{(2)}\nabla_{\mathbf{r}_2}^4)\delta(\mathbf{r}_1 - \mathbf{r}_2)$ in real space [26]. The partial direct correlation functions $c_{ij}^{(2)}$ can be related to the measured or computed partial structure factors.

Following Elder *et al.* [26], the reduced partial particle density differences are defined as $\psi_A = (\rho_A - \bar{\rho}_A)/\rho_0$ and $\psi_B = (\rho_B - \bar{\rho}_B)/\rho_0$, where $\rho_0 = \bar{\rho}_A + \bar{\rho}_B$. They have introduced then the new variables $\psi = \psi_A + \psi_B$ and $\hat{\psi} = (\psi_B - \psi_A) + (\bar{\rho}_B - \bar{\rho}_A)/\rho_0$, obtaining fields whose amplitude expansion yields field amplitudes resembling order parameters associated with structural and composition changes in the conventional PF models. Expanding the free energy around $\hat{\psi} = 0$ and $\psi = 0$, one obtains

$$\begin{aligned} \frac{\mathcal{F}}{\rho_{\text{ref}} k_B T} = \int d\mathbf{r} & \left(\frac{\psi}{2} (B_1 + B_s(2R^2\nabla_{\mathbf{r}}^2 + R^4\nabla_{\mathbf{r}}^4))\psi + s\frac{\psi^3}{3} + v\frac{\psi^4}{4} \right. \\ & \left. + \gamma\hat{\psi} + w\frac{\hat{\psi}^2}{2} + u\frac{\hat{\psi}^4}{4} + \frac{L^2}{2}(\nabla_{\mathbf{r}}\hat{\psi})^2 + \dots \right). \end{aligned} \quad (69)$$

This model has been used for studying a broad range of phase transitions, including the formation of solutal dendrites, eutectic structures [26,28], and the Kirkendall effect [64].

Binary PFC model for surface alloying: A somewhat different formulation of the binary model has been proposed to model compositional patterning in monolayer aggregates of binary metallic systems by Muralidharan and Haataja [48]:

$$\begin{aligned} \mathcal{F} = \int d\mathbf{r} & \left(\frac{\rho}{2}(\beta(c) + (k_c^2 + \nabla_{\mathbf{r}}^2)^2)\rho + \frac{\rho^4}{4} + V(c)\rho \right. \\ & \left. + f_0 \left(\frac{w_0^2}{2}(\nabla_{\mathbf{r}}c)^2 - \theta_c \frac{c^2}{2} + \frac{\theta}{2}((1+c)\ln(1+c) + (1-c)\ln(1-c)) \right) \right). \end{aligned} \quad (70)$$

In this construction, the values $c = \pm 1$ of the concentration field stand for different atomic species, $V(c)$ is the atom-specific substrate-film interaction, k_c incorporates the bulk lattice constant of different species, f_0 governs the relative strength of the elastic and chemical energies, while θ_c is the critical temperature, θ the scaled absolute temperature, and w_0 tunes the chemical contribution to the interface energy between different species. Starting from this free-energy functional, Muralidharan and Haataja have shown, that their PFC model incorporates competing misfit dislocations and alloying in a quantitative way, and then employed the model for investigating the misfit- and line tension dependence of the domain size [48].

3.1.2.2 *The equations of motion. Dimensionless binary form in the SH fashion:* The same type of overdamped conservative dynamics has been assumed for the two types of atoms [12]:

$$\frac{\partial \tilde{\psi}_1}{\partial t} = M_1 \nabla_{\mathbf{r}}^2 \frac{\delta \tilde{\mathcal{F}}}{\delta \tilde{\psi}_1} + \zeta_1 \quad \text{and} \quad \frac{\partial \tilde{\psi}_2}{\partial t} = M_2 \nabla_{\mathbf{r}}^2 \frac{\delta \tilde{\mathcal{F}}}{\delta \tilde{\psi}_2} + \zeta_2. \quad (71)$$

Here, M_i and ζ_i are the mobility and the noise term applying to species $i \in \{1, 2\}$.

DFT-based binary PFC model: In this widely used formulation of the binary 1M-PFC model, it is assumed that the same mobility M applies to the two species A and B (corresponding to substitutional diffusion) decoupling the dynamics of the fields ψ and $\hat{\psi}$. Assuming, furthermore, a constant effective mobility $M_e = 2M/\rho^2$ and conserved dynamics, the equations of motions for the two fields have the form [26]

$$\frac{\partial \psi}{\partial t} = M_e \nabla_{\mathbf{r}}^2 \frac{\delta \mathcal{F}}{\delta \psi} \quad \text{and} \quad \frac{\partial \hat{\psi}}{\partial t} = M_e \nabla_{\mathbf{r}}^2 \frac{\delta \mathcal{F}}{\delta \hat{\psi}}. \quad (72)$$

In general, the coefficients B_1 , B_s , and R in Equation (69) depend on $\hat{\psi}$. A Taylor expansion of $B_1(\hat{\psi})$, $B_s(\hat{\psi})$, and $R(\hat{\psi})$ in terms of $\hat{\psi}$ yields new coefficients B_i^l , B_i^s , and R_i with $i = 0, 1, 2, \dots$ that are independent of $\hat{\psi}$. Retaining only the coefficients B_0^l , B_2^l , B_0^s , R_0 , and R_1 , and inserting the free energy (69) into Equations (72), one obtains

$$\begin{aligned} \frac{\partial \psi}{\partial t} &= M_e \nabla_{\mathbf{r}}^2 (\psi (B_0^l + B_2^l \hat{\psi}^2) + s\psi^2 + v\psi^3 \\ &\quad + \frac{B_0^s}{2} (2(R_0 + R_1 \hat{\psi})^2 \nabla_{\mathbf{r}}^2 + (R_0 + R_1 \hat{\psi}^4) \nabla_{\mathbf{r}}^4) \psi \\ &\quad + \frac{B_0^s}{2} (2\nabla_{\mathbf{r}}^2 (\psi (R_0 + R_1 \hat{\psi})^2) + \nabla_{\mathbf{r}}^4 (\psi (R_0 + R_1 \hat{\psi})^4))), \end{aligned} \quad (73)$$

$$\begin{aligned} \frac{\partial \hat{\psi}}{\partial t} &= M_e \nabla_{\mathbf{r}}^2 (B_2^l \hat{\psi} \psi^2 + \gamma + w\hat{\psi} + u\hat{\psi}^3 - L^2 \nabla_{\mathbf{r}}^2 \hat{\psi} \\ &\quad + 2B_0^s \psi ((R_0 + R_1 \hat{\psi}) R_1 \nabla_{\mathbf{r}}^2 + (R_0 + R_1 \hat{\psi})^3 R_1 \nabla_{\mathbf{r}}^4) \psi). \end{aligned} \quad (74)$$

3.1.2.3 The Euler–Lagrange equations. Since the derivation of the ELE is straightforward for all the binary PFC models, we illustrate it for the most frequently used version deduced from the binary Ramakrishnan–Yussouff-type classical perturbative DFT. The extremum of the grand potential functional requires that its first functional derivatives are zero, that is,

$$\frac{\delta \mathcal{F}}{\delta \psi} = \frac{\delta \mathcal{F}}{\delta \psi} \Big|_{\psi_0, \hat{\psi}_0} \quad \text{and} \quad \frac{\delta \mathcal{F}}{\delta \hat{\psi}} = \frac{\delta \mathcal{F}}{\delta \hat{\psi}} \Big|_{\psi_0, \hat{\psi}_0}, \quad (75)$$

where ψ_0 and $\hat{\psi}_0$ are the total and relative particle densities for the homogeneous initial state. Inserting Equation (69) into Equation (75), one obtains after rearranging

$$\begin{aligned} &(B_1 \hat{\psi} + B_s R \hat{\psi}^2 (2\nabla_{\mathbf{r}}^2 + R \hat{\psi}^2 \nabla_{\mathbf{r}}^4) + \frac{B_s}{2} (2\nabla_{\mathbf{r}}^2 (R^2) + \nabla_{\mathbf{r}}^4 (R^4))) (\psi - \psi_0) \\ &= -s(\psi^2 - \psi_0^2) - v(\psi^3 - \psi_0^3), \end{aligned} \quad (76)$$

$$\begin{aligned} &L^2 \nabla_{\mathbf{r}}^2 \hat{\psi} - \frac{\partial B_1}{\partial \hat{\psi}} (\hat{\psi} \psi^2 - \hat{\psi}_0 \psi_0^2) - 2B_s R \frac{\partial R}{\partial \hat{\psi}} \psi (\nabla_{\mathbf{r}}^2 + R^2 \nabla_{\mathbf{r}}^4) \psi \\ &= w(\hat{\psi} - \hat{\psi}_0) + u(\hat{\psi}^3 - \hat{\psi}_0^3), \end{aligned} \quad (77)$$

where $R = R_0 + R_1 \hat{\psi}$. These equations are to be solved assuming no-flux boundary conditions at the border of the simulation box for both fields [$\mathbf{n} \cdot \nabla_{\mathbf{r}} \psi = 0$, $(\mathbf{n} \cdot \nabla_{\mathbf{r}}) \nabla_{\mathbf{r}}^2 \psi = 0$, $\mathbf{n} \cdot \nabla_{\mathbf{r}} \hat{\psi} = 0$, and $(\mathbf{n} \cdot \nabla_{\mathbf{r}}) \nabla_{\mathbf{r}}^2 \hat{\psi} = 0$].

3.1.3. PFC models for liquid crystals

Another level of complexity is to consider interactions between particles, that are not any longer spherically symmetric. The simplest case being the *oriented* particles, that is, particles with a fixed orientation along a given direction where the interaction $U_2(\mathbf{r}_1 - \mathbf{r}_2)$ is not any longer radially symmetric [as assumed in Equation (36)]. The derivation described in Section 2.3 was straightforwardly extended towards this case leading to a microscopic justification of the APFC model (59) proposed in Section 3.1.1.1. Clearly, the resulting crystal lattices are anisotropic,

which leads also to an anisotropic crystal growth. Much more complicated, however, is the case of *orientable* particles, which can adjust their orientation and form liquid crystalline mesophases.

Therefore, we now address orientable anisotropic particles, that possess orientational degrees of freedom. In order to keep the effort manageable, the particles are assumed to be uniaxial, that is, they are rotationally symmetric around an internal axis. Consequently, their orientations are described by unit vectors $\hat{\mathbf{u}}_i$ with $i \in \{1, \dots, N\}$ along their internal symmetry axes. Most of the statistical quantities can suitably be generalized towards orientational degrees of freedom by including also the orientational configuration space on top of the translational configurational space.

3.1.3.1 *Statics.* For orientable particles, the one-particle density is now defined via

$$\rho(\mathbf{r}, \hat{\mathbf{u}}) = \left\langle \sum_{i=1}^N \delta(\mathbf{r} - \mathbf{r}_i) \delta(\hat{\mathbf{u}} - \hat{\mathbf{u}}_i) \right\rangle \quad (78)$$

and contains also the probability distribution of the orientations as expressed by the dependence on the orientational unit vector $\hat{\mathbf{u}}$. Its full configurational mean is given by the mean particle number density

$$\rho_0 = \frac{1}{4\pi V} \int d\mathbf{r} \int d\hat{\mathbf{u}} \rho(\mathbf{r}, \hat{\mathbf{u}}) = \frac{N}{V}, \quad (79)$$

where the orientational integral denotes integration over the two-dimensional unit sphere S_2 . Now the external potential is $U_1(\mathbf{r}, \hat{\mathbf{u}})$ and couples also to the particle orientation. In general, also the pair-interaction potential $U_2(\mathbf{r}_1 - \mathbf{r}_2, \hat{\mathbf{u}}_1, \hat{\mathbf{u}}_2)$ has an orientational dependence. The corresponding equilibrium Helmholtz free-energy functional $\mathcal{F}[\rho(\mathbf{r}, \hat{\mathbf{u}})]$ can be split as usual into three contributions

$$\mathcal{F}[\rho(\mathbf{r}, \hat{\mathbf{u}})] = \mathcal{F}_{\text{id}}[\rho(\mathbf{r}, \hat{\mathbf{u}})] + \mathcal{F}_{\text{exc}}[\rho(\mathbf{r}, \hat{\mathbf{u}})] + \mathcal{F}_{\text{ext}}[\rho(\mathbf{r}, \hat{\mathbf{u}})] \quad (80)$$

namely the ideal rotator-gas free-energy contribution

$$\mathcal{F}_{\text{id}}[\rho(\mathbf{r}, \hat{\mathbf{u}})] = k_B T \int d\mathbf{r} \int d\hat{\mathbf{u}} \rho(\mathbf{r}, \hat{\mathbf{u}}) (\ln(\Lambda^3 \rho(\mathbf{r}, \hat{\mathbf{u}})) - 1), \quad (81)$$

the non-trivial excess free-energy functional $\mathcal{F}_{\text{exc}}[\rho(\mathbf{r}, \hat{\mathbf{u}})]$, and the external free-energy contribution (Section 2.1)

$$\mathcal{F}_{\text{ext}}[\rho(\mathbf{r}, \hat{\mathbf{u}})] = \int d\mathbf{r} \int d\hat{\mathbf{u}} \rho(\mathbf{r}, \hat{\mathbf{u}}) U_1(\mathbf{r}, \hat{\mathbf{u}}). \quad (82)$$

Analogously to Equation (8), a functional Taylor expansion

$$\mathcal{F}_{\text{exc}}[\rho(\mathbf{r}, \hat{\mathbf{u}})] = \mathcal{F}_{\text{exc}}^{(0)}(\rho_{\text{ref}}) + k_B T \sum_{n=1}^{\infty} \frac{1}{n!} \mathcal{F}_{\text{exc}}^{(n)}[\rho(\mathbf{r}, \hat{\mathbf{u}})] \quad (83)$$

with the n th-order contributions

$$\mathcal{F}_{\text{exc}}^{(n)}[\rho(\mathbf{r}, \hat{\mathbf{u}})] = - \int d\mathbf{r}_1 \cdots \int d\mathbf{r}_n \int d\hat{\mathbf{u}}_1 \cdots \int d\hat{\mathbf{u}}_n c^{(n)}(\mathbf{r}^n, \hat{\mathbf{u}}^n) \prod_{i=1}^n \Delta \rho(\mathbf{r}_i, \hat{\mathbf{u}}_i), \quad (84)$$

the n -particle direct correlation function $c^{(n)}(\mathbf{r}^n, \hat{\mathbf{u}}^n)$, and the abbreviations

$$\mathbf{r}^n = (\mathbf{r}_1, \dots, \mathbf{r}_n), \quad \hat{\mathbf{u}}^n = (\hat{\mathbf{u}}_1, \dots, \hat{\mathbf{u}}_n) \quad (85)$$

are used. Again, the constant zeroth-order contribution of the functional Taylor expansion (83) is irrelevant and the first-order contribution vanishes. In the Ramakrishnan–Yussouff approximation, the functional Taylor expansion is truncated at second order.

In order to derive PFC-type models for liquid crystals, one can follow the same strategy as for spherical systems: first, the full density field $\rho(\mathbf{r}, \hat{\mathbf{u}})$ is parametrized by small and slowly varying space-dependent multi-component order-parameter fields. An insertion into the density functional together with a perturbative and gradient expansion yields a local PFC-type free energy. Then several coupling terms of the order-parameter components arise, whose prefactors are given by moments of the generalized direct fluid correlation functions. Still, the gradient expansion is more tedious, since the orientational space has a more complicated topology. For stability reasons, one has to assume that the coefficients of the highest-order terms in the gradients and order-parameter fields in the PFC model are positive in the full free-energy functional. If this appears not to be the case for a certain system, it is necessary to take further terms of the respective order-parameter field up to the first stabilizing order into account.

3.1.3.2 Two spatial dimensions. We now consider first the case of 2D both for the translational and orientational degrees of freedom. Here, the topology of orientations is simpler than in 3D. Obviously, all previous expressions can be changed towards two dimensions by replacing the volume V by an area A , by changing the unit sphere S_2 into the unit circle S_1 , and by replacing Λ^3 by Λ^2 in Equation (81). The orientational vector $\hat{\mathbf{u}}(\varphi) = (\cos(\varphi), \sin(\varphi))$ can be parametrized by a single polar angle $\varphi \in [0, 2\pi)$.

Derivation of the PFC free-energy functional: First we chose as order-parameter fields the *reduced translational density*, the *polarization*, and the *nematic tensor* field. The reduced translational density is defined via

$$\psi(\mathbf{r}) = \frac{1}{2\pi\rho_{\text{ref}}} \int d\hat{\mathbf{u}} (\rho(\mathbf{r}, \hat{\mathbf{u}}) - \rho_{\text{ref}}), \quad (86)$$

while the polarization is

$$\mathbf{P}(\mathbf{r}) = \frac{1}{\pi\rho_{\text{ref}}} \int d\hat{\mathbf{u}} \rho(\mathbf{r}, \hat{\mathbf{u}}) \hat{\mathbf{u}} \quad (87)$$

and describes the local averaged dipolar orientation of the particles. Finally, the symmetric and traceless nematic tensor with the components

$$Q_{ij}(\mathbf{r}) = \frac{2}{\pi\rho_{\text{ref}}} \int d\hat{\mathbf{u}} \rho(\mathbf{r}, \hat{\mathbf{u}}) \left(u_i u_j - \frac{1}{2} \delta_{ij} \right) \quad (88)$$

describes quadrupolar ordering of the particles. Equivalently, one could decompose the polarization $\mathbf{P}(\mathbf{r}) = P(\mathbf{r})\hat{\mathbf{p}}(\mathbf{r})$ into its modulus $P(\mathbf{r})$ and the local normalized dipolar orientation $\hat{\mathbf{p}}(\mathbf{r})$ and use the two order parameters $P(\mathbf{r})$ and $\hat{\mathbf{p}}(\mathbf{r})$ instead of $\mathbf{P}(\mathbf{r})$. Similarly, the nematic tensor can be expressed by [157,158]

$$Q_{ij}(\mathbf{r}) = S(\mathbf{r})(n_i(\mathbf{r})n_j(\mathbf{r}) - \frac{1}{2}\delta_{ij}) \quad (89)$$

through the *nematic order parameter* $S(\mathbf{r})$, which measures the local degree of quadrupolar orientational order [159], and the *nematic director* $\hat{\mathbf{n}}(\mathbf{r}) = (n_1(\mathbf{r}), n_2(\mathbf{r}))$. Note that $\hat{\mathbf{n}}(\mathbf{r})$ and $\hat{\mathbf{p}}(\mathbf{r})$ do not necessarily coincide.

One may expand the total density in terms of its orientational anisotropy as

$$\rho(\mathbf{r}, \hat{\mathbf{u}}) = \rho_{\text{ref}}(1 + \psi(\mathbf{r}) + P_i(\mathbf{r})u_i + u_i Q_{ij}(\mathbf{r})u_j). \quad (90)$$

Inserting the parametrization (90) into Equation (81), performing a Taylor expansion of the integrand up to the fourth order in the order-parameter fields, which guarantees stability of the solutions, and carrying out the angular integration yields to the approximation

$$\mathcal{F}_{\text{id}}[\psi, P_i, Q_{ij}] = F_{\text{id}} + \pi \rho_{\text{ref}} k_B T \int d\mathbf{r} f_{\text{id}}(\mathbf{r}) \quad (91)$$

with the local scaled ideal rotator-gas free-energy density

$$\begin{aligned} f_{\text{id}} = & \frac{\psi}{4} (8 - 2P_i^2 + 2P_i Q_{ij} P_j - Q_{ij}^2) + \frac{\psi^2}{4} (4 + 2P_i^2 + Q_{ij}^2) - \frac{\psi^3}{3} + \frac{\psi^4}{6} \\ & + \frac{P_i^2}{8} (4 + Q_{kl}^2) - \frac{P_i Q_{ij} P_j}{4} + \frac{P_i^2 P_j^2}{16} + \frac{Q_{ij}^2}{4} + \frac{Q_{ij}^2 Q_{kl}^2}{64}, \end{aligned} \quad (92)$$

where $F_{\text{id}} = 2\pi \rho_{\text{ref}} k_B T A (\ln(\Lambda^2 \rho_{\text{ref}}) - 1)$ is an irrelevant constant.

If the functional Taylor expansion (83) for the excess free energy is truncated at the fourth order, an insertion of the parametrization (90) into the functional (84) and a gradient expansion yield [160]

$$\mathcal{F}_{\text{exc}}^{(n)}[\psi, P_i, Q_{ij}] = - \int d\mathbf{r} f_{\text{exc}}^{(n)}(\mathbf{r}) \quad (93)$$

with

$$\begin{aligned} f_{\text{exc}}^{(2)} = & A_1 \psi^2 + A_2 (\partial_i \psi)^2 + A_3 (\partial_k^2 \psi)^2 + B_1 (\partial_i \psi) P_i + B_2 P_i (\partial_j Q_{ij}) + B_3 (\partial_i \psi) (\partial_j Q_{ij}) \\ & + C_1 P_i^2 + C_2 P_i (\partial_k^2 P_i) + C_3 (\partial_i P_i)^2 + D_1 Q_{ij}^2 + D_2 (\partial_j Q_{ij})^2, \end{aligned} \quad (94)$$

$$\begin{aligned} f_{\text{exc}}^{(3)} = & E_1 \psi^3 + E_2 \psi P_i^2 + E_3 \psi Q_{ij}^2 + E_4 P_i Q_{ij} P_j + F_1 \psi^2 (\partial_i P_i) + F_2 \psi P_i (\partial_j Q_{ij}) \\ & + F_3 (\partial_i \psi) Q_{ij} P_j + F_4 P_i^2 (\partial_j P_j) + F_5 (\partial_i P_i) Q_{kl}^2 + F_6 P_i Q_{ki} (\partial_j Q_{kj}), \end{aligned} \quad (95)$$

$$\begin{aligned} f_{\text{exc}}^{(4)} = & G_1 \psi^4 + G_2 \psi^2 P_i^2 + G_3 \psi^2 Q_{ij}^2 + G_4 \psi P_i Q_{ij} P_j + G_5 P_i^2 Q_{kl}^2 + G_6 P_i^2 P_j^2 \\ & + G_7 Q_{ij}^2 Q_{kl}^2. \end{aligned} \quad (96)$$

Obviously, this creates a much more sophisticated series of coupling terms between gradients of the different order-parameter fields. They are all allowed by symmetry. There are altogether 28 coupling coefficients $A_i, B_i, C_i, D_i, E_i, F_i, G_i$, which can in principle all be expressed as moments over the microscopic fluid direct correlation functions. These explicit expressions are summarized in Appendix A.1.

The general result for the two-dimensional PFC free energy constituted by Equations (94)–(96) contains several special cases, known from the literature, which we now discuss in more detail.

These special cases follow from the full free-energy functional either by choosing some of the order-parameter fields as zero or as a constant different from zero and by taking into account the contributions of the functional Taylor expansion (83) only up to a certain order $n_{\text{max}} \in \{2, 3, 4\}$. Table 2 gives an overview about the most relevant special cases.

The most simple special cases are obtained for either a constant translational density ψ , polarization P_i , or nematic tensor Q_{ij} with an arbitrary choice for n_{max} , when all remaining order-parameter fields are assumed to be zero. These special cases are known to be Landau expansions

Table 2. Relevant special cases that are contained in the polar PFC model for 2D. n_{\max} is the order of the functional Taylor expansion (83). If n_{\max} is not specified, it can be arbitrary (arb.).

ψ	P_i	Q_{ij}	n_{\max}	Associated model
0	0	Const.	Arb.	Landau expansion in Q_{ij}
0	0	$Q_{ij}(\mathbf{r})$	2	Landau-de Gennes free energy for uniaxial nematics [158]
0	0	$Q_{ij}(\mathbf{r})$	Arb.	Gradient expansion in $Q_{ij}(\mathbf{r})$
0	Const.	0	Arb.	Landau expansion in P_i
0	$P_i(\mathbf{r})$	0	Arb.	Gradient expansion in $P_i(\mathbf{r})$
Const.	0	0	Arb.	Landau expansion in ψ
$\psi(\mathbf{r})$	0	0	2	PFC model of Elder <i>et al.</i> [26]
$\psi(\mathbf{r})$	0	0	Arb.	Gradient expansion in $\psi(\mathbf{r})$
Const.	$P_i(\mathbf{r})$	$Q_{ij}(\mathbf{r})$	4	Constant-density approximation
$\psi(\mathbf{r})$	0	$Q_{ij}(\mathbf{r})$	2	PFC model of Löwen [67]
$\psi(\mathbf{r})$	$P_i(\mathbf{r})$	$Q_{ij}(\mathbf{r})$	4	Full free-energy functional

in ψ , P_i , and Q_{ij} , respectively. If the only non-vanishing order-parameter field is not constant, but space-dependent, then the functional can be called a gradient expansion in this order-parameter field. If additionally $n_{\max} = 2$ is chosen, the gradient expansion in $\psi(\mathbf{r})$ becomes the original PFC model of Elder *et al.* [26] and the gradient expansion in $Q_{ij}(\mathbf{r})$ reduces to the Landau-de Gennes free energy for inhomogeneous uniaxial nematics [158]. When only ψ is constant and the other order-parameter fields are space-dependent, we recover the case of an incompressible system. The liquid crystalline PFC model of Löwen [67] is obtained for $n_{\max} = 2$, if the translational density and the nematic tensor are space-dependent, while the polarization vanishes, and if the nematic tensor is parametrized according to Equation (89). In the polar PFC model for 2D, one can also consider the case of a space-dependent translational density $\psi(\mathbf{r})$, a space-dependent polarization $P_i(\mathbf{r})$, and a vanishing nematic tensor, that corresponds to a ferroelectric phase without orientational order, but such a phase was never observed in experiments up to the present day. Therefore, this case is not included in Table 2.

Equilibrium bulk phase diagram: While there are two independent parameters for the original PFC model (Equation (1) and Figure 9), the number of coupling parameters explodes for the general

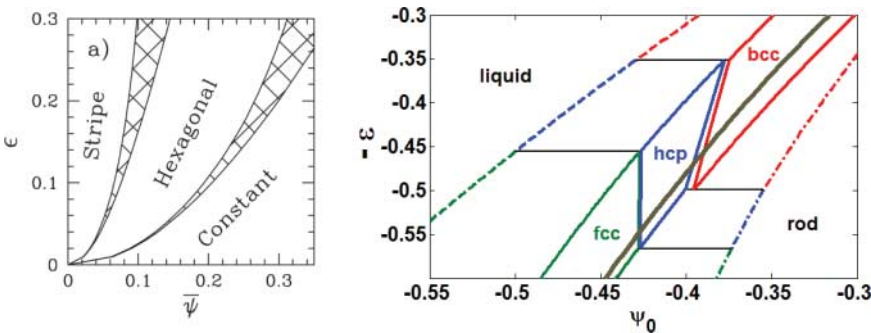


Figure 9. (a) Single-mode approximation to the phase diagram of the 1M-PFC model in 2D with $\epsilon \equiv \beta$ and the average reduced particle density $\bar{\psi}$. (Reproduced with permission from Elder *et al.* [12] © 2002 by the American Physical Society.) (b) Section of the 3D phase diagram of the 1M-PFC model evaluated by the Euler–Lagrange method described in reference [28] with $\epsilon \equiv \epsilon$ and the average reduced particle density ψ_0 . Note the stability domains of the bcc, hcp, and fcc phases. The homogeneous liquid is unstable right of the heavy grey line emerging from linear stability analysis [28]. (Reproduced from Tóth *et al.* [28] © 2010 by Institute of Physics Publishing.)

liquid crystalline PFC model as proposed in Equations (94)–(96) to 27 coupling coefficients. One of them can be incorporated into a length scale such that 26 coefficients remain. Therefore, a numerical exploration of the equilibrium phase diagram requires a much higher effort. Maybe not too surprising, such calculations are sparse and it was only until recently that the phase diagram was calculated for the apolar PFC model [67], where $\mathbf{P}(\mathbf{r}) = \mathbf{0}$, which contains only five independent parameters [69]. We summarize and outline the basic findings of reference [69] in Section 3.2.2.

3.1.3.3 *Three spatial dimensions.* We now discuss the three-dimensional ($d = 3$) PFC model for liquid crystals. In spherical coordinates, the three-dimensional orientation vector is

$$\hat{\mathbf{u}}(\theta, \phi) = (\sin(\theta) \cos(\phi), \sin(\theta) \sin(\phi), \cos(\theta)) \quad (97)$$

with the polar angle $\theta \in [0, \pi]$ and the azimuthal angle $\phi \in [0, 2\pi]$. We consider here only the apolar case, where the polarization vanishes: $\mathbf{P}(\mathbf{r}) = \mathbf{0}$. There exists indeed a zoo of realizations of apolar particles both in the molecular and in the colloidal regime. For suitable interactions, see references [161–169].

Following similar ideas as outlined in Section 3.1.3.2 for two dimensions, we define as the corresponding order parameters the reduced translational density

$$\psi(\mathbf{r}) = \frac{1}{4\pi\rho_{\text{ref}}} \int d\hat{\mathbf{u}} (\rho(\mathbf{r}, \hat{\mathbf{u}}) - \rho_{\text{ref}}) \quad (98)$$

and the 3×3 -dimensional symmetric and traceless nematic tensor

$$Q_{ij}(\mathbf{r}) = \frac{15}{8\pi\rho_{\text{ref}}} \int d\hat{\mathbf{u}} \rho(\mathbf{r}, \hat{\mathbf{u}}) \left(u_i u_j - \frac{1}{3} \delta_{ij} \right). \quad (99)$$

Again, the nematic tensor can be expressed by the nematic order-parameter field $S(\mathbf{r})$ and the nematic director $\hat{\mathbf{n}}(\mathbf{r}) = (n_1(\mathbf{r}), n_2(\mathbf{r}), n_3(\mathbf{r}))$, that is here and is the only unit vector that denotes a preferred direction in the liquid crystalline system. In the three-dimensional case, the decomposition of the nematic tensor is given by [157,158]

$$Q_{ij}(\mathbf{r}) = S(\mathbf{r}) \left(\frac{3}{2} n_i(\mathbf{r}) n_j(\mathbf{r}) - \frac{1}{2} \delta_{ij} \right). \quad (100)$$

Note that the nematic order-parameter field $S(\mathbf{r})$ is the biggest eigenvalue of the nematic tensor $Q_{ij}(\mathbf{r})$ and the nematic director $\hat{\mathbf{n}}(\mathbf{r})$ is the corresponding eigenvector. Accordingly, with the order-parameter fields $\psi(\mathbf{r})$ and $Q_{ij}(\mathbf{r})$, the one-particle density is approximated by

$$\rho(\mathbf{r}, \hat{\mathbf{u}}) = \rho_{\text{ref}} \left(1 + \psi(\mathbf{r}) + u_i Q_{ij}(\mathbf{r}) u_j \right). \quad (101)$$

As before, the Helmholtz free-energy functional has to be approximated by a Taylor expansion around the homogeneous reference system and by a gradient expansion [68]. The ideal rotator-gas free-energy functional is approximated by

$$\mathcal{F}_{\text{id}}[\psi, Q_{ij}] = F_{\text{id}} + \pi\rho_{\text{ref}} k_{\text{B}} T \int d\mathbf{r} f_{\text{id}}(\mathbf{r}) \quad (102)$$

with the local scaled ideal rotator-gas free-energy density

$$\begin{aligned} f_{\text{id}} = & 4\psi \left(1 - \frac{\text{tr}(\mathbf{Q}^2)}{15} + \frac{8\text{tr}(\mathbf{Q}^3)}{315} \right) + 2\psi^2 \left(1 + \frac{2\text{tr}(\mathbf{Q}^2)}{15} \right) - \frac{2\psi^3}{3} + \frac{\psi^4}{3} \\ & + \frac{4\text{tr}(\mathbf{Q}^2)}{15} - \frac{16\text{tr}(\mathbf{Q}^3)}{315} + \frac{8\text{tr}(\mathbf{Q}^4)}{315}. \end{aligned} \quad (103)$$

Here, $\text{tr}(\cdot)$ denotes the trace operator and $F_{\text{id}} = 4\pi\rho_{\text{ref}} V k_{\text{B}} T (\ln(\Lambda^3 \rho_{\text{ref}}) - 1)$ an irrelevant constant. For the excess free-energy functional, the Ramakrishnan–Yussouff approximation (11) is

used together with Equation (101) involving the direct correlation function $c^{(2)}(\mathbf{r}_1 - \mathbf{r}_2, \hat{\mathbf{u}}_1, \hat{\mathbf{u}}_2)$. Respecting all symmetries, one finally obtains the following approximation for the excess free-energy functional

$$\mathcal{F}_{\text{exc}}^{(2)}[\psi, Q_{ij}] = - \int d\mathbf{r} f_{\text{exc}}^{(2)}(\mathbf{r}) \quad (104)$$

with the local scaled excess free-energy density

$$f_{\text{exc}}^{(2)} = A_1 \psi^2 + A_2 (\partial_i \psi)^2 + A_3 (\partial_k^2 \psi)^2 + B_1 Q_{ij}^2 + B_2 (\partial_i \psi) (\partial_j Q_{ij}) + \tilde{K}_1 (\partial_j Q_{ij})^2 + \tilde{K}_2 Q_{ij} (\partial_k^2 Q_{ij}). \quad (105)$$

The seven coupling coefficients $A_1, A_2, A_3, B_1, B_2, \tilde{K}_1, \tilde{K}_2$ can be expressed as generalized moments of the microscopic correlation function $c^{(2)}(\mathbf{r}_1 - \mathbf{r}_2, \hat{\mathbf{u}}_1, \hat{\mathbf{u}}_2)$. The full expressions are summarized in Appendix A.2. We remark that \tilde{K}_1 and \tilde{K}_2 correspond to the traditional Frank constants appearing in Frank's elastic energy [158,170].

Special cases of the free-energy density are summarized in Table 3. As for the PFC model for 2D, one obtains a Landau expansion in the nematic tensor Q_{ij} , if the translational density $\psi(\mathbf{r})$ is zero and the nematic tensor is constant so that all gradients vanish. Analogously, one obtains a Landau expansion in ψ , if $Q_{ij}(\mathbf{r})$ is zero and the translational density is constant. When only ψ is zero and $Q_{ij}(\mathbf{r})$ is space-dependent, the Landau-de Gennes free energy for inhomogeneous uniaxial nematics [158] is recovered again. Clearly, the original PFC model of Elder *et al.* [26] for isotropic particles in 3D can be obtained from the full free-energy functional by choosing $Q_{ij}(\mathbf{r}) = 0$. The case of a constant ψ and a space-dependent $Q_{ij}(\mathbf{r})$ corresponds to an incompressible system. Finally, we note that the full functional was recently numerically evaluated for several situations by Yabunaka and Araki in reference [171].

3.1.3.4 Dynamics. DDFT can now be used to derive the dynamics of the PFC models for liquid crystals. DDFT is well justified for Brownian anisotropic particles (as, for example, colloidal rods or platelets). The basic derivation is similar to that performed for spherical particles in Section 2.3.2, but in practice it is much more tedious. The basic derivation is performed in three steps. At first, the order-parameter fields, that have been chosen for the statics, are assumed to be time-dependent and the time-dependent one-particle density $\rho(\mathbf{r}, \hat{\mathbf{u}}, t)$ is approximated in terms of these time-dependent order-parameter fields. Secondly, the chain rule for functional differentiation is used to express the functional derivative $\delta\mathcal{F}/\delta\rho$ of the Helmholtz free-energy functional \mathcal{F} in terms of the functional derivatives of the free-energy functional with respect to the chosen order-parameter fields. Finally, the time-dependent parametrization for the one-particle density and the time-dependent expression for the functional derivative $\delta\mathcal{F}/\delta\rho$ are inserted into the DDFT equation and a set of in general coupled dynamic equations for the single-order parameter fields is obtained by an orthogonal projection of the DDFT equation with respect to the orientation $\hat{\mathbf{u}}$.

Table 3. Relevant special cases that are contained in the apolar PFC model for 3D.

ψ	Q_{ij}	Associated model
0	Const.	Landau expansion in Q_{ij}
0	$Q_{ij}(\mathbf{r})$	Landau-de Gennes free energy for uniaxial nematics [158]
Const.	0	Landau expansion in ψ
$\psi(\mathbf{r})$	0	PFC model of Elder <i>et al.</i> [26]
Const.	$Q_{ij}(\mathbf{r})$	Constant-density approximation
$\psi(\mathbf{r})$	$Q_{ij}(\mathbf{r})$	Full free-energy functional

We first consider the case of 2D ($d = 2$). The time-dependent noise-averaged one-particle number density is now

$$\rho(\mathbf{r}, \hat{\mathbf{u}}, t) = \left\langle \sum_{i=1}^N \delta(\mathbf{r} - \mathbf{r}_i(t)) \delta(\hat{\mathbf{u}} - \hat{\mathbf{u}}_i(t)) \right\rangle \quad (106)$$

and its order-parameter parametrization is

$$\rho(\mathbf{r}, \hat{\mathbf{u}}, t) = \rho_{\text{ref}}(1 + \psi(\mathbf{r}, t) + P_i(\mathbf{r}, t)u_i + u_i Q_{ij}(\mathbf{r}, t)u_j). \quad (107)$$

The DDFT equation for orientational degrees of freedom in 2D (without a hydrodynamic translational-rotational coupling) reads [108]

$$\dot{\rho}(\mathbf{r}, \hat{\mathbf{u}}, t) = \nabla_{\mathbf{r}} \cdot \left(\frac{D_{\text{T}}(\hat{\mathbf{u}})}{k_{\text{B}}T} \rho(\mathbf{r}, \hat{\mathbf{u}}, t) \nabla_{\mathbf{r}} \frac{\delta \mathcal{F}(T, [\rho])}{\delta \rho(\mathbf{r}, \hat{\mathbf{u}}, t)} \right) + \frac{D_{\text{R}}}{k_{\text{B}}T} \partial_{\varphi} \left(\rho(\mathbf{r}, \hat{\mathbf{u}}, t) \partial_{\varphi} \frac{\delta \mathcal{F}(T, [\rho])}{\delta \rho(\mathbf{r}, \hat{\mathbf{u}}, t)} \right) \quad (108)$$

with the translational short-time diffusion tensor

$$D_{\text{T}}(\hat{\mathbf{u}}) = D_{\parallel} \hat{\mathbf{u}} \otimes \hat{\mathbf{u}} + D_{\perp} (\mathbf{1} - \hat{\mathbf{u}} \otimes \hat{\mathbf{u}}). \quad (109)$$

Here, D_{\parallel} and D_{\perp} are the translational diffusion coefficients for the translation parallel and perpendicular to the orientation $\hat{\mathbf{u}} = (\cos(\phi), \sin(\phi))$, respectively, and the symbol $\mathbf{1}$ denotes the 2×2 -dimensional unit matrix. The two terms on the right-hand-side of this DDFT equation correspond to the pure translation and pure rotation, respectively.

The CMA is now

$$\dot{\rho}(\mathbf{r}, \hat{\mathbf{u}}, t) = \rho_{\text{ref}} \nabla_{\mathbf{r}} \cdot \left(\frac{D_{\text{T}}(\hat{\mathbf{u}})}{k_{\text{B}}T} \nabla_{\mathbf{r}} \frac{\delta \mathcal{F}(T, [\rho])}{\delta \rho(\mathbf{r}, \hat{\mathbf{u}}, t)} \right) + \rho_{\text{ref}} \frac{D_{\text{R}}}{k_{\text{B}}T} \partial_{\varphi}^2 \frac{\delta \mathcal{F}(T, [\rho])}{\delta \rho(\mathbf{r}, \hat{\mathbf{u}}, t)}. \quad (110)$$

Within the CMA, this yields for the dynamics of the order-parameter fields

$$\dot{\psi} + \partial_i J_i^{\psi} = 0, \quad \dot{P}_i + \Phi_i^P = 0, \quad \dot{Q}_{ij} + \Phi_{ij}^Q = 0 \quad (111)$$

with the currents and quasi-currents

$$J_i^{\psi} = -2\alpha_1 \partial_i \frac{\delta \mathcal{F}}{\delta \psi} - 2\alpha_3 \partial_j \frac{\delta \mathcal{F}}{\delta Q_{ij}}, \quad (112)$$

$$\Phi_i^P = -2\alpha_2 \partial_k^2 \frac{\delta \mathcal{F}}{\delta P_i} - 4\alpha_3 \partial_i \partial_j \frac{\delta \mathcal{F}}{\delta P_j} + 2\alpha_4 \frac{\delta \mathcal{F}}{\delta P_i}, \quad (113)$$

$$\Phi_{ij}^Q = -4\alpha_1 \partial_k^2 \frac{\delta \mathcal{F}}{\delta Q_{ij}} - 2\alpha_3 \left(2\partial_i \partial_j \frac{\delta \mathcal{F}}{\delta \psi} - \delta_{ij} \partial_k^2 \frac{\delta \mathcal{F}}{\delta \psi} \right) + 8\alpha_4 \frac{\delta \mathcal{F}}{\delta Q_{ij}}. \quad (114)$$

The coefficients α_i in Equations (112)–(114) are defined as

$$\alpha_1 = \frac{D_{\parallel} + D_{\perp}}{8\lambda}, \quad \alpha_2 = \frac{D_{\parallel} + 3D_{\perp}}{8\lambda}, \quad \alpha_3 = \frac{D_{\parallel} - D_{\perp}}{8\lambda}, \quad \alpha_4 = \frac{D_{\text{R}}}{2\lambda}. \quad (115)$$

Note that $D_{\parallel} \geq D_{\perp}$ holds for all types of uniaxial particles, if the vector $\hat{\mathbf{u}}$ for the orientation of the axis of symmetry is chosen properly.

Finally, we remark that in three dimensions ($d = 3$) the dynamics is much more involved but can in principle be derived along similar lines from DDFT [112]. Recently, the CMA dynamics was considered in reference [171]. A main result of this reference is shown in Section 5.2.

3.1.4. Numerical methods

3.1.4.1 *The equation of motion.* The commonly used combination of explicit time-stepping with a finite-difference (FD) scheme has been routinely applied for solving the EOM of the PFC models [172]. However, owing to the high-order differential operators appearing in the EOM of the PFC models (up to 12th order), explicit time-stepping suffers from severe constraints. Energy stable large time-step implicit FD methods have been developed for the PFC [173] and MPFC [174] equations, which lead to large sets of sparse algebraic equations. The resultant algebraic equations can be solved using nonlinear multigrid methods [175]. As an elegant alternative, pseudo-spectral methods can be used, which combine unconditionally stable time marching with algebraic equations of the diagonal form [176]. Furthermore, the pseudo-spectral methods offer exponential convergence with the spatial resolution as opposed to the polynomial convergence rate of the FD schemes. This means that with smaller spatial resolution, one obtains results comparable to those obtained with high spatial resolution in the real space methods. Using operator splitting techniques, the domain of the spectral methods has been extended to a wide range of problems, including PDEs with variable coefficients [177]. A detailed study on the application of this method to PFC models shows that the respective schemes can be parallelized easily and efficiently [177], yielding up to 10^5 times faster computations, when compared to FD schemes. Adaptive time stepping [176] may further accelerate such computations. Other numerical methods (e.g. stable semi-implicit finite element discretization combined with adaptive time stepping [178]) have also been used for PFC models, however, further investigations are needed to assess their numerical accuracy.

3.1.4.2 *The Euler–Lagrange equation and other saddle point finding methods.* In recent works [28,35], the ELE has been solved using a semi-spectral successive approximation scheme combined with the operator-splitting technique [179]. A different approach termed the fixed length simplified string method has been proposed to find the minimum energy path and the nucleation barrier in reference [32].

3.1.5. Coarse-graining the PFC models

Soon after the appearance of the 1M-PFC model, attempts have been made to use this atomistic approach as a basis for deriving phase-field-type coarse-grained models, using the amplitude equation method. This extension to the 1M-PFC formalism, when combined with the adaptive grid, has the potential to enable simulations of mesoscopic phenomena ($\mu\text{m} \rightarrow \text{mm}$) that are resolved down to the atomic scale, still incorporating all the respective physics.

3.1.5.1 *Amplitude equations based on renormalization group theory.* Goldenfeld *et al.* [141] have developed a computationally efficient approach to polycrystalline solidification, based on the 1M-PFC model. The nanoscale particle density distribution is reconstructed from its slowly varying amplitude and phase, obtained by solving the rotationally covariant equations of motion derived from renormalization group theory. They have shown in two dimensions that the microscopic density distributions from their amplitude and phase equations show a very close match to the 1M-PFC result. In later works, Athreya and co-workers [19,20] have combined this approach with adaptive mesh algorithms, leading to a substantial acceleration of the numerical code. (Possible ways of using the renormalization group methods have been discussed in references [20,180].) Despite the impressive computational gains achieved when combining renormalization group theory with adaptive mesh refinement, several technical issues require further attention, as pointed out in reference [20]. Amongst them are the following two open issues [20]:

- The first one concerns the boundary conditions used in describing polycrystalline matter under externally applied loads or displacements such as shear, uniaxial or biaxial loading

states [59,60]. For the scalar order-parameter field, the 1M-PFC model employs, appropriate boundary conditions have been worked out [61]. In the renormalization-group-theory-based amplitude expansion method, the scalar order parameter of the 1M-PFC model is replaced by a complex one. This means that for polycrystals under externally applied load, a meaningful translation of the respective boundary conditions to amplitudes *and* phases is required. This can, however, be mathematically demanding, since it requires the solution of systems of nonlinearly coupled equations at the boundaries [20].

- Another important issue, as pointed out in reference [20], follows from the fact that the renormalization-group-theory-based amplitude equations rely on the single-mode approximation. Accordingly, for situations that require higher modes (e.g. large distance from the critical point), the respective higher-mode amplitude equations still need to be developed systematically [20].

3.1.5.2 Phenomenological amplitude equations. Approximate treatments based on the amplitude expansion of the free energy of the 1M-PFC models (i.e. expressing \mathcal{F} in terms of the Fourier amplitude of the dominant density waves) have been developed. They have been used for various purposes, such as determining the anisotropy of liquid-solid interfacial free energies [41,144], the Asaro-Tiller-Grinfeld (ATG) morphological instability of a stressed crystal surface, polycrystalline growth from the melt, grain-boundary energies over a wide range of misorientation, and grain-boundary motion coupled to shear deformation [52,63]. Yeon *et al.* [181] have used an amplitude-equation approach to model the evolution of a two-phase system that has been validated by investigating the Gibbs-Thomson effect in 2D. Elder *et al.* [31] have proposed amplitude representations for the binary PFC model in the cases of triangular lattice (2D) and bcc and fcc (3D) structures. The respective equations of motion have been related to those of the original PF theory of binary freezing and elasticity, providing explicit connection between the PF and PFC approaches. The abilities of the phenomenological amplitude models have been demonstrated for eutectic solidification, solute migration at grain boundaries, and for the formation of quantum dots on nanomembranes [31].

3.2. Phase diagrams the PFC models realize

The different versions and extensions of the PFC model, reviewed in Section 3.1, lead to different phase diagrams, which in turn depend on the dimensionality of the system.

3.2.1. Phase diagram of single-component and binary systems

The phase diagrams of the 1M-PFC model [12] in 2D and 3D are shown in Figure 9. In 2D, a single crystalline phase (the triangular phase) appears that coexists with the liquid and a striped phase [12]. Remarkably, phase diagrams of comparable structure have been predicted for weakly charged colloids with competing interactions [182]. In 3D, as implied earlier by EOM studies [42], and confirmed by full thermodynamic optimization [143] and an equivalent method based on solving the ELE [28], stability domains exist for the homogeneous fluid, bcc, fcc, and hcp structures, besides the 3D version of the respective 2D structures: the rod and the lamellar structures. Interestingly, the rod and lamellar structures, and a phase diagram resembling to the 1M-PFC phase diagram appear in MD simulations for a Derjaguin-Landau-Verwey-Overbeek (DLVO) type potential [183] (Figure 10), characteristic to charged colloidal systems. The 1M-PFC model prefers the formation of the bcc phase near the critical point.

In contrast, the 2M-PFC model by Wu *et al.* [144], which has been designed to realize fcc crystallization, suppresses the bcc phase (Figure 11(a)). Remarkably, the 1M-PFC model can be

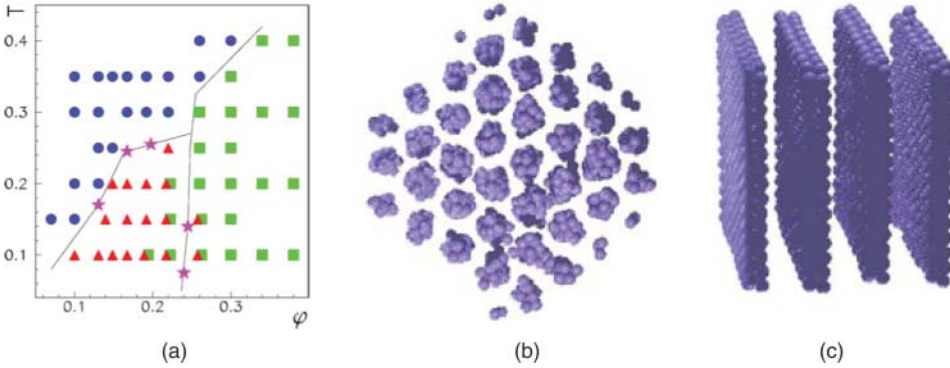


Figure 10. (a) Temperature-particle density phase diagram from MD simulations with a DLVO-type potential. Circles represent the disordered phase, triangles the columnar phase, and squares the lamellar phase. Stars stand for points, where the free energies of two phases cross. Solid lines are a guide for the eyes. Snapshots of the (b) triangular rod and (c) lamellar phases. (Reproduced with permission from de Candia *et al.* [183] © 2006 by the American Physical Society.)

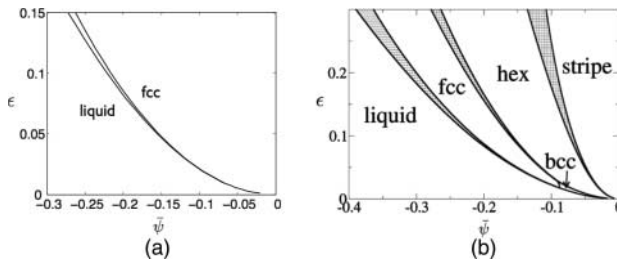


Figure 11. (a) Single-mode approximations to the phase diagram of the 2M-PFC model in 3D for $R_1 = 0$. (b) The same for $R_1 = 0.05$. Note the small bcc stability domain near the critical point. (Reproduced with permission from Wu *et al.* [144] © 2010 by the American Physical Society.)

obtained as a limiting case of the 2M-PFC approach. Interpolating between the full fcc ($R_1 = 0$) and the 1M-PFC limits in terms of the parameter R_1 leads to the appearance of a bcc stability domain in the neighborhood of the critical point (Figure 11(b)). (Here R_1 is the ratio of the Fourier amplitudes for the density waves having the second and first neighbour RLVs as wave vector.) Whether the appearance of the bcc stability domain is accompanied with that of an hcp stability domain, as seen in the 1M-PFC limit, requires further investigation [71].

The applicability of the EOF-PFC model has been demonstrated for Fe [142]. The free energy vs. particle density curves for the solid and liquid phases, which were used to determine the equilibrium conditions at the melting point, are shown in Figure 12. No phase diagram has been published for this model. It appears that much like the original 1M-PFC model, it prefers bcc freezing [71].

An attempt to control the preferred crystal structure relies on manipulating the two-particle direct correlation function so that its peaks prefer the desired structural correlations [146]. The type of phase diagram accessible for this method and the respective free-energy curves for coexistence between the bcc and fcc structures are displayed in Figure 13(a). Starting from the observation that the nonlinearities can stabilize the square lattice [184] so that it coexists with the triangular

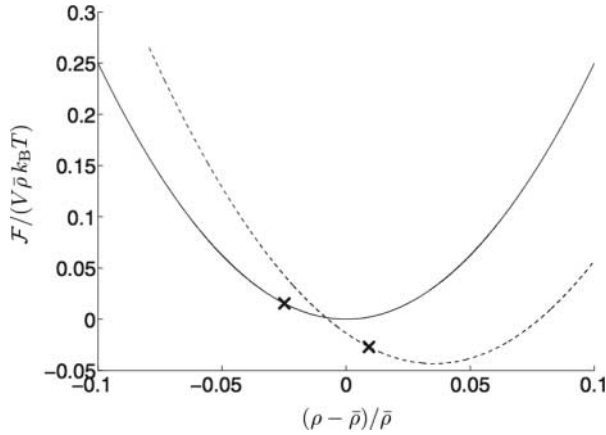


Figure 12. Free-energy density for the liquid (solid) and bcc (dashed) Fe as a function of reduced particle density in the EOF-PFC model. Crosses denote the equilibrium points obtained by the common tangent method. (Reproduced with permission from Jaatinen *et al.* [142] © 2009 by the American Physical Society.)

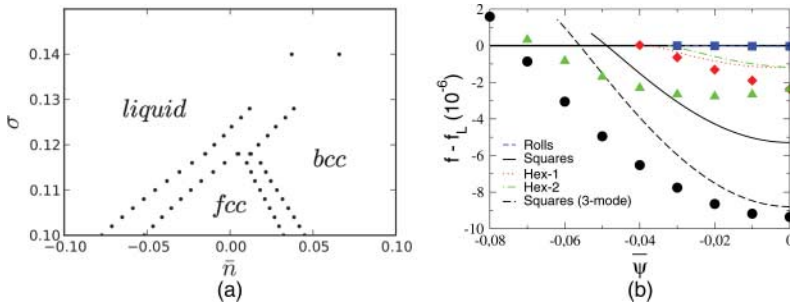


Figure 13. (a) Phase diagram in the effective temperature σ -mean density \bar{n} -plane for a system whose direct correlation function was manipulated so that peritectic coexistence between the fcc and bcc structures is realized. (Reproduced with permission from Greenwood *et al.* [146] © 2011 by the American Physical Society.) (b) Free-energy density f vs. average reduced particle density $\bar{\psi}$ when controlling the crystal structure via nonlinear resonance. f_L denotes the free-energy density of the liquid. The analytical solutions are plotted as lines, while the numerical simulation results for rolls, squares, hex-1, and hex-2 are plotted as squares, circles, diamonds, and triangles, respectively. (Reproduced with permission from Wu *et al.* [147] © 2010 by Institute of Physics Publishing.)

phase [185], Wu *et al.* [147] have proposed a method based on nonlinear resonance for constructing PFC models that prefer the desired crystal structure, as they indeed demonstrated for the square lattice in 2D: the relative free energies of possible competing structures are compared in Figure 13(b).

Elder *et al.* [26] have obtained eutectic phase diagrams within the binary generalization of the 1M-PFC model in 2D both numerically and by using the single-mode approximation. Comparable phase diagrams (Figure 14(a) and (b)) have been reported for triangular phases in 2D, and for the bcc and fcc phases in 3D, by the phenomenological amplitude equation method [31]. The 3D extension of the binary 1M-PFC model has been investigated by Tóth *et al.* [28]. The map of the thermodynamic driving force for solidification as a function of composition and density of the initial liquid is shown in Figure 14(c). 3D eutectic solidification to bcc phases of different lattice constants has indeed been observed in the domain of the largest driving force.

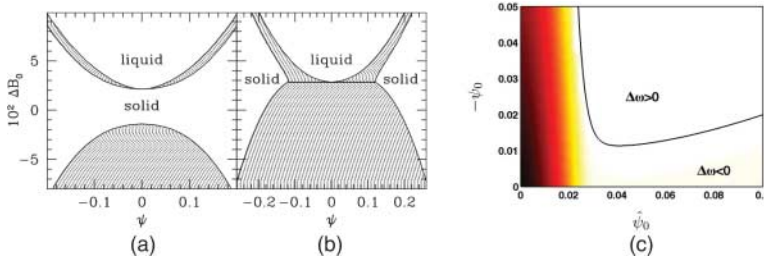


Figure 14. (a), (b) Reduced temperature ΔB_0 vs. reduced particle density difference ψ phase diagrams for the two-dimensional triangular system in the amplitude equation formalism. The filled regions correspond to regions of phase coexistence. (Reproduced with permission from Elder *et al.* [31] © 2010 by the American Physical Society.) (c) Colour map for the thermodynamic driving force of eutectic solidification ($\Delta\omega$ is the grand potential density difference relative to the liquid) for the binary 1M-PFC model in 3D [28], as a function of the chemical composition $\hat{\psi}_0$ and density ψ_0 . Note that solidification is expected in the region, where $\Delta\omega < 0$. (Reproduced from Tóth *et al.* [28] © 2010 by Institute of Physics Publishing.)

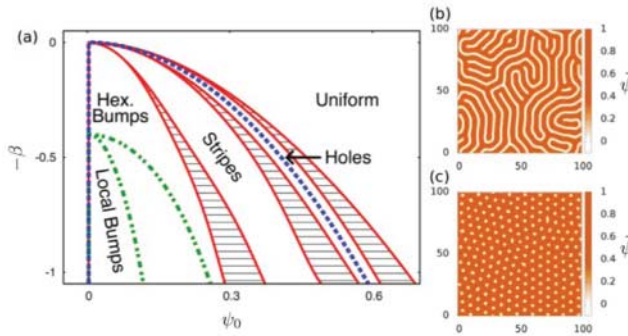


Figure 15. Phase diagram for the VPFC model in 2D [Equation (58)] (a) for $k_0 = 1$ [156]. The red solid lines denote coexistence curves, the green dash-dotted lines envelope the region, where localized and hexagonally ordered density peaks (bumps) coexist, whereas the blue dashed line indicates the linear stability limit of the spatially uniform phase. Snapshots of simulations for (b) stripes and (c) hexagonally ordered holes are also shown. These simulations have been performed for: $k_0 = 1$, $\beta = 0.9$, $h = 1500$, $M = 1$ (the mobility in the EOM) and (b) $\psi_0 = 0.4$ and (c) $\psi_0 = 0.53$. (Reproduced from Robbins *et al.* [156] © 2012 by the American Physical Society.)

An essential question is how to extend the PFC framework to accommodate the physical properties of real alloys of different crystalline structures. A two-phase binary extension of the EOF-PFC model based on the 1M-PFC and 2M-PFC concepts might be worth exploring.

The VPFC extension of the 1M-PFC model leads to a restructured phase diagram (Figure 15) [156], whose central region contains stability domains for the 2D hexagonal crystal and localized density peaks (“bumps”) that represent individual particles.

3.2.2. Phase diagram of two-dimensional liquid crystals

For liquid crystalline systems, there are much more candidates for possible bulk phases. Therefore the topology of the bulk phase diagram is getting more complex. Recently, bulk phase diagrams were computed by using the two-dimensional apolar PFC model of Löwen [67]. After

an appropriate scaling in energy and length, this model reads as

$$\mathcal{F}[\psi, Q_{ij}] = \int d\mathbf{r} \left(-\frac{\psi^3}{3} + \frac{\psi^4}{6} + (\psi - 1) \frac{\psi Q_{ij}^2}{4} + \frac{Q_{ij}^2 Q_{kl}^2}{64} + A_1 \psi^2 + A_2 \psi (\partial_k^2 + \partial_l^2) \psi \right. \\ \left. + B_3 (\partial_i \psi) (\partial_j Q_{ij}) + D_1 Q_{ij}^2 + D_2 (\partial_j Q_{ij})^2 \right). \tag{116}$$

Some trends of the phase diagram can directly be read of Equation (116). Since the parameter D_1 controls the contribution of the nematic tensor $Q_{ij}(\mathbf{r})$ and therefore also of the nematic order parameter $S(\mathbf{r})$, the nematic phase can be expected to be stable for large negative values of D_1 . In the opposite case, if D_1 is large enough and positive, the term $D_1 Q_{ij}^2(\mathbf{r}) + Q_{ij}^2(\mathbf{r}) Q_{kl}^2(\mathbf{r})/64$ dominates the free energy and only phases with $Q_{ij}(\mathbf{r}) \propto S(\mathbf{r}) = 0$ can be stable. Crystalline phases with a non-vanishing nematic order can therefore only appear in a region around $D_1 = 0$. From previous work it is known that the difference $A_1 - A_2/4$ has a big influence on the translational density field $\psi(\mathbf{r})$ [26,69]. If the parameter A_1 is large and positive, variations of the translational density field enlarge the free energy. Similarly, gradients of the translational density field enlarge the free energy for large and negative values of A_2 . Therefore, phases without any density modulations, that is, the isotropic and the nematic phase, are preferred for positive values of the difference $A_1 - A_2/4$, while all other phases with a periodic translational density field are preferred for negative values of this difference. Furthermore, there is a symmetry concerning the reversal of the sign of the parameter B_3 in the free-energy functional. From Equation (116) follows directly, that the free-energy functional is invariant under a simultaneous change of the signs of the parameter B_3 and the nematic order-parameter field $S(\mathbf{r})$. Due to this symmetry, $B_3 \geq 0$ can be assumed without loss of generality.

Depending on the coupling parameters, a wealth of different stable liquid crystalline phases was found (Figure 16). They include an *isotropic* phase, which has no translational and no orientational ordering ($\psi(\mathbf{r}) = 0$ and $S(\mathbf{r}) = 0$), a *nematic* phase with pure orientational ordering ($\psi(\mathbf{r}) = 0$ and $S(\mathbf{r}) > 0$), a *columnar* phase (or equivalently a *smectic A* phase), where the translational density and the orientation show a one-dimensional undulation, and various *plastic crystals*. In the columnar/smectic A phase the system has positional ordering in one direction, while it is isotropic perpendicular to this direction. The nematic order-parameter field $S(\mathbf{r})$ for this phase has a similar profile to the reduced translational density field $\psi(\mathbf{r})$ with maxima of these two fields at the same positions. Near the maxima of the translational density $\psi(\mathbf{r})$, the director field $\hat{\mathbf{n}}(\mathbf{r})$ is preferentially parallel to the gradient $\partial_i \psi(\mathbf{r})$, while it is perpendicular to $\partial_i \psi(\mathbf{r})$ around the minima of $\psi(\mathbf{r})$. A similar flipping of the orientational field from perpendicular to parallel to the stripe direction was identified as transverse intralayer order in the three-dimensional smectic A phase of hard spherocylinders [118].

Plastic crystals are two-dimensional modulations of the translational density and have no global (averaged) orientational direction. Interestingly, depending on the coupling-parameter combinations, three different types of plastic crystals are stable including two-dimensional triangular, square, and honeycomb lattices for the translational ordering. The orientational field of plastic crystals is schematically shown in Figure 17. It exhibits an interesting defect structure in the orientation. There are defects at the density peaks and in the interstitial places of the lattice. The defect structure has not yet been explored so far outside the PFC-world. It can be confirmed in microscopic computer simulations [186] or in real-space experiments [187–189].

In a two-dimensional slice of the coupling parameter space, the phase diagram is shown in Figure 18. Apart from the isotropic phase with $\psi(\mathbf{r}) = 0$ and $S(\mathbf{r}) = 0$, which appears for $A_1 > A_2/4$ and $D_1 > 0$, for negative and large D_1 a nematic phase is stable. A rich topology occurs

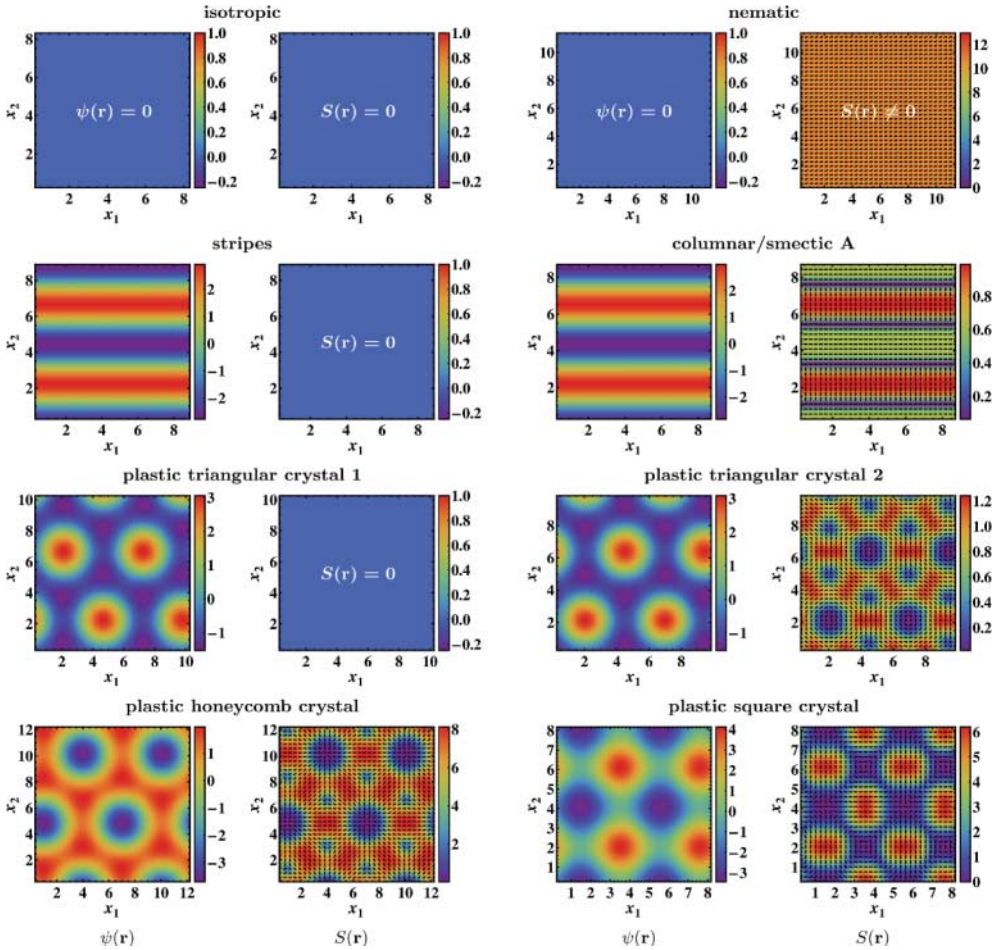


Figure 16. Stable liquid crystalline phases. The contour plots show the order-parameter fields $\psi(\mathbf{r})$ and $S(\mathbf{r})$ in the x_1 - x_2 -plane for the isotropic and nematic phases, the stripe phase and columnar/smectic A phase, two plastic triangular crystals with different orientational ordering, and a plastic honeycomb crystal as well as a plastic square crystal. The black lines in the plots of the second and fourth column represent the director field $\hat{\mathbf{n}}(\mathbf{r})$. In the plots with $S(\mathbf{r}) = 0$, the director field is not shown because it is not defined. The parameters are $A_2 = 14, D_2 = 8$, and $B_3 = 0$ for the stripe phase and the plastic triangular crystal 1 and $A_2 = 14, D_2 = 0.8$, and $B_3 = -4$ for all other phases. (Reproduced from Achim *et al.* [69] © 2011 by the American Physical Society.)

around $D_1 = 0$ including columnar phases and three different plastic crystals. However, one should bear in mind that the phase transitions shown in Figure 18 were assumed to be isochoric, that is, without any density jump. While this is in general a good approximation for liquid crystalline phase transitions, it is not true in general. Independent of the particular value of the parameter B_3 , the phase transition between the isotropic and the nematic phase is continuous, while all other phase transitions are discontinuous.

In conclusion, rich phase diagrams with novel liquid crystalline phases were found in the apolar PFC model. This gives confidence that in a further step interfaces between coexisting phases and the dynamics can be explored on the basis of the PFC approach. It would open the way of PFC models to enter into the rich world of liquid crystals.

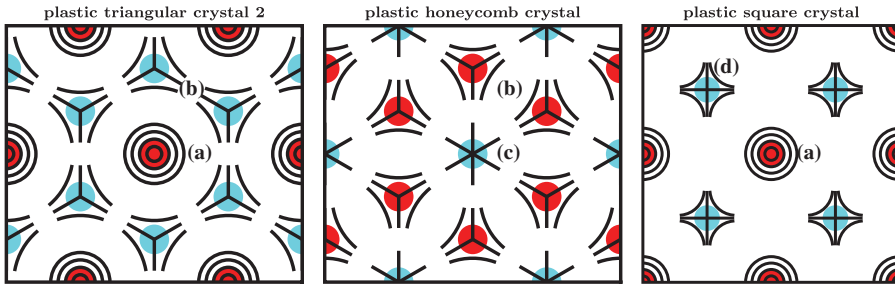


Figure 17. Topological defects in three different plastic liquid crystals in the x_1 - x_2 -plane (schematic). The defects coincide with the maxima (red discs) and minima (cyan discs) of the translational density field $\psi(\mathbf{r})$. The symbols in the plots represent the following defects: (a) vortices with the topological winding number $m = 1$, (b) disclinations with $m = -1/2$, (c) sources/sinks with $m = 1$, and (d) hyperbolic points with $m = -1$. (Reproduced from Achim *et al.* [69] © 2011 by the American Physical Society.)

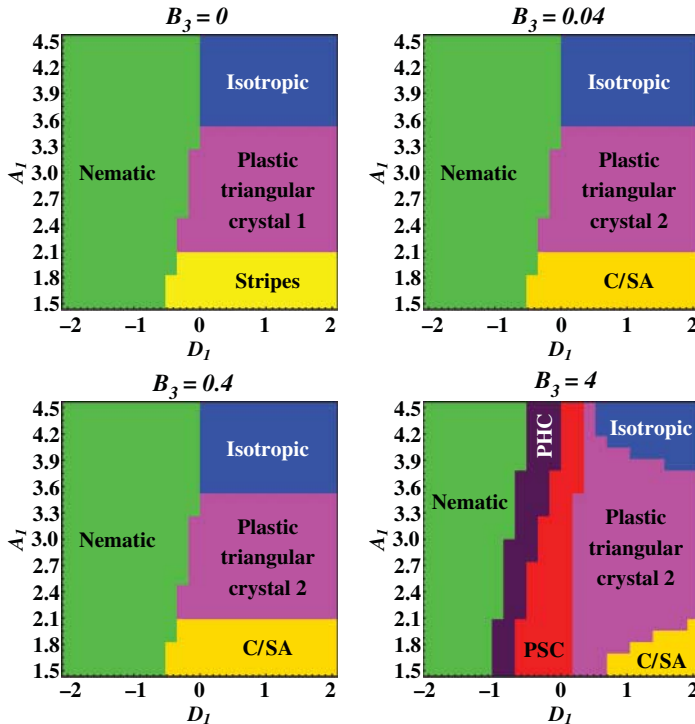


Figure 18. Phase diagrams for the parameters $A_2 = 14$ and $D_2 = 0.8$. The relevant liquid crystalline phases are isotropic (blue), nematic (green), stripes (yellow), columnar/smectic A (C/SA, light orange), plastic triangular crystals (magenta), plastic honeycomb crystal (PHC, dark purple), and plastic square crystal (PSC, red). The cornered separation lines between different phases are due to the finite numerical resolution of the parameter space. (Reproduced from Achim *et al.* [69] © 2011 by the American Physical Society.)

3.3. Anisotropies in the PFC models

One of the most attractive features of the PFC-type models is that the anisotropies for various physical properties follow directly from the crystal structure. The anisotropy of the interfacial free

energy has been addressed theoretically and numerically by several authors [33,40–44], whereas the growth anisotropy has been evaluated numerically in 3D [42].

3.3.1. Free energy of the liquid-solid interface

3.3.1.1 Numerical results. Backofen and Voigt [43] have determined the anisotropy of the crystal-liquid interfacial free energy for small 2D clusters from simulations performed using the 1M-PFC model. They have observed a strong dependence of the interfacial free energy on the distance from the critical point. The results have been fitted with the formula of Stashevich *et al.* [190] from low temperature expansion. Remarkably, the anisotropy shows strong size-dependence, when reducing the cluster size to a few particles. Comparable results have been obtained by Gránásy *et al.* [33,38] for the equilibrium shapes in a broader reduced temperature range (Figure 19). Tóth *et al.* [28] evaluated the free energy and thickness of flat interfaces as a function of ϵ via solving the ELE for the equilibrium $(10\bar{1})$ triangular crystal-liquid interface, and have shown that mean-field critical exponents apply. A similar approach has been applied in 3D for a large number of orientations of the flat bcc-liquid interface forming at $\epsilon = 0.3748$. The orientation dependence of the interfacial free energy and the respective Wulff plot are presented in Figure 20 [44]. Apparently, the rhombic-dodecahedral equilibrium shape [42] obtained from simulations performed using the EOM for the same ϵ has been a growth form. It became also evident that the usual cubic harmonic expansion is not sufficient for reproducing reasonably the anisotropy even if terms up to seventh order are considered.

3.3.1.2 Analytical results. Wu and Karma [40] have used multi-scale analysis close to the critical point ($0 < \epsilon \ll 1$) to evaluate the anisotropy of the interfacial free energy. They have approximated the EOM of the 1M-PFC model by a set of coupled equations describing the time

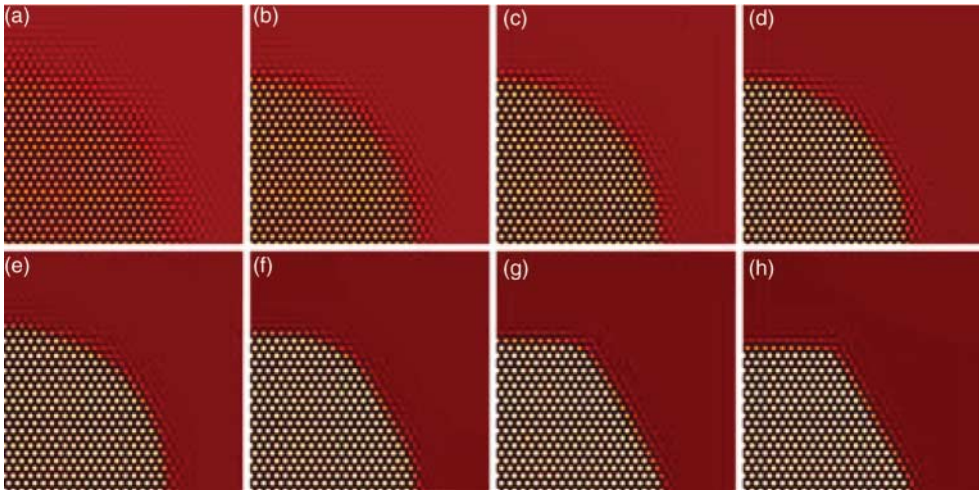


Figure 19. Equilibrium shape for the 1M-PFC model as determined by solving the EOM vs. reduced temperature ϵ in the absence of noise [33]. (a) - (h): $\epsilon = 0.05, 0.10, 0.15, 0.20, 0.25, 0.30, 0.325,$ and 0.35 . Note that the interface thickness decreases while the anisotropy increases with an increasing distance from the critical point. The computations have been performed on a 1024×1024 rectangular grid (the upper right quarter of the simulations is shown), whereas the crystalline fraction was ≈ 0.3 . Equilibration has been performed for a period of 106 dimensionless time steps. Reduced particle density maps are shown. (Reproduced from Gránásy *et al.* [33] © 2011 by Taylor & Francis.)

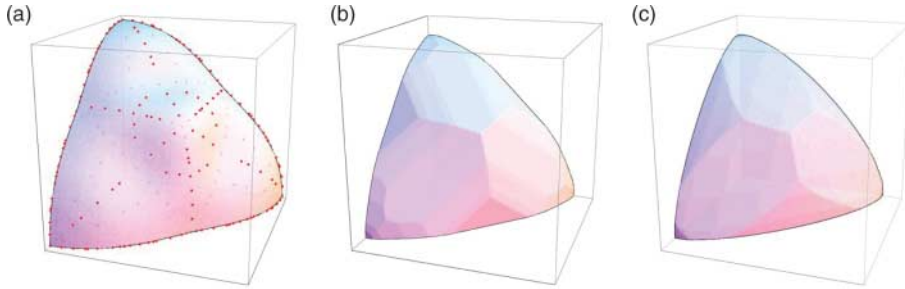


Figure 20. Anisotropy of the bcc-liquid interfacial free energy at $\epsilon = 0.3748$ evaluated numerically for the single-component 1M-PFC model and the respective equilibrium shapes [44]. (a) Gamma plot. Dark dots (red online) represent the directions for which the interfacial free energy has been evaluated. The surface is a seventh-order cubic harmonics fit. Heavy dots are on the viewer's side of the surface. Light dots are on the other side of the surface. (b) Wulff shape evaluated from the red dots in the gamma plot. (c) The Wulff shape evaluated from a seventh-order cubic harmonics fit to the gamma plot.

evolution of the amplitudes of the dominant density waves. The analysis of the stationary solution led to an anisotropy that is independent of the reduced temperature ϵ . This finding accords with those of Majaniemi and Provatas [41], who have used a simple coarse-graining technique, the local volume averaging method, for deriving amplitude equations for liquid–solid interfaces broad relative to the periodicity of the crystalline phase. In both studies, the temperature-independent anisotropy is a direct consequence of the approximations that lead to weakly fourth-order amplitude theories of the Ginzburg-Landau type, in which all material parameters can be scaled out from the free-energy functional [40,41]. Accordingly, the anisotropy of the interfacial free energy depends only on the crystal structure. However, this independence of the anisotropy from temperature is unphysical, as it must vanish when the correlation length (the width of the liquid-solid interface) diverges in the critical point. In contrast to these phenomenological coarse-graining techniques, the renormalization-group-based approaches by Athreya *et al.* [141] lead to higher-order amplitude equations, from which the temperature cannot be scaled out; that is, a temperature-dependent anisotropy is expected as found in the virtually exact numerical studies.

3.3.2. Growth anisotropy

Tegze *et al.* [42] have investigated the growth rate anisotropy in the 1M-PFC model at $\epsilon = 0.3748$ for freezing to the bcc, hcp, and fcc structures. Diffusion-controlled layerwise crystal growth has been observed, a mechanism that is consistent with two-dimensional nucleation. The predicted growth anisotropies were found to decrease with increasing thermodynamic driving force (or velocity) consistently with kinetic roughening expected on the basis of 1M-PFC simulations performed in 2D [38].

3.4. Glass formation

One of the most intriguing phenomena that may happen during solidification is glass formation, a process by which the undercooled liquid is transformed into an amorphous solid. An early 1M-PFC study for single-component system by Berry *et al.* [46] relying on conservative overdamped dynamics indicated a first-order phase transition for this phase change, whereas the amorphous structure resembled closely to the glass structure obtained by embedded-atom-potential (EAP) MD simulations for glassy Fe or Ni [191,192]. These findings have been confirmed for the 1M-PFC model by Tóth *et al.* [151] and for the EOF-PFC model fitted to Fe by Tóth *et al.* [28] and

Gránásy *et al.* [33]. In a more recent study, Berry and Grant [47] have addressed glass formation in the framework of the monatomic and binary versions of the VPFC model with equation(s) of motion like Equation (64) considering inertia and damping. They have shown that important aspects of glass formation can be reproduced over multiple time scales, including the agreement with mode-coupling theory (MCT) for underdamped liquids at low undercoolings and a rapidly growing dynamic correlation length that can be associated with a fragile behaviour. It appears that in the original PFC model glass formation takes place via a first-order phase transition, while the monatomic VPFC model behaves like poor glass formers, whereas the binary VPFC model displays features consistent with good glass formers.

3.5. Phase-field-crystal modelling of foams

Working at extreme distances from the critical point, Guttenberg *et al.* [70] have shown that the 1M-PFC model can be used to describe the formation of foams. Under such conditions, the free energy of the periodic phases exceeds that for a mixture of two immiscible liquids – a situation that leads to the appearance of a foam-like structure coarsening with time. Starting from this observation, the authors present a simple PFC-type continuum scalar theory of wet and dry foams (Figure 21).

3.6. Coupling to hydrodynamics

An interesting approach has been brought forward recently by Ramos *et al.* in reference [54]. It couples the PFC dynamics of the form of Equation (1) to a Stokes-type dynamics as well as to an external pinning potential. The general set of equations the authors arrive at is given by

$$\begin{aligned}\frac{\partial \rho}{\partial t} &= -\nabla_{\mathbf{r}} \mathbf{g}, \\ \frac{\partial g_i}{\partial t} &= -\rho \partial_i \frac{\delta H_{\text{int}}}{\delta \rho} + \rho f_i - \eta g_i + v_i,\end{aligned}\tag{117}$$

where the specific configurational energy contribution H_{int} needs to be specified depending on the system. Assuming a periodic system, it is specified in reference [54] as

$$H_{\text{int}} = \int d\mathbf{r} \left(\frac{\psi}{2} (-\epsilon + (1 + \nabla_{\mathbf{r}}^2)^2) \psi + \frac{\psi^4}{4} + \psi U_p \right).\tag{118}$$

In Equations (117), $\rho(\mathbf{r})$ and $\mathbf{g}(\mathbf{r})$ refer to particle and momentum density, respectively. Moreover, f_i denotes the components of an external force vector and $v_i(\mathbf{r}, t)$ denotes noise components. Furthermore, η is a dissipative coefficient and U_p accounts for the pinning potential.

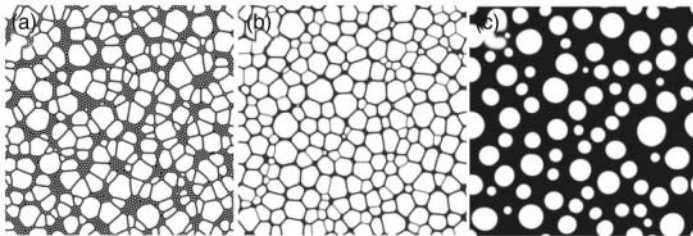


Figure 21. Foam structures predicted by the MPFC model. (a) Coexisting atoms and large cell foam. (b) Dry foam with no residual atoms. (c) Wet foam with circular bubbles. (Reproduced with permission from Guttenberg *et al.* [70] © 2010 by the American Physical Society.)

Even if at first glance, the coupled set of Equations (117) looks like a first step towards coupling of the PFC model based on Equation (1) to a full Navier–Stokes (NS) type equation and thus to hydrodynamic motion, a respective extension of Equations (117) is not straightforward due to the simple relation between particle density $\rho(\mathbf{r})$ and momentum density $\mathbf{g}(\mathbf{r})$ assumed. Thus instead of providing a step towards an extension of PFC models towards hydrodynamics, Equations (117) rather provide a general framework for the inclusion of inertia effects in PFC models. The latter issue has also been addressed in references [55,56,138], where it was shown that the consideration of inertia terms allows to include fast degrees of freedom into the PFC approach. Furthermore, the authors of reference [138] have shown that inclusion of such fast degrees of freedom yields a two-stage relaxation process of the system. Chen *et al.* proved the thermodynamic consistency of such models with fast degrees of freedom [193]. Thereby, these authors validated from the viewpoint of thermodynamic theory that such a two-stage relaxation process can truly be regarded as an important qualitative feature of non-equilibrium pattern formation in periodic systems. To do so, they developed a unified thermodynamic framework applying to both conventional PF models and PFC models with slow and fast degrees of freedom. Based on this framework it is now possible to validate also PFC models based on their thermodynamic consistency, as done previously in numerous cases for PF models (see reference [194] for examples). Experimental evidence of inertia contributions to the dynamics of a nonlinear system in the form described by the PFC model with fast degrees of freedom can indeed be found for example in rapid solidification [138].

The coupling of PFC models to hydrodynamics, though, is still an open issue. It makes sense to distinguish two cases:

Case (a): Liquid-solid systems as, for example, solidifying alloys, where hydrodynamic transport takes place in only the liquid phase. This implies that such systems can be treated in a multi-scale approach, where the PFC equation for the atomic scale dynamics in the interior of the solid is coupled to the long-range transport processes in the exterior, which – to be numerically efficient – couple only to the amplitude equation of the PFC equation. The reason is that in the case of PFC models it is the amplitude equation, which distinguishes between solid and liquid. Such amplitude equation approaches have been derived and solved numerically as computationally efficient representatives of PFC models, for example, for diffusion limited polycrystalline grain growth [20] based on renormalization group techniques (see Section 3.1.5.1 for details). Since renormalization for PFC models of Equation (1) type does not directly yield NS-type equations and thus a coupling to hydrodynamics exploiting the above multi-scale idea, this is still an open issue.

Case (b): This case differs from the above picture in that it applies to systems, for which interatomic respectively intermolecular fluidic motion needs to be taken into account as, for example, in polymers. Then one would desire a PFC model, where the PFC equation itself is directly coupled to a NS-type equation. A first step in that direction was done by Praetorius *et al.* [195]. They developed a PFC model with an advective term to simulate particles in a flowing solvent. To do so they followed the same route as Rauscher *et al.* [196] and Penna *et al.* [197] to derive a DDFT model for such systems, and approximated the latter further based on the Ramakrishnan–Yussouff approximation [94]. Strictly speaking the resulting PFC model applies only to potential flows. Furthermore, the coupling of the PFC variable ψ into the dynamic equations for the hydrodynamic field is constructed simply based on numerical arguments. More rigorous generalizations of these studies might require additional physically motivated coupling terms, as demonstrated for hydrogels in terms of the derivation of the corresponding PF model in reference [198] (see Section 5.2 for details).

Just as in the PF case, one can expect efficient further advance of PFC models in the future. Progress will result from physical modelling concepts based upon the classical routes to patterned

nonlinear systems [1], analytical mathematical expansion techniques as the renormalization group approach (see Section 3.1.5.1 for details), and advanced numerical approaches [195,199] in close comparison to experimental techniques.

4. Phase-field-crystal models applied to nucleation and pattern formation in metals

As pointed out in reference [71], crystal nucleation can be handled in two different ways within the framework of PFC models [28,33,35]: (i) via finding the properties of the critical fluctuations (nuclei) by solving the ELE under appropriate boundary conditions (zero field gradients at the centre and unperturbed liquid phase in the far field), whose solution represents an extremum of the free-energy functional; (ii) by adding noise to the EOM. These approaches have their limitations [71]: (i) is expected to work for small undercoolings, where the individual heterophase fluctuations do not interact. In addition, it is not immediately straightforward how one should address possible non-crystalline nucleation precursors. In turn, in the case of (ii) it is not clear conceptually, which fraction of the thermal fluctuations has already been integrated into the free energy, and which wavelengths should yet be added as noise to the EOM [104,200,201] – a question, inherently related to the proper choice of the high frequency cutoff needed to avoid an ultraviolet catastrophe in 3D [202,203]. Furthermore, the addition of noise to the EOM changes such properties as the free energy, the phase diagram, and the interfacial properties. In principle, a correction of this difficulty is possible via parameter renormalization [204,205], however, further study is needed in the case of PFC models. On the other hand, the original free-energy functional used in (i) seems to miss the effect of longer wavelength fluctuations, which could move the system out of a metastable state [71]. Considering these, (i) and (ii) may be regarded as approaches that provide complementary, though qualitative information of the crystallizing system, which converge when the amplitude of the noise tends to zero [71].

We note, however, that the results obtained via route (i) are more general than those obtained from (ii), as they follow directly from the free-energy functional, being therefore independent of the type of dynamics the EOM defines. Accordingly, results from (i) are valid even in cases, where the colloid-type diffusive dynamics is not applicable (e.g. metals). In this section, we review results obtained following route (i) for metals, or when pattern formation is governed by either chemical or surface diffusion. In turn, results obtained with the single-component PFC models with overdamped diffusive dynamics will be reviewed in Section 5.1.

4.1. Properties of nuclei from extremum principles

4.1.1. Homogeneous nucleation

Backofen and Voigt [32] have adapted the string method for finding the saddle point of the free-energy functional, when determining the properties of the critical fluctuations appearing in the 1M-PFC model in 2D. The respective density profiles are displayed in Figure 22. Apparently, there are no bulk crystal properties at the centre of the smallest nuclei forming at large supersaturations. Another interesting finding is that the small nuclei are faceted even though the large crystals are not.

Tóth *et al.* [28] have solved in 2D the ELE of the 1M-PFC model for the appropriate boundary conditions (homogeneous supersaturated liquid in the far field) to find the free-energy extrema for faceted clusters far from the critical point ($\epsilon = 0.5$), where even the large crystals are inherently faceted. Under such conditions, the free-energy surface has many local minima [28,155] that map out the shape of the free-energy barrier for nucleation as a function of cluster size (Figure 23(a)). It has also been reported that the effective interfacial free energy deduced from the barrier height

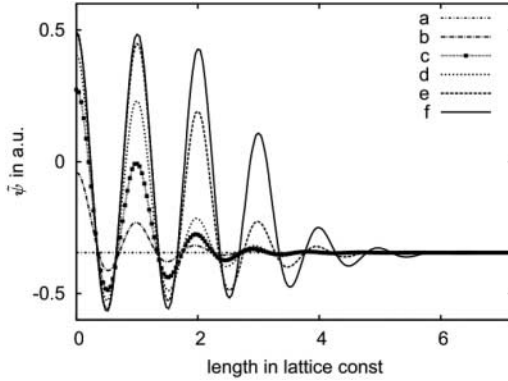


Figure 22. Particle density profiles for the critical fluctuations forming at different supersaturations (supersaturation decreases from a to f), as obtained by the adaptation of the string method for determining the extrema of the free-energy functional in the 1M-PFC model in 2D. (Reproduced with permission from Backofen and Voigt [32] © 2010 by Institute of Physics Publishing.)

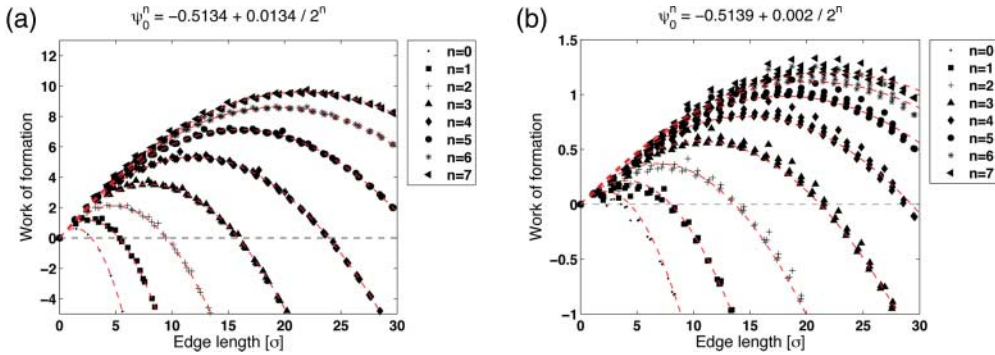


Figure 23. Nucleation barrier vs. size relationship obtained by solving the ELE for faceted nuclei ($\epsilon = 0.5$) for the 1M-PFC model [28] in 2D: (a) homogeneous crystal nuclei for $\psi_0^n = -0.5134 + 0.0134/2^n$, where $n = 0, 1, 2, \dots, 7$, respectively. (b) Heterogeneous crystal nuclei for $\psi_0^n = -0.5139 + 0.002/2^n$, where $n = 0, 1, 2, \dots, 7$, respectively. The lattice constant of the substrate is equal to the interparticle distance in the triangular crystal. Note the substantial reduction of the nucleation barrier, a monolayer adsorption layer, and the contact angle of 60° determined by the crystal structure. (Reproduced from Tóth *et al.* [28] © 2010 by Institute of Physics Publishing.)

using the hexagonal classical cluster model (valid owing to the interface sharp on the atomic scale) converges towards the free energy of the planar interface as the supersaturation decreases [28].

Tóth *et al.* [28] have performed a similar ELE analysis in 3D to study for heterophase fluctuations forming in the 1M-PFC model. They have evaluated the properties of crystal nuclei for bcc and fcc structures. It has been found that under the investigated conditions both the nucleation barrier and the driving force are fairly close for these structures, indicating comparable interfacial free energies and also Turnbull’s coefficient⁹ for the bcc and fcc structures under conditions ($\epsilon = 0.3748$), where the thermodynamic properties of the crystalline phases are rather close [42]. This seems to contradict recent results from MD simulations performed using the EAP method [206]. It is worth noting, however, that Turnbull’s coefficient varies with the type of interaction potential. For example, it is ≈ 0.55 for EAP metals of fcc structure [206], whereas ≈ 0.36 has been deduced for the fcc Lennard-Jones (LJ) system [207].

4.1.2. Heterogeneous nucleation

The height of the nucleation barrier is often reduced by heterogeneities (walls, floating particles, templates, etc.), a phenomenon termed heterogeneous nucleation [208]. The efficiency of the heterogeneities in instigating freezing is influenced by a range of microscopic properties, such as crystal structure, lattice mismatch, surface roughness, adsorption, etc., which are often condensed into the contact angle used in the classical theory and coarse-grained continuum models. The atomic scale characteristics of the substrate surface, especially the lattice mismatch, are crucial from the viewpoint of the highly successful free-growth-limited model of particle-induced freezing by Greer and co-workers [208,209] – a model in which cylindrical particles, whose circular faces (of radius R) are ideally wet by the crystal, remain dormant during cooling until the radius of the homogeneous nuclei becomes smaller than R and free growth sets in. The PFC models are especially suitable to investigate such problems as they work on the diffusive time scale [12] and can handle systems containing as many as 2.4×10^7 atoms [28].

Along this line, Tóth *et al.* [28] used a *periodic* external potential to incorporate a crystalline substrate into the ELE method for determining the properties of faceted heterogeneous nuclei. They have observed the adsorption of a monolayer of particles on the surface of substrate that reduced the formation energy of nuclei substantially and lead to a contact angle of 60° determined by the crystal structure (Figure 23(b)). In a more recent ELE study, Tóth *et al.* [151] have shown for the 1M-PFC model in 2D that the contact angle, the thickness of the crystal layer adsorbed on the substrate, and the height of the nucleation barrier vary non-monotonically with the lattice constant of a square-lattice substrate (Figure 24). They have also proven in 2D and 3D that the free-growth-limited model of particle-induced freezing by Greer *et al.* [208,209] is valid for larger nanoparticles and a small anisotropy of the interfacial free energy (Figure 25). Faceting due to either the small size of the foreign particle or a high anisotropy of the free energy of the liquid-solid interfacial free energy decouples free growth from the critical size of homogeneous nuclei.

4.2. Pattern formation

As pointed out in reference [71], owing to the overdamped diffusive dynamics most of the PFC models assume, diffusional instabilities that lead to fingering of the propagating crystal front are inherently incorporated. In the case of a single-component PFC model, diffusive dynamics means that as the growing crystal (of larger particle density than the liquid) consumes the particles in the adjacent liquid, the only way they can be replenished is via long-range diffusion from the

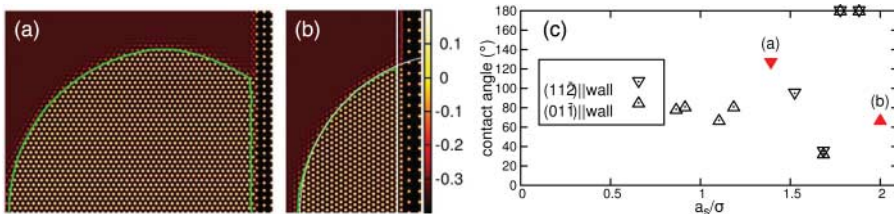


Figure 24. Heterogeneous crystal nucleation at a wall in 2D from solving the ELE [151]: (a), (b) typical (non-faceted) nuclei obtained for $\epsilon = 0.25$, $\psi_0 = -0.341$, while the ratio of the lattice constant of the substrate and the particle diameter is $a_s/\sigma = 1.49$ and 2.0 , respectively, whereas the crystal orientations $(11\bar{2})$ and $(01\bar{1})$ are parallel with the wall. The intersection of the circular and linear fits (white lines) to the contour line (green online, light grey in print) defines the contact angle. (c) Contact angle vs. a_s/σ for $\epsilon = 0.25$ and $\psi_0 = -0.341$. The full symbols indicate the states corresponding to panels (a) and (b). (Reproduced from Tóth *et al.* [151] © 2012 by the American Physical Society.)

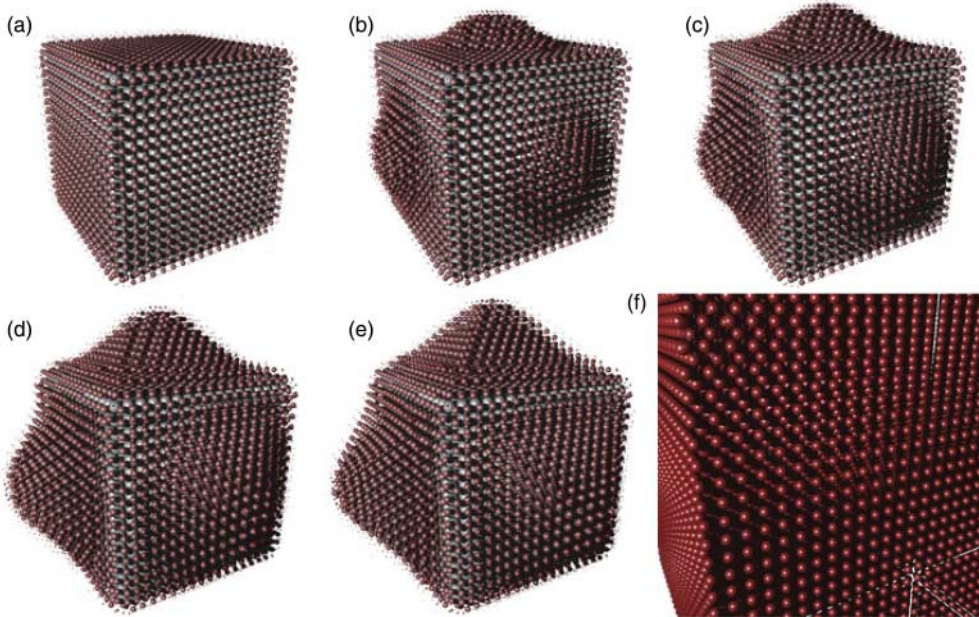


Figure 25. Free-growth limited bcc crystallization in 3D on a cube of sc structure as predicted by the ELE within the 1M-PFC model [151]. Here, $\epsilon = 0.25$ and from left to right $\psi_0 = -0.3538, -0.3516, -0.3504, -0.3489, -0.3482$, and -0.3480 , respectively. The linear size of the substrate is $L_s = 16a_{\text{bcc}}$, while a_{bcc} is the lattice constant of the stable bcc structure. Spheres centred on density peaks are shown, whose size increases with the height of the peak. Colour varies with peak height, interpolating between dark grey (red online) (minimum height) and light grey (maximum height). The ELE has been solved on a $256 \times 256 \times 256$ grid. (Reproduced from Tóth *et al.* [151] © 2012 by the American Physical Society.)

bulk liquid. Accordingly, a depletion zone forms ahead of the growing crystal [28,38,42,210]. This resembles the behaviour of colloidal suspensions, in which the micron-sized colloid particles move by Brownian motion in the carrier fluid. Relying on this similarity, the single-component PFC models can be considered as reasonable tools to address colloidal crystal aggregation [71]. One may, however, get rid of this type of mass-diffusion-controlled dynamics when driving the system strongly enough for a diffusion-controlled to diffusionless transition [38]. These phenomena are not necessarily present in the phenomenological coarse-grained PFC models, where the change in density upon crystallization is not always taken into account – models that might be considered, therefore, as a reasonable description of metallic alloys. Diffusive dynamics is furthermore appropriate on the surface of substrates, where the adsorbed particles indeed move by diffusion in a periodic potential. 2D PFC models relying on the interplay of the interparticle forces and a periodic external potential representing the symmetries of the substrate can be used to capture pattern formation on such surfaces.

4.2.1. PFC modelling of surface patterns

A combination of computer simulations with the solution of amplitude equations for PFC models equipped with periodic potentials has been used to investigate a range of surface phenomena including incommensurate to commensurate transitions for triangular surface layers on a square-lattice substrate [55–57], the deposition of monolayers on quasi-crystalline substrates [50,58],

sliding friction [54,56], and the formation of quantum dots/islands on nanomembranes [53,211] (Figure 26).

Muralidharan and Haataja [48] have extended the PFC model for describing stress-induced alloying of bulk-immiscible binary systems on a substrate by adding a potential energy term describing the substrate and a regular solution term. Fixing the model parameters to data for CoAg/Ru(0001), they demonstrated that the model captures experimentally observed morphologies. A sequential application of this model has been employed for addressing multilayer growth on crystalline and quasi-crystalline substrates [50]. A similar approach has been proposed by Elder *et al.* [49] using amplitude equations that allow large-scale simulations for stress-induced alloying in heteroepitaxial overlayers. Quantitative predictions, that are in an excellent agreement with experiments, have been obtained for the stripe, honeycomb, and triangular superstructures emerging in the metal/metal systems, Cu on Ru(0001) and Cu on Pd(111) (Figure 27).

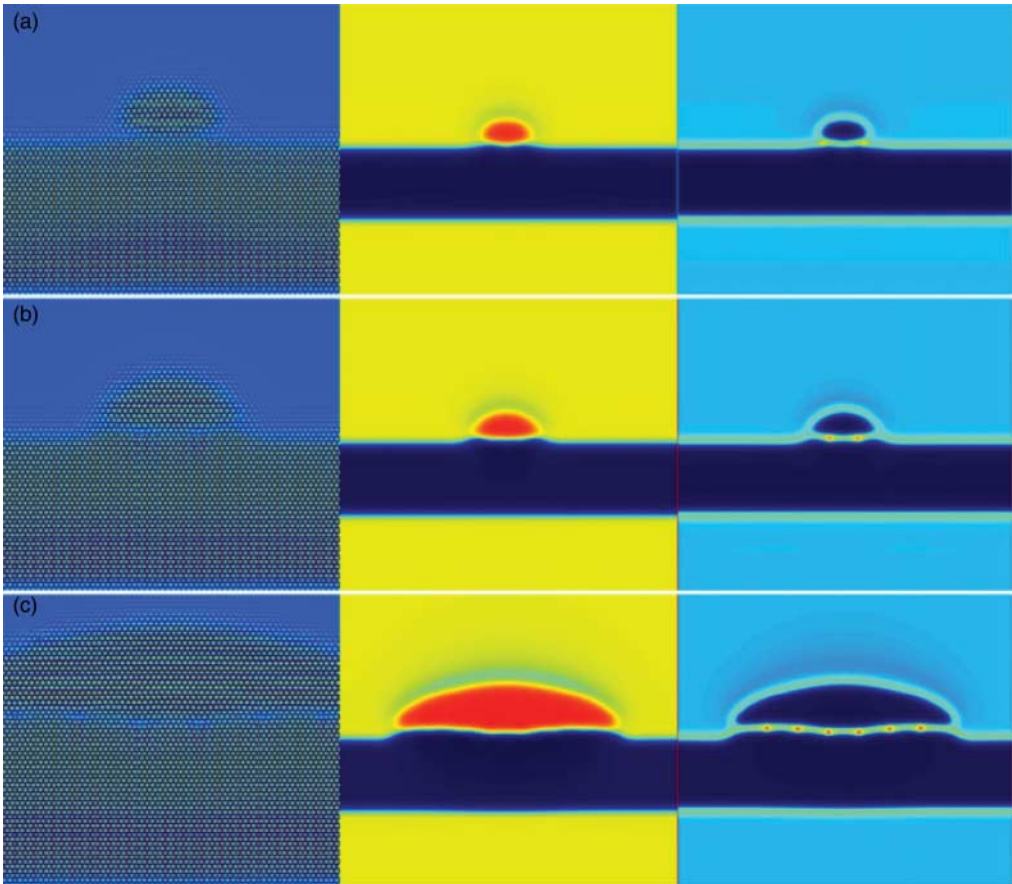


Figure 26. Growth of an island on a nanomembrane of approximately 30 atomic layers thickness at times (a) $t = 60,000$, (b) $t = 80,000$, (c) $t = 400,000$ as predicted by the amplitude equations of reference [53]. Similar to Figure 9, the left, middle, and right columns correspond to the results of the total particle density, the difference of the particle densities for the two components, and the local free-energy density, respectively. Also for clarity, the particle density images have been expanded by a factor of two. (Reproduced with permission from Elder and Huang [53] © 2010 by Institute of Physics Publishing.)

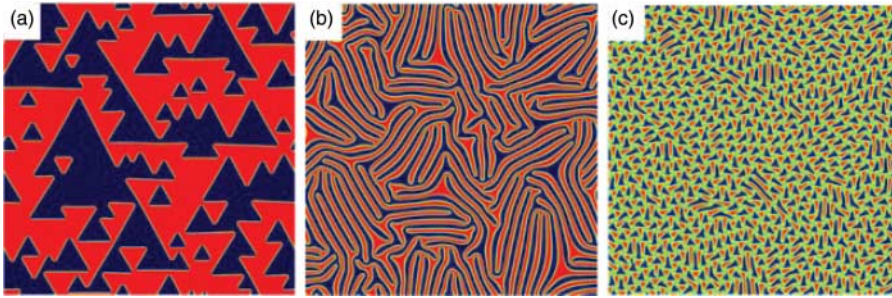


Figure 27. Surface patterns the amplitude equations predict for a decreasing dimensionless coupling u_0 between the layer and the substrate [49]. From left to right: $u_0 = 12.1 \times 10^{-3}$, 3.2×10^{-3} , and 0.87×10^{-3} , respectively. Colouring: fcc domains are dark grey (blue online), hcp domains are medium grey (red online), and the domain walls are light grey (green online). (Reproduced with permission from Elder *et al.* [49] © 2012 by the American Physical Society.)

4.2.2. Pattern formation during binary solidification

4.2.2.1 *Dendritic freezing.* The possibility of growing solutal dendrites has been first addressed within numerical 1M-PFC simulations by Elder *et al.* [26]. Studies of the transformation kinetics for many particles including several dendrites have been performed using the same approach by Pusztai *et al.* [27] for system sizes containing about 1.6×10^6 atoms (Figure 28). Tegze [29] has investigated the behaviour of solutal dendrites using binary 1M-PFC simulations of similar size. With increasing driving force obtained by increasing the total number density, transitions from dendritic needle crystals to compact hexagon shape crystals have been observed as in the conventional PF models (Figure 29). It has also been shown that (i) a steady state tip velocity is attained after a time, and (ii) tip oscillations do not occur, that is, from the viewpoint of side branch formation the dendrite tip works like a selective amplifier of the fluctuations at the tip (Figure 30).

4.2.2.2 *Eutectic solidification.* Eutectic solidification in binary 1M-PFC simulations has been first observed in 2D in the seminal paper by Elder *et al.* [26]. The formation of lamellar eutectic grains has been explored by Elder *et al.* [31] using an approach based on amplitude equations (Figure 31). For the relatively large lattice mismatch they assumed for the two crystalline phases (8.4% in equilibrium), spontaneous nucleation of dislocations at the lamellar interfaces has been observed – a phenomenon expected to modify the spacing selection mechanism predicted by earlier

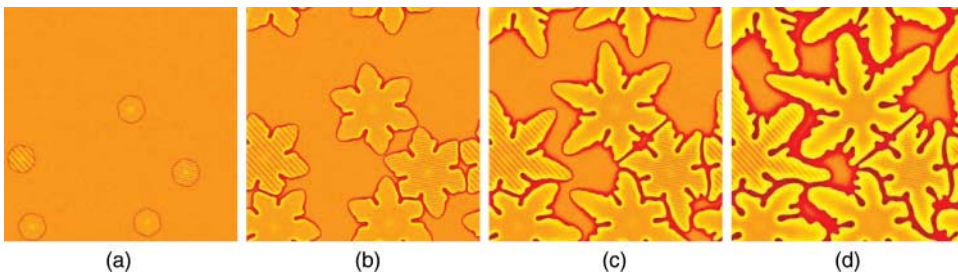


Figure 28. Growth of five dendrites in the binary PFC model (the distribution of the field $\hat{\psi}$ is shown). The snapshots taken at 1000, 5000, 10,000 and 20,000 time steps are shown. The simulations have been performed on a 16384×16384 grid, using a semi-implicit spectral method [177]. (Reproduced from Pusztai *et al.* [27] © 2008 by Institute of Physics Publishing.)

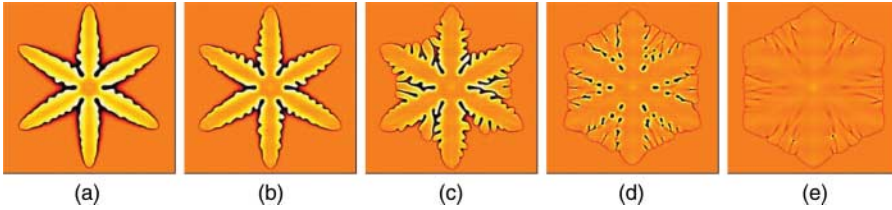


Figure 29. Morphological transition from dendritic needle crystals to compact hexagonal shape with increasing driving force for crystallization [29]. Conditions/properties are as described for dendrites in reference [177] except that the initial total number densities are $\psi_0 = 0.009, 0.0092, 0.0094, 0.0096,$ and 0.0098 (from left to right). The reduced number density $\hat{\psi}$ is shown. Note the reducing contrast of the images from left to right indicating an increasing solute trapping. A 8192×8192 grid has been used. (Reproduced from Tegze [29]).

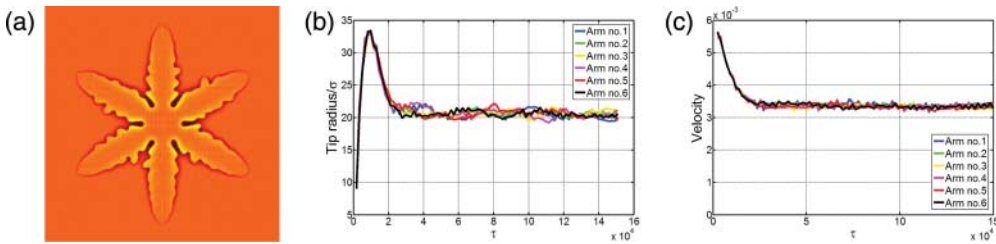


Figure 30. Analysis of a solutal dendrite grown in the binary 1M-PFC model [29]. The dendrite arms are numbered clockwise from the top arm. Apparently, there are no tip radius or velocity oscillations and steady state growth is reached after ≈ 4000 time steps. A 8192×8192 grid has been used and $\psi_0 = 0.0092$, whereas other conditions as for Figure 25 are present. (Reproduced from Tegze [29]).

eutectic solidification theories. Larger-scale binary 1M-PFC simulations relying on a numerical solution of the EOMs (73) and (74) in 2D imply that owing to the diffusive dynamics of the total particle density in the binary 1M-PFC model, eutectic colonies may form even in binary systems [28] (Figure 32). Here, the morphological change occurs as a result of the diffusional instability emerging from the diffusive EOM, many of the PFC models assume. Using the same approach in 3D, eutectic crystallization to the bcc structure has been reported by Tóth *et al.* [28] (Figure 33). These atomistic simulations indicate a remarkable time evolution of the eutectic pattern after solidification.

4.3. Phenomena in the solid state

One of the most successful areas, where the PFC models make a real difference is the modelling of solid state transitions including grain-boundary dynamics, melting, crack formation, stress-induced morphology evolution, and the modelling of the Kirkendall effect, to mention a few. This follows from the fact that, working on the atomistic scale, the PFC methods incorporate the dislocations inherently. In contrast, the coarse-grained continuum approaches model dislocation dynamics via their energetic contribution. The PF models following the seminal work of Chen *et al.* [212,213] integrate microelasticity into the PF formalism [214], enabling thus the description of *coherent* martensitic transformations in single [215] and polycrystalline systems [216]. This PF methodology of dislocation kinetics has been developed consecutively in a series of articles [217–220]. A versatile and numerically efficient microelastic PF model has been put forward

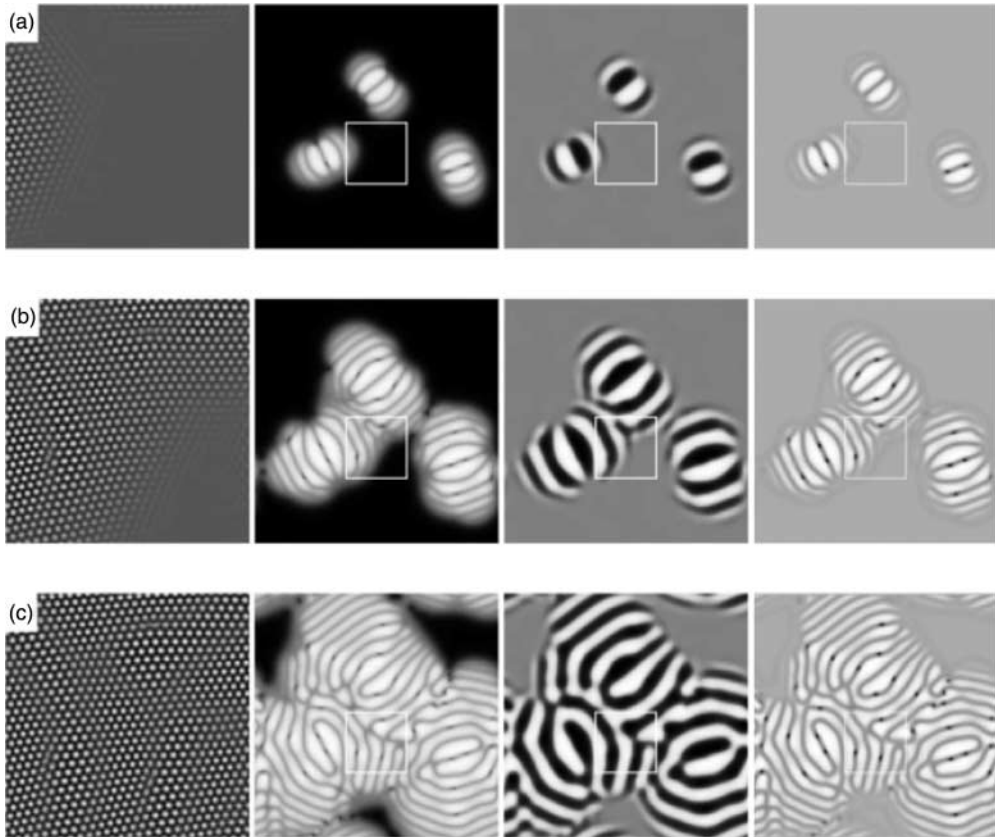


Figure 31. Time evolution of equiaxed eutectic solidification within the amplitude equation formalism proposed by Elder *et al.* [31]. Panels (a), (b), and (c) correspond to dimensionless times 30,000, 60,000, and 105,000, respectively. From left to right the columns display the reduced total number density in the boxed region, the coarse-grained number density, the reduced difference of the number densities for the two species, and the local free-energy density. Dislocations appear as small black dots in the local free-energy density. (Reproduced with permission from Elder *et al.* [31] © 2010 by the American Physical Society.)



Figure 32. Snapshots of eutectic solidification on the atomistic scale in the binary 1M-PFC model in 2D [28]: composition $\hat{\psi}$ maps corresponding to 2×10^5 , 6×10^5 , and 10^6 time steps are shown. White and black denote the two crystalline phases, while grey (orange online) stands for the liquid phase. The simulation has been performed on a 2048×1024 rectangular grid. Crystallization has been started by placing a row of supercritical crystalline clusters of alternating composition into the simulation window. Interestingly, the eutectic pattern evolves inside the solid region on a timescale comparable to the timescale of solidification. (Reproduced from Tóth *et al.* [28] © 2010 by Institute of Physics Publishing.)

recently [214]. It relies on a dislocation density field whose evolution follows an advanced constitutive model of plastic slip from micromechanics [221–223]. Although the micromechanical PF models have successfully addressed various phenomena associated with dislocation dynamics,

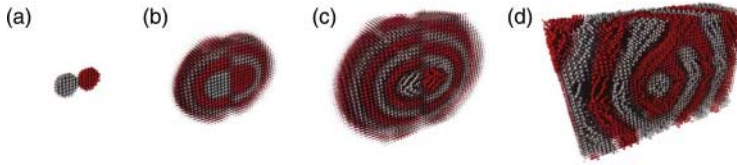


Figure 33. Snapshots of eutectic solidification as predicted by the binary 1M-PFC model in 3D [28]; time elapses from left to right. The simulation has been performed on a $450 \times 300 \times 300$ rectangular grid. Solidification has been started by placing two touching supercritical bcc clusters of different compositions into the simulation window. Remarkably, the nanoscale solid-phase eutectic pattern roughens on a timescale comparable to the time of solidification. Brown and grey colours denote the terminal solutions of the two crystalline phases. Spheres of size reflecting the height ψ of the total number density peak and coloured according to the local composition $\hat{\psi}$ are centred to the particle density maxima. Only half of the simulation window is shown. (Reproduced from Tóth *et al.* [28] © 2010 by Institute of Physics Publishing.)

the atomistic approach the PFC models realize offers a more detailed description as illustrated in the following.

4.3.1. Dislocation dynamics and grain-boundary melting

Already the first paper on the PFC method [12,59] has addressed grain boundaries and shown that the model automatically recovers the Read-Shockley relationship between grain-boundary energy and misorientation (Figure 34). It has also been shown that PFC models are ideal for modelling grain-boundary dynamics [12,59] (Figure 34) and offers the possibility to link mechanical properties with the grain structure [59]. Two mechanisms of dislocation glide have been observed: for high strain rates, continuous glide is observed, while at the lower strain rate, the dislocation set into a stick-slip motion [61]. Grain rotation and the associated grain-boundary motion have been addressed in detail by Wu and Voorhees [224]. While observing classical linear area-shrinkage in time for large and small grain misorientations, they report non-classical dynamics for intermediate initial grain misorientations, a phenomenon associated with specific rearrangement of dislocations during shrinkage. Grain-boundary melting has been addressed in several works [36,37,180]. It has

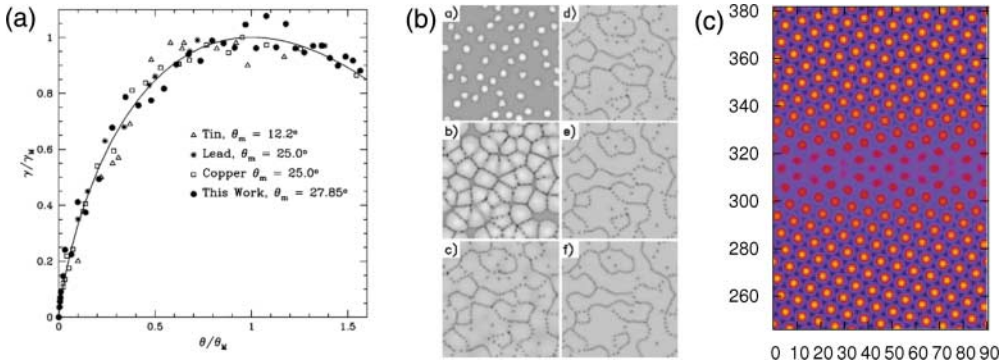


Figure 34. PFC modelling of defect and pattern formation in solids. From left to right: (a) grain-boundary energy vs. Read-Shockley relationship and (b) grain-boundary dynamics. (Reproduced with permission from Elder and Grant [59] © 2004 by the American Physical Society.) (c) Grain-boundary melting at a large-angle grain boundary. (Reproduced with permission from Mellenthin *et al.* [37] © 2008 by the American Physical Society.)

been reported that dislocations in low-angle to intermediate-angle grain boundaries melt similarly until an angle-dependent first-order wetting transition occurs, when neighbouring melted regions coalesce. In the large-angle limit, the grain-boundary energy becomes increasingly uniform along its length and can no longer be interpreted in terms of individual dislocations (Figure 34). The difference between high- and low-angle boundaries appears to be reflected in the dependence of the disjoining potential on the width of the pre-melted layer w : it is purely repulsive for all widths for misorientations larger than a critical angle, however, it switches from repulsive at small w to attractive for large w [37].

4.3.2. Crack formation and propagation

Crack formation and propagation are inherent multiscale problems, since in the vicinity of a crack tip time and length scales diverge. As outlined in reference [225], on the atomic length scale crack propagation is understood as a successive breaking of bonds.

Large scale MD simulations up to about 10^7 atoms allow a deeper insight into the growth of cracks [226–229]. Although limited to sub-micron samples and very short times, these simulations are able to reproduce key features of crack propagation like the initial acceleration and the onset of instabilities. The predictions, however, depend significantly on the employed model potentials [229,230].

Continuum descriptions of fracture offer a complementary view on the experimentally relevant length and time scales [225]. In the classical theory of macroscopic fracture, the crack is represented by a mathematical cut with no internal dimension, that is, a single crack is described by its tip-velocity and its path [231]. This of course neglects atomistic effects such as roughening of the crack surfaces.

The PFC models provide yet another atomistic approach, however, on a time scale considerably longer than that of the MD simulations. Elder and Grant [59] have demonstrated that the 1M-PFC model can be used to model crack propagation. A small notch cut out of a defect-free crystal placed under 10% strain in the vertical direction and filled with coexisting liquid has been used as a nucleation site for crack propagation. Snapshots of crack development are shown in Figure 35.

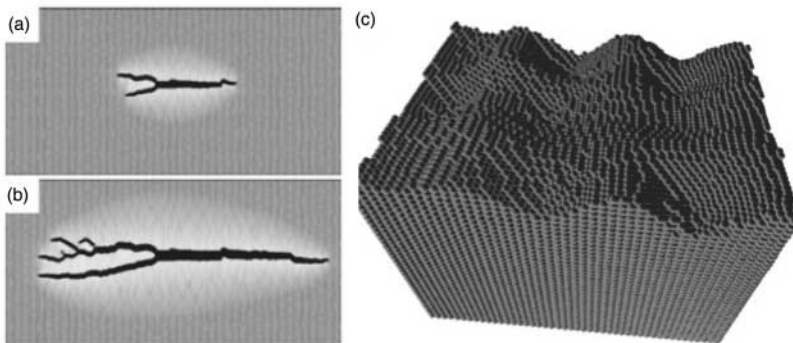


Figure 35. Crack formation (left) and strain-induced epitaxial islands (right) in the single-component 1M-PFC model. (a), (b) Snapshots of the energy density map taken at dimensionless times 25,000 and 65,000. (Reproduced with permission from Elder and Grant [59] © 2004 by the American Physical Society.) (c) Grey scale image of epitaxial islands in an 1M-PFC simulation for a 4.8% tensile film. (Reproduced with permission from Huang and Elder [51] © 2008 by the American Physical Society.)

4.3.3. *Strain-induced morphologies*

Huang and Elder [51] have studied strain-induced film instability and island formation using numerical 1M-PFC simulations and amplitude equations (Figure 34). They have identified a linear regime for the island wave number scaling and recovered the continuum ATG instability in the weak strain limit. The ATG instability has been studied in 2D by Spatschek and Karma [63] using a different amplitude equations approach. Qualitatively similar surface roughening has been reported by Tegze *et al.* [42] for heteroepitaxial body-centred tetragonal (bct) films grown on sc crystalline substrates of tuned lattice constant – a phenomenon interpreted in terms of the Mullins-Sekerka/ATG instability. Wu and Voorhees have shown [232] that the 1M-PFC predictions deviate from those of the classical sharp interface continuum model when the critical wavelength of the ATG instability becomes comparable to the interface width. They also report that nonlinear elastic effects due to large stresses alter the critical wavelength and the morphology of the interface.

4.3.4. *Kirkendall effect*

Elder *et al.* [64] have used a simple extension of the binary 1M-PFC model incorporating unequal atomic mobilities to investigate different aspects of the Kirkendall effect. They have shown that the model indeed captures such phenomena as crystal (centre-of-mass) motion, pore formation via vacancy supersaturation, and enhanced vacancy concentration near grain boundaries.

4.3.5. *Density/solute trapping*

In recent works by Tegze *et al.* [38,39], it has been reported for the 1M-PFC model (of diffusive dynamics) that at large ϵ ($= 0.5$) and high driving force a transition from diffusion-controlled to diffusionless solidification can be observed, during which the interface thickness increases, whereas the density difference between the crystal and the liquid decreases drastically (Figure 36). This “density trapping” phenomenon is analogous to solute trapping observed in rapid solidification of alloys (where due to a lack of time for partitioning, solids of non-equilibrium compositions form) and can be fitted reasonably well using the models of Aziz [233] and Jackson *et al.* [234]. In a very recent work, Humadi *et al.* [45] have investigated solute trapping in the binary MPFC model. In agreement with the findings for density trapping, they have found that pure diffusive dynamics leads to a velocity-dependent partition coefficient that approaches unity for large velocities – consistently with the model of Aziz and Kaplan [235]. In contrast, the wavelike dynamics, the second-order time derivatives of the MPFC-type EOMs realize, leads to a solute trapping behaviour similar to the predictions of Galenko *et al.* [236].

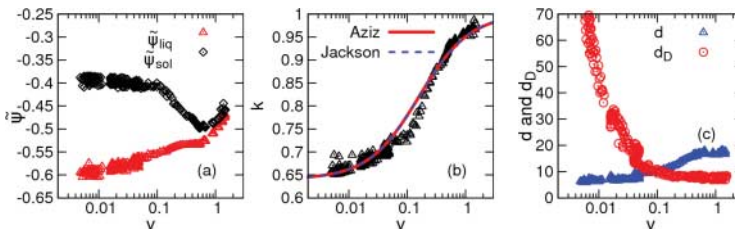


Figure 36. Density trapping as predicted by the single-component 1M-PFC model [38,39]. (a) Coarse-grained particle densities $\bar{\psi}$ for the liquid and solid phases at the growth front as a function of growth velocity v . (b) Effective partition coefficient k defined using the liquidus and solidus densities vs. growth velocity. For comparison, fits of the models by Aziz [233] and Jackson *et al.* [234] are also displayed. (c) Comparison of the interface thickness d and the diffusion length d_D as a function of growth velocity. (Reproduced from Tegze *et al.* [38] © 2011 by Royal Society of Chemistry Publishing.)

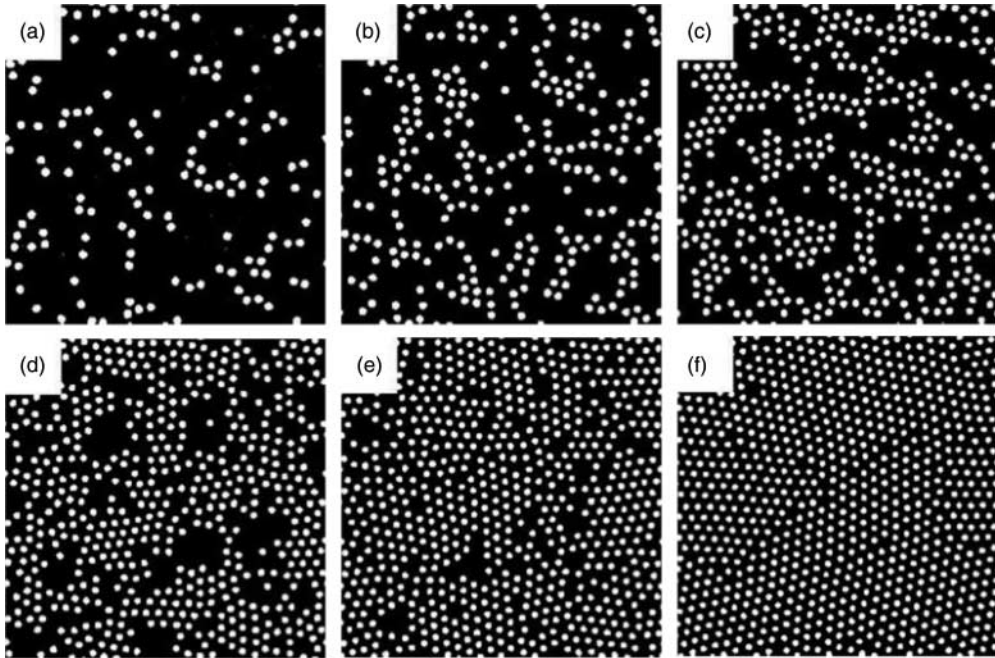


Figure 37. VPFC modelling of fluid and crystalline states of different particle densities. The number of atoms increases from left to right and from top to bottom. (Reproduced with permission from Chan *et al.* [65] © 2009 by the American Physical Society.)

4.3.6. Vacancy/atom transport in the VPFC model

The VPFC model by Chan *et al.* [65] is one of the most exciting extensions of the original PFC approach. The extra term added to the free energy makes particle density non-negative and allows for the formation of individual density peaks (“atoms” forming the fluid) and vacancies in the crystal. This, combined with the MPFC EOM (64), that considers inertia and damping, makes it a kind of MD-like approach working on a still far longer time scale than the usual MD simulations. Accordingly, one can obtain configurations that look like snapshots of the fluid state (Figure 37) and may evaluate the structure factor for the fluid state, which is evidently impossible for the original PFC model. (Apparently, similar images can be obtained in the 1M-PFC model as a *transient state* during solidification [38], however, with different dynamics owing to the differences in free energy and EOM.)

A comparison with another recent development, termed the diffusive molecular dynamics (DMD) technique, by Li *et al.* [237] would be very interesting. The latter approach works on the diffusive time scale too, while maintaining atomic resolution, by coarse-graining over atomic vibrations and evolving a smooth site-probability representation.

5. Phase-field-crystal modelling in soft matter physics

5.1. Applications to colloids

In this section, we review results obtained using different PFC models relying on overdamped conservative dynamics – a reasonable approximation for colloidal crystal aggregation. We concentrate on three major areas: crystal nucleation, pattern formation in free growth, and pattern formation in the presence of external potentials.

As mentioned previously, using of the EOM for simulating crystallization is not without difficulties. In the DDFT-type models, the system cannot leave a metastable state (e.g. the homogeneous initial fluid) unless Langevin noise representing thermal fluctuations is added to the EOM. This raises, however, essential questions: considering the number density an ensemble-averaged quantity, all the fluctuations are (in principle) incorporated into the free-energy functional. Adding noise to the EOM, a part of the fluctuations might be counted twice [104,200]. If in turn the number density is viewed as being coarse-grained in time, there is phenomenological motivation to add a noise term to the EOM [201]. The latter approach is appealing in several ways: crystal nucleation is feasible from a homogeneous state and capillary waves appear at the crystal-liquid interface. To investigate how nucleation and growth happen on the atomistic level, a conserved noise term is usually incorporated into the EOM [Equations (60)–(63)]. To overcome some difficulties occurring when discretizing the noise [202,203], coloured noise obtained by filtering out the unphysical short wavelengths smaller than the interparticle distance is often used (this removes both the ultraviolet catastrophe expected in 3D [238] and the associated dependence of the results on spatial resolution). The majority of the studies we review below follows this approach.

5.1.1. Nucleation in colloidal crystal aggregation

5.1.1.1 *Homogeneous nucleation. The effect of noise:* A systematic study of the effect of the noise strength on the grain size distribution performed in 2D by Hubert *et al.* [34] for the original 1M-PFC model implies that the grain size decreases with increasing noise amplitude, resulting in both a smaller average grain size and a reduced maximum grain size. They have distinguished two regimes regarding the cluster size distribution: for small noise amplitudes a bimodal cluster size distribution is observed, whereas for large noise amplitudes a monotonically decreasing distribution is reported.

Phase selection in 2D and 3D: Mounting evidence indicates that the classical picture of crystal nucleation, which considers heterophase fluctuations of only the stable phase, is oversimplified. Early analysis by Alexander and McTague suggests a preference for bcc freezing in simple liquids [239]. Atomistic simulations for the LJ system have verified that small heterophase fluctuations have the metastable bcc structure, and even larger clusters of the stable fcc structure have a bcc interface layer [240], while the ratio of the two phases can be tuned by changing the pressure [241]. Composite bcc-fcc nuclei have also been predicted by continuum models [242]. Two-stage nucleation has been reported in systems that have a metastable critical point in the undercooled liquid (including solutions of globular proteins [243]); the appearance of the crystalline phase is assisted by dense liquid droplets, whose formation precedes and helps crystal nucleation [244]. Recent studies indicate a similar behaviour in simple liquids such as the LJ [245] or hard-sphere (HS) [246] fluids, where a dense liquid or amorphous precursor assists crystal nucleation. Analogous behaviour has been reported for colloidal systems in 2D [247] and 3D [248]. These findings imply that the nucleation precursors are fairly common. The 1M-PFC model has bcc, fcc, and hcp stability domains [28], the appearance of an amorphous phase and two-step nucleation has also been reported [46], and the 2M-PFC model incorporates the 1M-PFC model [144]. Accordingly, this class of the dynamic PFC models is especially suitable for investigating phase selection during freezing of undercooled liquids.

In 2D, it has been shown within the framework of the 1M-PFC model that at relatively small supersaturations direct crystal nucleation takes place. Increasing the thermodynamic driving force, first copious crystal nucleation is observed, and at higher driving forces an amorphous precursor precedes crystalline nucleation [33] (Figures 38 and 39(a)). Similarly to quenching experiments for two-dimensional colloidal systems [249], no hexatic phase is observed in the 1M-PFC quenching

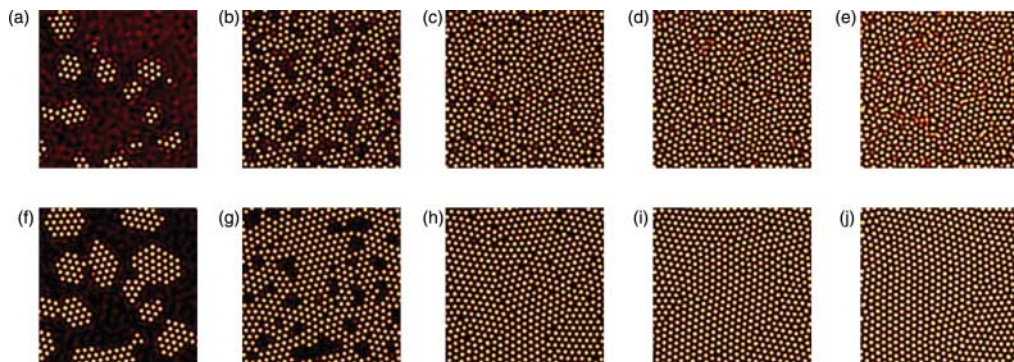


Figure 38. Snapshots of early and late stages of isothermal solidification in 1M-PFC quenching simulations performed in 2D with initial reduced particle densities of $\psi_0 = -0.55, -0.50, -0.45, -0.40$ and -0.35 [33]. (a)–(e): Early stage: the respective reduced times are $\tau/\Delta\tau = 10,000, 3000, 1500, 1000,$ and 700 . (f)–(j): Late stage: the same fractions are shown at reduced time $\tau/\Delta\tau = 60,000$. Reduced particle density maps in 418×418 sized fractions of 2048×2048 sized simulations are shown. Other simulation parameters were $\epsilon = 0.75$ and $\alpha = 0.1$ (noise strength). (Reproduced from Gránásy *et al.* [33] © 2011 by Taylor & Francis.)

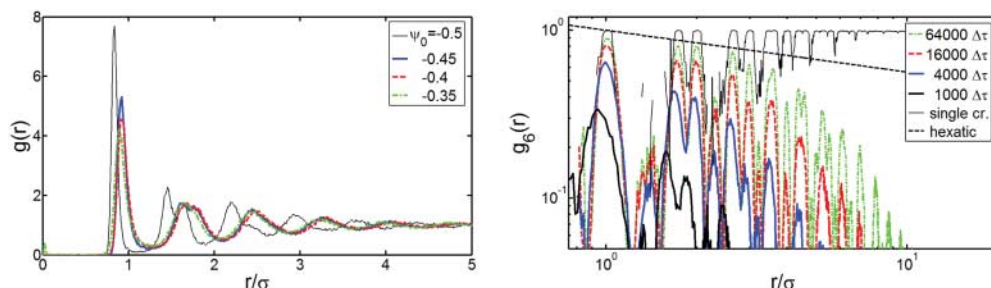


Figure 39. Structural properties evolving after quenching in 1M-PFC simulations [33]: (a) pair-correlation function $g(r)$ for the early-stage solidification structures shown in Figure 20(b)–(e). (b) Time evolution of the bond-order correlation function $g_6(r)$ for $\psi_0 = -0.4$ on log–log scale. $g_6(r)$ is shown at $\tau/\Delta\tau = 1000, 4000, 16,000,$ and $64,000$. For comparison, the upper envelope expected for the hexatic phase and the result for a single crystal are also shown. These curves describe an amorphous to polycrystalline transition (Figure 20(d) and (i)). Note that the upper envelope of the $g_6(r)$ curves decay faster than expected for the hexatic phase. (Reproduced from Gránásy *et al.* [33] © 2011 by Taylor & Francis.)

simulations [33,38] [as demonstrated by the form of the radial decay of the bond-order correlation function [33], see Figure 39(b)].

In 3D, a systematic dynamic study of the 1M/2M-PFC models by Tóth *et al.* [35] shows that in these systems the first appearing solid is amorphous, which promotes the nucleation of bcc crystals (Figure 40) but suppresses the appearance of the fcc and hcp phases. The amorphous phase appears to coexist with the liquid indicating a first-order phase transition between these phases in agreement with the observed nucleation of the amorphous state. Independent ELE studies determining the height of the nucleation barrier have confirmed that density and structural changes take place on different times scales [35]. This finding suggests that the two time scales are probably present independently of the type of dynamics assumed. These findings have been associated with features of the effective interaction potential deduced from the amorphous structure using Schommers’ iterative method [250] that shows a maximum at $r_0\sqrt{2}$, where r_0 is the radius corresponding to the main minimum of the potential. Such a maximum in the interaction potential is expected to

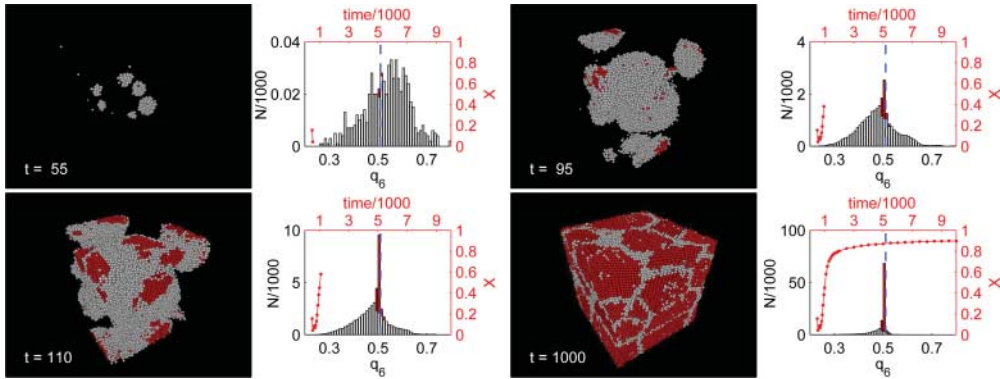


Figure 40. Two-step nucleation in the 1M-PFC model at $\psi_0 = -0.1667$ and $\epsilon = 0.25$ [35]. Four pairs of panels are shown, where t indicates the time elapsed, N is the total number of particles, and q_i is the bond orientational order parameter with index i . Left: snapshots of the density distribution taken at the dimensionless times $\tau = 57.74t$. Spheres of the diameter of the interparticle distance centred on density peaks higher than a threshold ($= 0.15$) are shown. They are coloured dark grey (red online) if $q_4 \in [0.02; 0.07]$ and $q_6 \in [0.48; 0.52]$ (bcc-like) and light grey otherwise. Right: population distribution of q_6 (histogram painted similarly) and the time dependence of the fraction X of bcc-like neighbourhoods (solid line). (Reproduced from Tóth *et al.* [35] © 2011 by the American Physical Society.)

suppress crystallization to the close-packed structures fcc and hcp [251], whereas the multiple minima also found are expected to lead to coexisting disordered structures [252]. By combining the results available for various potentials (LJ [245], HS [246], and the PFC potentials [28,35]), it appears that a repulsive core suffices for the appearance of a disordered precursor, whereas the peak at $r_0\sqrt{2}$ correlates with the observed suppression of fcc and hcp structures, while the coexistence of the liquid and amorphous phases seen here can be associated with multiple minima of the interaction potential.

3D studies, performed for bcc crystal nucleation in molten pure Fe in the framework of the EOF-PFC model [28,33], lead to similar results, however, still with diffusive dynamics. In these simulations, the initial density of the liquid has been increased until the solidification started – a procedure that has led to an extreme compression owing to the small size and short time accessible for the simulations. While this raises some doubts regarding the validity of the applied approximations, the behaviour observed for the EOF-PFC Fe is fully consistent with the results obtained for the 1M-PFC model: with increasing driving force first an amorphous precursor nucleates and the bcc phase appears inside these amorphous regions [28,33]. At higher driving forces the amorphous precursor appears nearly homogeneously in space and the bcc phase nucleates into it later. Apparently, direct nucleation of the bcc phase from the liquid phase requires a longer time than via the amorphous precursor, suggesting that the appearance of the bcc phase is assisted by the presence of the amorphous phase and in line with recent predictions by DFT [245] and atomistic simulations [246]. Remarkably, the interaction potential evaluated for Fe from the pair-correlation function of the amorphous structure is oscillatory and is qualitatively similar to the ones evaluated from experimental liquid structures [253].

5.1.1.2 Heterogeneous nucleation. Prieler *et al.* [148] have explored crystal nucleation on an unstructured hard wall in an anisotropic version of the 1M-PFC model, in which the particles are assumed to have an ellipsoidal shape. In particular, they have investigated how the contact angle depends on the orientation of the ellipsoids and the strength of the wall potential (Figure 41).

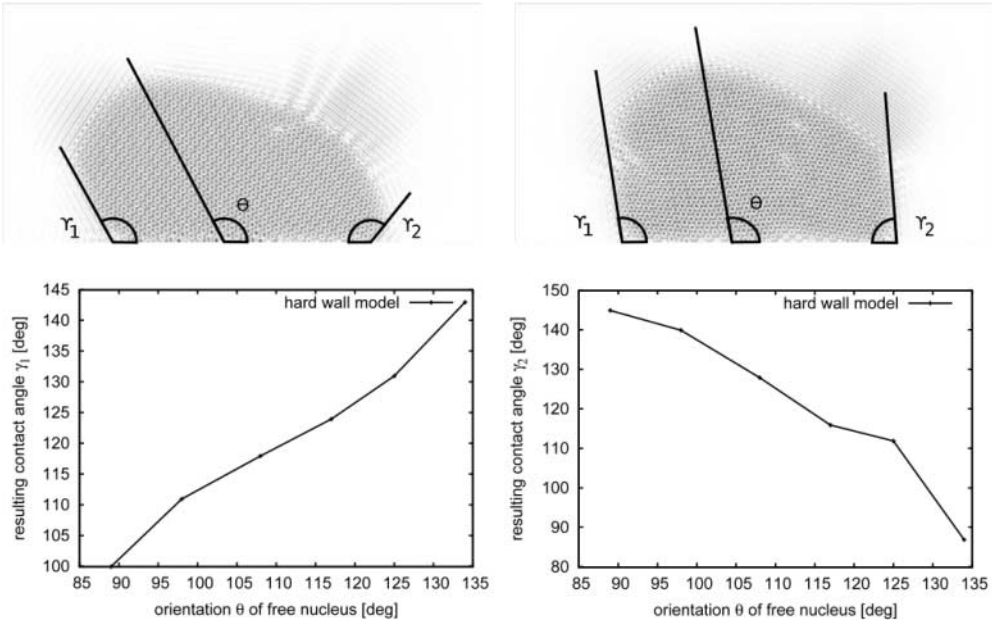


Figure 41. Heterogeneous nuclei formed on a hard wall in the APFC model proposed in reference [148] and the dependence of the left and right side contact angle (γ_1 and γ_2 , respectively) on the crystal orientation. (Reproduced from Prieler *et al.* [148] © 2009 by Institute of Physics Publishing.)

A complex behaviour has been observed for the orientational dependence, while increasing the strength of the wall potential reduced the contact angle.

Gránásy *et al.* [147] have studied crystal nucleation in an rectangular corner of structured and unstructured substrates within the 1M-PFC model in 2D. Despite expectations based on the classical theory of heterogeneous nucleation and conventional PF simulations [254], which predict that a corner should be a preferred nucleation site, in the atomistic approach such a corner is not a preferable site for the nucleation of the triangular crystal structure (Figure 42) owing to the misfit of the triangular crystal structure with a rectangular corner. Crystals of different orientation nucleate on the two substrate surfaces, which inevitably leads to the formation of a grain boundary starting from the corner when the two orientations meet. The energy cost of forming the grain boundary

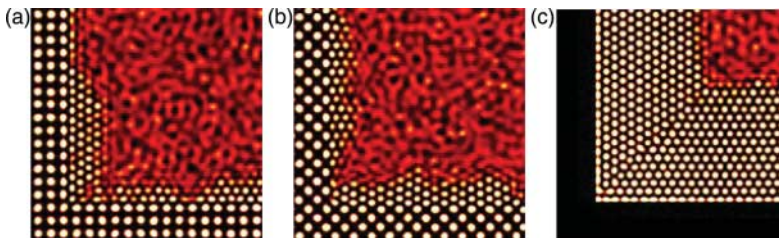


Figure 42. Heterogeneous nucleation in rectangular inner corners of the 1M-PFC model in 2D [33]. (a) Nucleation on (01) surfaces of a square lattice (ratio of lattice constant of substrate to interparticle distance $a_0/\sigma \approx 1.39$). (b) Nucleation on (11) surfaces of a square lattice. (c) Nucleation on an unstructured substrate. Note the frustration at the corner and the formation of a grain boundary starting from the corner at later stages. (Reproduced from Gránásy *et al.* [33] © 2011 by Taylor & Francis.)

makes the rectangular corner an unfavoured place for nucleation. In contrast, a 60° corner helps the nucleation of the triangular phase.

5.1.2. Pattern formation in colloidal crystal aggregation

5.1.2.1 Colloid patterns in two dimensions. Using a large value for the parameter ϵ leading to a faceted liquid-solid interface, Tegze *et al.* [38,39] have investigated solidification morphologies as a function of the thermodynamic driving force. They have found that the diffusion-controlled growth mode appearing at low driving forces and yielding faceted interfaces changes to a diffusionless growth mode characterized by a diffuse liquid-solid interface, which in turn produces a crystal, whose density is comparable to the density of the liquid due to the quenched-in vacancies (Section 4.3.5). It is worth noting that similar growth modes have been observed experimentally in colloidal systems [255]. Tegze *et al.* have shown [38,39] that the diffusion-controlled and diffusionless modes can coexist along the perimeter of the same crystal and lead to a new branching mechanism that differs from the usual diffusional-instability-driven branching by which dendritic structures form. This new mechanism explains the fractal-like and porous growth morphologies [256] observed in 2D colloidal systems (Figure 43) and may be relevant for the diffusion-controlled to diffusionless transition of crystallization in organic glasses [71].

5.1.2.2 Colloid patterns in three dimensions. Tóth *et al.* [28] have demonstrated first that owing to the conservative dynamics, the EOM of the 1M-PFC model realizes, dendritic growth forms of bcc and fcc structure evolve in the single-component theory. Tegze [29] and Gránásy *et al.* [257] have shown by simulations containing $\approx 3 \times 10^6$ particles that due to a kinetic roughening of the

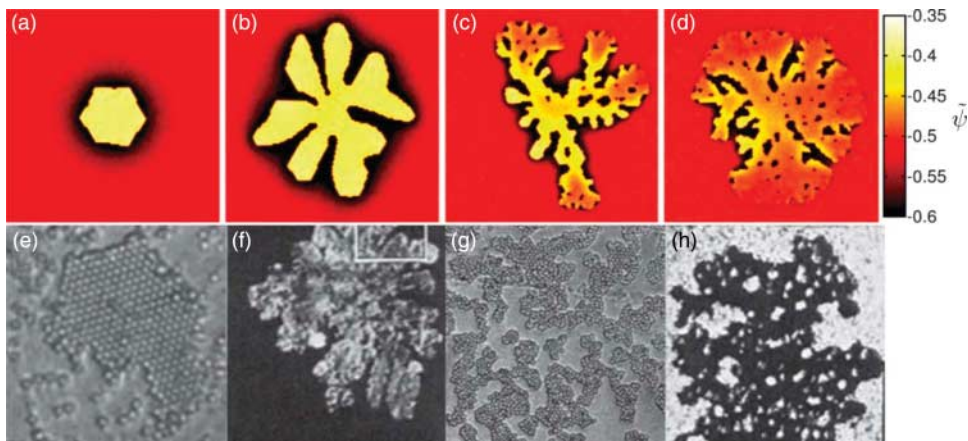


Figure 43. Single crystal growth morphologies (a)–(d) in the 1M-PFC model [38] (top) and experiment (bottom) (e)–(h): 2D colloid crystals by Skjeltorp. (Reproduced with permission from Skjeltorp [256] © 1987 by the American Physical Society.) The driving force increases from left to right. In the case of the simulations, the coarse-grained particle density map is shown. The fractal dimensions of the single crystal aggregates evaluated from the slope of the plot $\log(N)$ vs. $\log(R_g)$ (N is the number of particles in the cluster and R_g is its radius of gyration) are: (a) $f_d = 2.012 \pm 0.3\%$, (b) $1.967 \pm 0.3\%$, (c) $1.536 \pm 0.9\%$, (d) $1.895 \pm 0.3\%$. The fast growth mode is recognizable via the lack of a (dark) depletion zone at the interface, whose presence is indicative to the slow mode. A 2048×2048 rectangular grid corresponding to $\approx 13,000$ particles, or $118 \mu\text{m} \times 118 \mu\text{m}$ (assuming $1.1 \mu\text{m}$ particles) has been used – a size comparable to that shown by the experimental images. (Reproduced from G. Tegze *et al.* [38] © 2011 by Royal Society of Chemistry Publishing.)

crystal-liquid interface that leads to interface broadening, a transition can be seen from faceted dendrites to compact rounded crystals (Figure 44) – a phenomenon reported earlier in experiments for dendritic growth of NH_4Br crystals [258]. Note that such a kinetic effect cannot be easily incorporated into conventional PF models. Remarkably, as pointed out in reference [28], assuming a micrometer diameter for the “atoms”, these dendritic structures are comparable in size to those formed in colloid experiments in microgravity [259]. This is a unique situation indeed: an “atomistic” theory works here on the size scale of experimental dendrites.

In a recent work, Tang *et al.* [30] have performed a geometric analysis of bcc and fcc dendrites grown in the respective stability domains of the 1M-PFC model, and evaluated dynamic exponents characterizing dendritic growth in the (100), (110), and (111) directions. They associate the

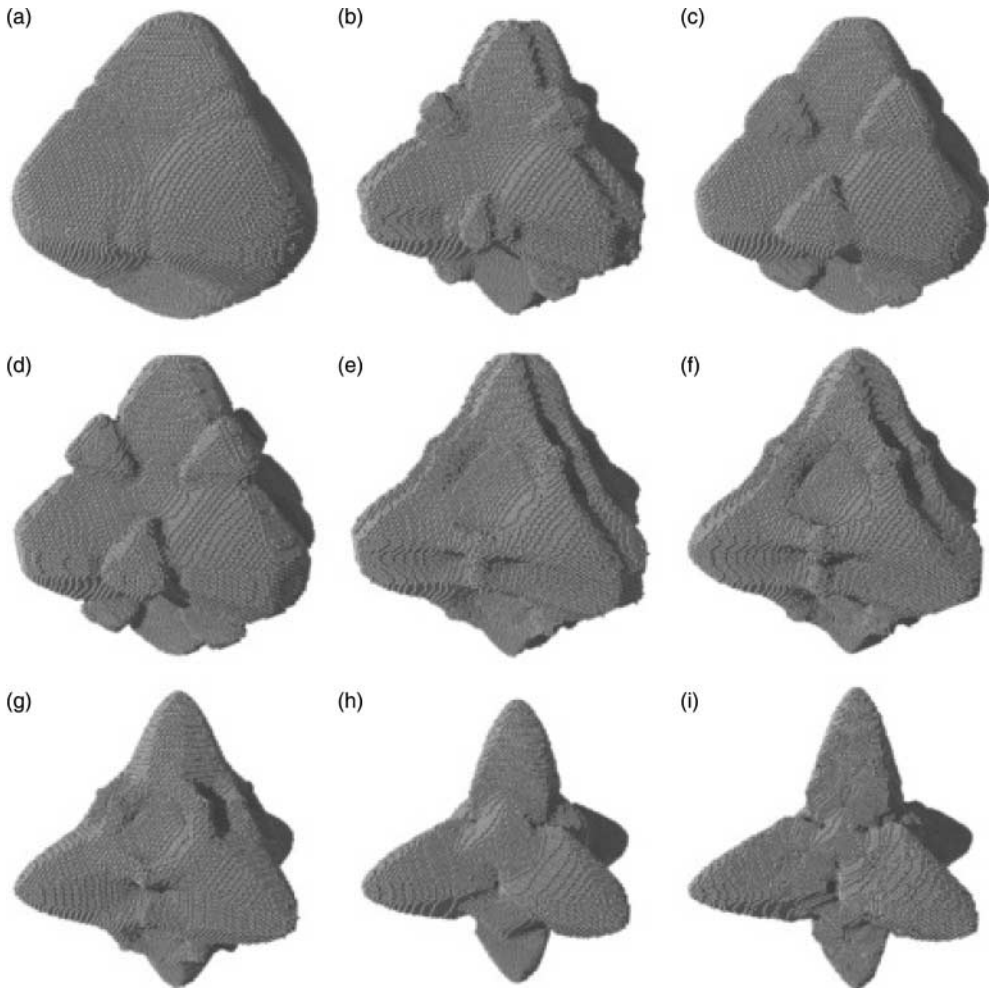


Figure 44. 3D crystal growth morphologies grown from a bcc seed in the single-component 1M-PFC model at $\epsilon = 0.3748$ in a system containing about 3×10^6 colloidal particles [29]. The initial fluid density decreases as (a) $\psi_0 = -0.015$, (b) -0.0175 , (c) -0.01875 , (d) -0.02 , (e) -0.02062 , (f) -0.0225 , (g) -0.025 , (h) -0.03 , (i) -0.0325 . The simulations have been performed on a $1024 \times 1024 \times 1024$ grid. Assuming $1 \mu\text{m}$ diameter for the particles, the linear size of the simulation box is $\approx 0.16 \text{ mm}$ – comparable to the smaller colloidal dendrites seen in microgravity experiments [259]. (Reproduced from Tegze [29]).

relatively large values obtained for the stability constant from the geometry of the dendrite tip with the faceted morphology of the crystals.

5.1.3. Colloid patterning

Colloid patterning under the influence of periodic substrates can be realized via creating patches that are chemically attractive to the colloidal particles [260]. Depending on the size of the patches single, double, triple, etc., occupations of the patches are possible (Figure 45), whereas the distance of the patches may lead to the formation of various ordered patterns, as predicted by Langevin simulations, in which the patterned substrate is represented by appropriate periodic potentials [261]. Gránásy *et al.* [33] has employed a 1M-PFC model supplemented with a periodic potential of circular potential wells arranged on a square lattice, to reproduce the patterns seen in the experiments (Figure 45). Another problem, exemplifying the abilities of PFC simulations in modelling colloid patterning, is colloidal self-assembly under the effect of capillary-immersion forces acting on the colloid particles in thin liquid layers due to capillarity and a periodically varying depth of the liquid layer due to a wavy substrate surface. Experiments of this kind have been used to produce single and double particle chains [262] and the otherwise unfavourable square-lattice structure [263]. The capillary-immersion forces can often be well represented by a potential of the form $U = u_1 \cos(kx)$, where u_1 is a constant, $k = 2\pi/\lambda$, and λ the wavelength of the periodic potential. Setting $\lambda = \sigma/\sqrt{2}$, where σ is the interparticle distance, and varying the orientation of the grooves relative to the crystallization (drying) front, patterns seen in the experiments [263] are observed to form in the 1M-PFC model: for grooves parallel to the front, a frustrated triangular structure of randomly alternating double and triple layers appears. For grooves perpendicular to the front, the particles align themselves on a square lattice with the (11) orientation lying in the interface, while for a $\pi/4$ declination of the grooves the same structure forms, however, now with the (10) face lying in the front. Using larger wavelengths for the potential and adding a weak transversal modulation, while starting from a homogeneous initial particle density, nucleation and growth of wavy single and double chains resembling closely to the experiments [262] are seen [33] (Figure 46).

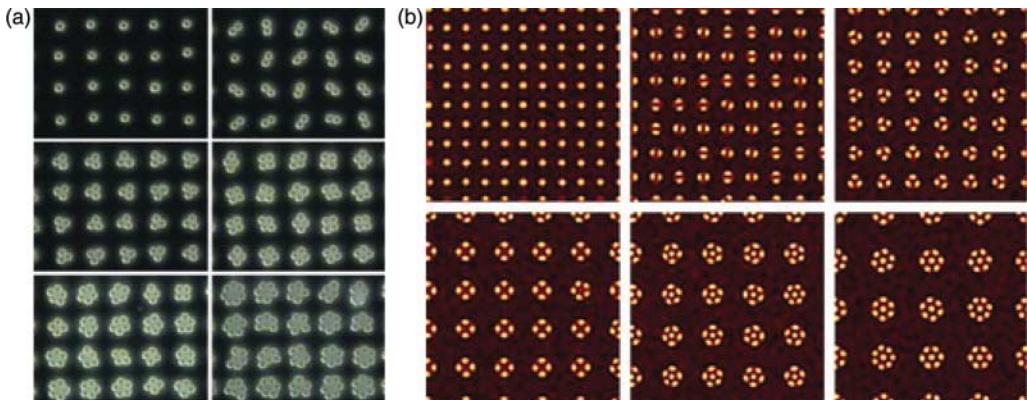


Figure 45. (a) Single and multiple occupation of a chemically patterned periodic substrate by colloidal particles as a function of increasing patch size in the experiments. (Reproduced with permission from Lee *et al.* [260] © 2002 by Wiley.) (b) 1M-PFC simulations [33] with increasing diameter of circular attractive potential wells. Reduced particle density maps are shown. The ratio of the potential well diameters relative to the single occupation case has been 1, 1.25, 1.5, 2, 2.13, and 2.5. (Reproduced from L. Gránásy *et al.* [33] © 2011 by Taylor & Francis.)

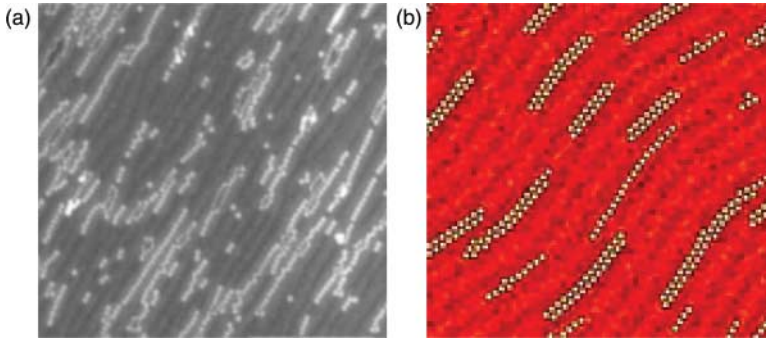


Figure 46. Patterning in experiment vs. 1M-PFC simulation: (a) single and double particle chains evolving in experiment due to capillary-immersion forces on the surface of a rippled substrate. (Reproduced with permission from Mathur *et al.* [262] © 2006 by the American Chemical Society.) (b) The particle chains forming in the 1M-PFC simulation performed with a tilted and wavy version of the potential described in the text [33]. Only a fraction of the reduced particle density map is shown. (Reproduced from Gránásy *et al.* [33] © 2011 by Taylor & Francis.)

Epitaxial growth on the (100) surface of a sc substrate has been investigated in 3D using the 1M-PFC model by Tegze *et al.* [42]. The lattice constant a_s of the substrate has been varied in a range that incorporates the interatomic distance of the bulk fcc structure and the lattice constant of the bulk bcc phase, where the (100) face of the sc structure is commensurable with the (100) faces of the bulk fcc and bcc structures, respectively. A bct structure has grown, whose axial ratio c/a varies continuously with the lattice constant of the substrate, where c and a are the lattice constants of the bct structure perpendicular and parallel to the surface of the substrate, respectively. At the matching values of a_s , fcc and bcc structures have been observed respectively, as observed in colloid patterning experiments [264]. Analogous results have been obtained for the (100) face of an fcc substrate using 1M-PFC simulations, however, for large lattice mismatch amorphous phase mediated bcc nucleation has been seen [151].

Optical tweezers are used widely to realize 2D periodic templates for influencing colloidal crystal aggregation in 3D [265]. Such templates, depending on the mismatch to the crystalline structure evolving, may instigate the formation of single-crystal or polycrystalline structures [266]. Growth textures, obtained when supplementing the 1M-PFC model with a 5×5 flat square-lattice template (realized by a periodic potential term), show remarkable resemblance to the experiments (Figure 47) [267].

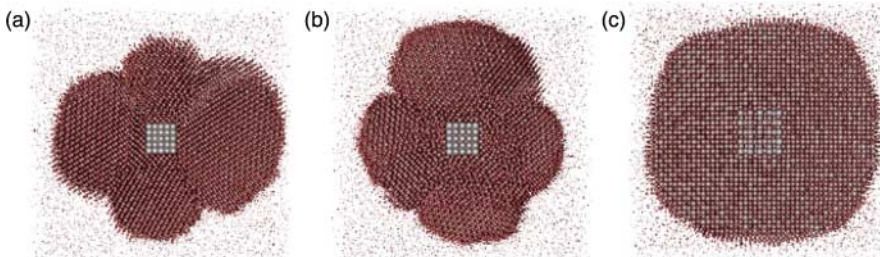


Figure 47. In-plane snapshot of crystalline aggregates grown on 5×5 square-lattice templates of $a_s/\sigma_{\text{fcc}} = 1.0, 1.1547, \text{ and } 1.56$ in 3D as predicted by 1M-PFC simulations [266]. Here, $\sigma_{\text{fcc}} = 1.056$. A $256 \times 256 \times 128$ grid has been used. The visualization is as in Figure 25.

5.2. Application to liquid crystals

The different forms of PFC models for orientable particles as discussed in Section 3.1.3 can be applied to compute liquid crystalline systems under various circumstances. First of all, the two-dimensional bulk calculations presented in Section 3.2.2 clearly need to be extended to 3D. Moreover, a huge application area is found for confined systems. For instance, boundary conditions to the director fields set by external walls can lead to forced topological defects of the orientational order [268]. Here, PFC models for liquid crystals provide a flexible tool to access those numerically. Next, liquid crystalline droplets in air or vacuum provide another type of confinement which induces quite peculiar orientational fields (so-called tactoids [269] or smectic droplets [269]) and again the PFC approach would provide a microscopic avenue to approach those. It would further be interesting to generalize the PFC model on curved surfaces in order to explore the structure of thin liquid crystalline bubbles, see, for example, references [270,271] for simulation predictions. Last not least the structure of interfaces between two coexisting liquid crystalline phases needs future attention, in particular for phases with positional order.

A further broad range of applications have to do with dynamics. One recent example was performed in reference [171], where the CMA was employed to compute the dynamic coarsening of a disturbed nematic phase. The time evolution of such a nematic phase is shown in the Schlieren patterns in Figure 48.

More applications concern the dynamics of topological defects, nucleation in liquid crystalline systems [272], and the orientational dynamics induced by external switching fields [273]. Hence a flourishing future of many more PFC computations for liquid crystals is still lying ahead.

6. Summary and outlook

Motivated by the spectacular advances phase-field-crystal modelling has made in recent years, we have reviewed its present status. Besides presenting the original PFC model together with its

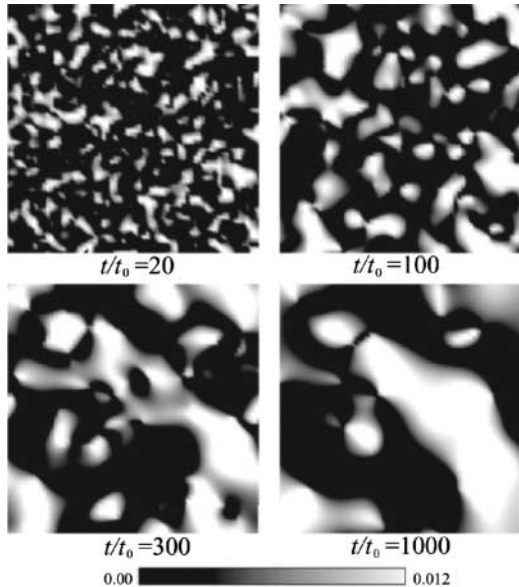


Figure 48. Time evolution of the Schlieren pattern $\propto Q_{12}^2$ in the x_1 - x_2 -plane, which exhibits a dynamical coarsening. The symbol t_0 denotes a characteristic time. (Reproduced with permission from Yabunaka and Araki [171] © 2011 by the American Physical Society.)

derivation from DDFT, we have reviewed many of its numerous extensions, including those aimed at describing binary solidification, vacancy transport (VPFC), anisotropic molecules (APFC), liquid crystals, and a quantitative description of real systems. We have reviewed, furthermore, a broad range of applications for metallic and soft matter systems (colloids and liquid crystals), and for phenomena like the glass transition, and the formation of foams. We have discussed open issues such as coupling to hydrodynamics and the possibility of making quantitative PFC predictions for real materials. The main question at present is what further steps need yet to be made to turn the PFC-type models into even more potent modelling tools.

To summarize the present state of affairs, it seems appropriate to recall some of the concluding remarks of a Centre Européen de Calcul Atomique et Moléculaire (CECAM) workshop dedicated to DDFT- and PFC-type approaches held in 2009 in Lausanne [202]. It appears that despite the advances made meantime, some of the major issues identified there need yet further attendance. These are the following:

(i) *How to build numerically efficient, quantitative PFC models for a broad spectrum of metallic materials?* The PFC models incorporate microscopic physics in a phenomenological manner. The respective local free-energy functional and the simplified dynamics lead to equations of motion that can be handled fairly efficiently with advanced numerical methods so that simulations containing up to a few times 10^7 particles/atoms can be performed with relative ease. A major aim here is to develop a methodology for tuning crystal symmetry, lattice spacing, elastic constants, surface energy, dislocation core energy, dislocation mobility, etc. without sacrificing numerical efficiency. Along this line, methods have been proposed for constructing PFC free energies that allow for the tuning of the crystal structure [144,146,147]. The amplitude equations represent an appealing alternative [19,31,141,181], in which the density field is expressed in terms of slowly-varying amplitudes, modulated by the fundamental spatial periodicity of particle density. As demonstrated, this approach realizes a truly multi-scale approach to phase transitions in freezing liquids [20]. Alternatively, one can work directly with the scaled density field of the PFC models and introduce additional model parameters, which can be fitted so that a required set of physical properties is recovered, as done in the case of pure bcc Fe [142].

(ii) *How to construct effective, low-frequency representations from DFT/DDFT?* Provided that one had an accurate and predictive density functional that incorporates *interaction potentials* between the constituent species in a multi-component system, it would become possible to develop an effective description that enables quantitative simulations for microscopically-informed continuum systems that evolve on diffusive time scales. However, one needs to develop first such free-energy functionals. Next, the dynamics of the relevant degrees of freedom should be projected out from the full DDFT description. It may be expected on physical grounds that the shape of a single density peak would relax much faster than the distance between different peak centres. Accordingly, one could “slave” the high-frequency modes associated with the peak shapes to the more slowly evolving modes with low spatial frequencies.

(iii) *The role of fluctuations in DDFT and PFC modelling.* There is a continuing debate about the role of noise in the DDFT- and PFC-type models [201]. Derivations of DDFT from either the Smoluchowski level [106] or within the projection operator technique [83] lead to a deterministic EOM without any noise an approximation that becomes problematic near the critical point, or during nucleation, where the system has to leave a metastable free-energy minimum. In the former case fluctuations are needed to obtain the correct critical behaviour, whereas in the latter case, fluctuations are needed to establish an escape route of the system from a metastable phase. Other approaches treat fluctuations on a more phenomenological level. Often, however, the noise strength, though fundamentally correlated with the thermal energy, is treated as a phenomenological fitting parameter [34,57]. This is a fundamental problem, shared by all DDFT and PFC approaches. We note that the addition of noise to the EOM in continuum models is not without

conceptual difficulties [203], even if noise is discretized properly during numerical solution. For example, in the presence of noise, the equilibrium properties of the system change. Furthermore, transformation kinetics generally depends on the spatial and temporal steps and in the limit of infinitely small steps in 3D the free energy of the PFC systems diverges, leading to an ultraviolet “catastrophe”. Evidently, an appropriate “ultraviolet cutoff”, that is, filtering out the highest frequencies, is required to regularize the unphysical singularity. Here, a straightforward choice for the cut-off length is the interparticle/interatomic distance, which then removes the unphysical, small wavelength fluctuations [27,28,42,177]. A more elegant handling of the problem is via renormalizing the model parameters so that with noise one recovers the “bare” physical properties (as outlined for the SH model in reference [205]). Further systematic investigations are yet needed to settle this issue.

Acknowledgements

This work has been supported by the EU FP7 Projects “ENSEMBLE” (contract no. NMP4-SL-2008-213669) and “EXOMET” (contract no. NMP-LA-2012-280421, co-funded by ESA), by the ESA MAP/PECS project “MAGNEPHAS III”, and by the German Research Foundation (DFG) in the context of the DFG Priority Program 1296.

Notes

1. It is interesting to note that there are also mesoscopic particle systems with Newtonian dynamics, which are virtually undamped. These are realized in the so-called complex plasmas [75,76], where dust particles are dispersed and levitated in a plasma.
2. This follows from the representation (9) under consideration of the translational and rotational symmetries of the isotropic bulk fluid that also apply to the direct correlation function $c^{(1)}(\mathbf{r}_1) = \text{const.}$
3. More refined approaches include also the third-order term [115] with an approximate triplet direct correlation function [116,117].
4. However, one should also note that density fluctuations, which are, for example, embodied in the liquid structure factor, are not reproduced by Equation (33), since the one-particle density is the only variable here.
5. Note that the order-parameter field $\psi(\mathbf{r})$ introduced here is not identical with the field $\tilde{\psi}(\tilde{\mathbf{r}})$ in Equation (1), although both fields are dimensionless.
6. This Taylor approximation of the logarithm has the serious consequence that the non-negative-density constraint $\rho(\mathbf{r}) \geq 0$ gets lost in the PFC model.
7. A recent comparison between DFT and PFC models for the structure of the hard-sphere crystal-fluid interface was performed in reference [134].
8. To keep the notation simple, we ignore $\tilde{\mathcal{F}}$ and write \mathcal{F} instead of $\Delta\mathcal{F}$ throughout this article.
9. Turnbull’s coefficient C_T is a reduced liquid-solid interfacial free energy defined via the relationship $\gamma_{\text{ls}} = C_T(\Delta H_f / (N_A^{1/3} v_m^{2/3}))$, where γ_{ls} , ΔH_f , N_A , and v_m are the total liquid-solid interfacial free energy, the molar heat of fusion, the Avogadro number, and the molar volume, respectively. C_T is expected to depend only on the crystal structure. Recent results indicate that besides structure the interaction potential also has influence on its magnitude.

References

- [1] P.C. Hohenberg and B.I. Halperin, *Rev. Mod. Phys.* 49 (1977), pp. 435–479.
- [2] J.D. Gunton, M. San Miguel, and P.S. Sahní, *The dynamics of first order phase transitions*, in C. Domb and J. Lebowitz, eds., *Phase Transitions and Critical Phenomena*, 1st ed., Academic Press, London, 1983, pp. 267–466.
- [3] M.C. Cross and P.C. Hohenberg, *Rev. Mod. Phys.* 65 (1993), pp. 851–1112.

- [4] M. Seul and D. Andelman, *Science* 267 (1995), pp. 476–483.
- [5] P.M. Chaikin and T.C. Lubensky, *Principles of Condensed Matter Physics*, 1st ed., Cambridge University Press, Cambridge, 1995.
- [6] L.M. Pismen, *Patterns and Interfaces in Dissipative Dynamics*, 1st ed., Springer, Berlin, 2006.
- [7] M.C. Cross and H. Greenside, *Pattern Formation and Dynamics in Nonequilibrium Systems*, 1st ed., Cambridge University Press, Cambridge, 2010.
- [8] C. Klemenz, *J. Cryst. Growth* 187 (1998), pp. 221–227.
- [9] B. Vasiev, F. Siegert, and C. Weijer, *Phys. Rev. Lett.* 78 (1997), pp. 2489–2492.
- [10] J. Swift and P.C. Hohenberg, *Phys. Rev. A* 15 (1977), pp. 319–328.
- [11] S.A. Brazowskii, *Sov. Phys. JETP* 41 (1975), pp. 85–89.
- [12] K.R. Elder, M. Katakowski, M. Haataja, and M. Grant, *Phys. Rev. Lett.* 88 (2002), p. 245701.
- [13] D. Oxtoby, *Course 3: Crystallization of liquids: A density functional approach*, in *Proceedings of the Les Houches Summer School, Course LI, 3–28 July 1989*, J.P. Hansen, D. Levesque, and J. Zinn-Justin, eds., Vol. 1, North Holland, Elsevier Science Publishers B.V., Amsterdam, 1991, pp. 145–192.
- [14] Y. Singh, *Phys. Rep.* 207 (1991), pp. 351–444.
- [15] H. Löwen, *Phys. Rep.* 237 (1994), pp. 249–324.
- [16] Y. Rosenfeld, *Phys. Rev. Lett.* 63 (1989), pp. 980–983.
- [17] J.F. Lutsko, *Phys. Rev. E* 74 (2006), p. 021603.
- [18] A. Härtel, M. Oettel, R.E. Rozas, S.U. Egelhaaf, J. Horbach, and H. Löwen, *Phys. Rev. Lett.* 108 (2012), p. 226101.
- [19] N. Goldenfeld, B.P. Athreya, and J.A. Dantzig, *Phys. Rev. E* 72 (2005), p. 020601.
- [20] B.P. Athreya, N. Goldenfeld, J.A. Dantzig, M. Greenwood, and N. Provatas, *Phys. Rev. E* 76 (2007), p. 056706.
- [21] J.J. Hoyt, M. Asta, and A. Karma, *Mater. Sci. Eng. R* 41 (2003), pp. 121–163.
- [22] L. Gránásy, T. Pusztai, and J.A. Warren, *J. Phys.: Condens. Matter* 16 (2004), pp. R1205–R1235.
- [23] A. Karma, *Phase field modeling*, in *Handbook of Materials Modeling*, S. Yip, ed., Springer, Netherlands, 2005, pp. 2087–2103.
- [24] H. Emmerich, *Adv. Phys.* 57 (2008), pp. 1–87.
- [25] N. Provatas and K. Elder, *Phase-Field Methods in Materials Science and Engineering*, 1st ed., Wiley, Weinheim, 2010.
- [26] K.R. Elder, N. Provatas, J. Berry, P. Stefanovic, and M. Grant, *Phys. Rev. B* 75 (2007), p. 064107.
- [27] T. Pusztai, G. Tegze, G.I. Tóth, L. Környei, G. Bansel, Z. Fan, and L. Gránásy, *J. Phys.: Condens. Matter* 20 (2008), p. 404205.
- [28] G.I. Tóth, G. Tegze, T. Pusztai, G. Tóth, and L. Gránásy, *J. Phys.: Condens. Matter* 22 (2010), p. 364101.
- [29] G. Tegze, *Application of atomistic phase-field methods to complex solidification problems*, Ph.D. thesis, Eötvös University, Budapest, Hungary, 2009 (in Hungarian).
- [30] S. Tang, R. Backofen, J. Wang, Y. Zhou, A. Voigt, and Y. Yu, *J. Cryst. Growth* 334 (2011), pp. 146–152.
- [31] K.R. Elder, Z.F. Huang, and N. Provatas, *Phys. Rev. E* 81 (2010), p. 011602.
- [32] R. Backofen and A. Voigt, *J. Phys.: Condens. Matter* 22 (2010), p. 364104.
- [33] L. Gránásy, G. Tegze, G.I. Tóth, and T. Pusztai, *Philos. Mag.* 91 (2011), pp. 123–149.
- [34] J. Hubert, M. Cheng, and H. Emmerich, *J. Phys.: Condens. Matter* 21 (2009), p. 464108.
- [35] G.I. Tóth, T. Pusztai, G. Tegze, G. Tóth, and L. Gránásy, *Phys. Rev. Lett.* 107 (2011), p. 175702.
- [36] J. Berry, K.R. Elder, and M. Grant, *Phys. Rev. B* 77 (2008), p. 224114.
- [37] J. Mellenthin, A. Karma, and M. Plapp, *Phys. Rev. B* 78 (2008), p. 184110.
- [38] G. Tegze, L. Gránásy, G.I. Tóth, J.F. Douglas, and T. Pusztai, *Soft Matter* 7 (2011), pp. 1789–1799.
- [39] G. Tegze, G.I. Tóth, and L. Gránásy, *Phys. Rev. Lett.* 106 (2011), p. 195502.
- [40] K. Wu and A. Karma, *Phys. Rev. B* 76 (2007), p. 184107.
- [41] S. Majaniemi and N. Provatas, *Phys. Rev. E* 79 (2009), p. 011607.
- [42] G. Tegze, L. Gránásy, G.I. Tóth, F. Podmaniczky, A. Jaatinen, T. Ala-Nissila, and T. Pusztai, *Phys. Rev. Lett.* 103 (2009), p. 035702.
- [43] R. Backofen and A. Voigt, *J. Phys.: Condens. Matter* 21 (2009), p. 464109.

- [44] T. Pusztai, G.I. Tóth, G. Tegze, and L. Gránásy, *Dendritic growth: Phase field crystal vs. phase field simulations*, Abstract Booklet, TMS Annual Meeting, 26 February – 3 March 2011, The Minerals, Metals & Materials Society, San Diego, 2011, p. 31.
- [45] H. Humadi, J. Hoyt, and N. Provatas, *A phase field crystal study of rapid solidification and solute trapping in binary alloys*, Abstract Booklet, TMS Annual Meeting, 11–15 March 2012, The Minerals, Metals & Materials Society, Orlando, 2012.
- [46] J. Berry, K.R. Elder, and M. Grant, *Phys. Rev. E* 77 (2008), p. 061506.
- [47] J. Berry and M. Grant, *Phys. Rev. Lett.* 106 (2011), p. 175702.
- [48] S. Muralidharan and M. Haataja, *Phys. Rev. Lett.* 105 (2010), p. 126101.
- [49] K.R. Elder, G. Rossi, P. Kanerva, F. Sanches, S.C. Ying, E. Granato, C.V. Achim, and T. Ala-Nissila, *Phys. Rev. Lett.* 108 (2012), p. 226102.
- [50] S. Muralidharan, R. Khodadad, E. Sullivan, and M. Haataja, *Phys. Rev. B* 85 (2012), p. 245428.
- [51] Z.F. Huang and K.R. Elder, *Phys. Rev. Lett.* 101 (2008), p. 158701.
- [52] Z.F. Huang and K.R. Elder, *Phys. Rev. B* 81 (2010), p. 165421.
- [53] K.R. Elder and Z.F. Huang, *J. Phys.: Condens. Matter* 22 (2010), p. 364103.
- [54] J.A.P. Ramos, E. Granato, S.C. Ying, C.V. Achim, K.R. Elder, and T. Ala-Nissila, *Phys. Rev. E* 81 (2010), p. 011121.
- [55] C.V. Achim, M. Karttunen, K.R. Elder, E. Granato, T. Ala-Nissila, and S.C. Ying, *Phys. Rev. E* 74 (2006), p. 021104.
- [56] C.V. Achim, J.A.P. Ramos, M. Karttunen, K.R. Elder, E. Granato, T. Ala-Nissila, and S.C. Ying, *Phys. Rev. E* 79 (2009), p. 011606.
- [57] J.A.P. Ramos, E. Granato, C.V. Achim, S.C. Ying, K.R. Elder, and T. Ala-Nissila, *Phys. Rev. E* 78 (2008), p. 031109.
- [58] J. Rottler, M. Greenwood, and B. Ziebarth, *J. Phys.: Condens. Matter* 24 (2012), p. 135002.
- [59] K.R. Elder and M. Grant, *Phys. Rev. E* 70 (2004), p. 051605.
- [60] J. Berry, M. Grant, and K.R. Elder, *Phys. Rev. E* 73 (2006), p. 031609.
- [61] P. Stefanovic, M. Haataja, and N. Provatas, *Phys. Rev. Lett.* 96 (2006), p. 225504.
- [62] P.Y. Chan, G. Tsekenis, J. Dantzig, K.A. Dahmen, and N. Goldenfeld, *Phys. Rev. Lett.* 105 (2010), p. 015502.
- [63] R. Spatschek and A. Karma, *Phys. Rev. B* 81 (2010), p. 214201.
- [64] K.R. Elder, K. Thornton, and J.J. Hoyt, *Philos. Mag.* 91 (2011), pp. 151–164.
- [65] P.Y. Chan, N. Goldenfeld, and J. Dantzig, *Phys. Rev. E* 79 (2009), p. 035701R.
- [66] S. Aland, J. Lowengrub, and A. Voigt, *Phys. Fluids* 23 (2011), p. 062103.
- [67] H. Löwen, *J. Phys.: Condens. Matter* 22 (2010), p. 364105.
- [68] R. Wittkowski, H. Löwen, and H.R. Brand, *Phys. Rev. E* 82 (2010), p. 031708.
- [69] C.V. Achim, R. Wittkowski, and H. Löwen, *Phys. Rev. E* 83 (2011), p. 061712.
- [70] N. Guttenberg, N. Goldenfeld, and J. Dantzig, *Phys. Rev. E* 81 (2010), p. 065301.
- [71] H. Emmerich, L. Gránásy, and H. Löwen, *Eur. Phys. J. Plus* 126 (2011), pp. 102/1–102/18.
- [72] J.P. Hansen and H. Löwen, *Ann. Rev. Phys. Chem.* 51 (2000), pp. 209–242.
- [73] A. Einstein, *Ann. Phys. (Leipzig)* 322 (1905), pp. 549–560.
- [74] E. Frey and K. Kroy, *Ann. Phys. (Leipzig)* 517 (2005), pp. 20–50.
- [75] G.E. Morfill and A.V. Ivlev, *Rev. Mod. Phys.* 81 (2009), pp. 1353–1404.
- [76] G.E. Morfill, A.V. Ivlev, P. Brandt, and H. Löwen, *Interdisciplinary research with complex plasmas*, in G. Bertin, F. de Luca, G. Lodato, R. Pozzoli, and M. Romé, eds., *Plasmas in the Laboratory and the Universe: Interactions, Patterns, and Turbulence*, American Institute of Physics, AIP Press, Melville, 2010, pp. 67–79.
- [77] P.N. Pusey, *Course 10: Colloidal suspensions*, in *Proceedings of the Les Houches Summer School, Course LI, 3–28 July 1989*, J.P. Hansen, D. Levesque, and J. Zinn-Justin, eds., Vol. 2, North Holland, Elsevier Science Publishers B.V., Amsterdam, 1991, pp. 763–942.
- [78] R. Evans, *Adv. Phys.* 28 (1979), pp. 143–200.
- [79] S. van Teeffelen, R. Backofen, A. Voigt, and H. Löwen, *Phys. Rev. E* 79 (2009), p. 051404.
- [80] J.K.G. Dhont, *An Introduction to Dynamics of Colloids*, 1st ed., Elsevier, Amsterdam, 1996.

- [81] M. Doi and S.F. Edwards, *The Theory of Polymer Dynamics*, 1st ed., Oxford University Press, Oxford, 2007.
- [82] H. Risken, *The Fokker-Planck Equation: Methods of Solution and Applications*, 3rd ed., Springer, Berlin, 1996.
- [83] P. Español and H. Löwen, *J. Chem. Phys.* 131 (2009), p. 244101.
- [84] A.J. Archer, *J. Phys.: Condens. Matter* 18 (2006), pp. 5617–5628.
- [85] A.J. Archer, *J. Chem. Phys.* 130 (2009), p. 014509.
- [86] U.M.B. Marconi and S. Melchionna, *J. Phys.: Condens. Matter* 22 (2010), p. 364110.
- [87] U.M.B. Marconi, P. Tarazona, F. Cecconi, and S. Melchionna, *J. Phys.: Condens. Matter* 20 (2008), p. 494233.
- [88] R. Roth, *J. Phys.: Condens. Matter* 22 (2010), p. 063102.
- [89] R. Roth, R. Evans, A. Lang, and G. Kahl, *J. Phys.: Condens. Matter* 14 (2002), pp. 12063–12078.
- [90] H. Graf and H. Löwen, *J. Phys.: Condens. Matter* 11 (1999), pp. 1435–1452.
- [91] H. Hansen-Goos and K. Mecke, *Phys. Rev. Lett.* 102 (2009), p. 018302.
- [92] H. Löwen, *Applications of density functional theory in soft condensed matter*, Understanding soft condensed matter via modeling and computation, World Scientific Publishing, Singapore, 2010, pp. 9–45.
- [93] A. Poniewierski and R. Hołyst, *Phys. Rev. Lett.* 61 (1988), pp. 2461–2464.
- [94] T.V. Ramakrishnan and M. Yussouff, *Phys. Rev. B* 19 (1979), pp. 2775–2794.
- [95] Y. Rosenfeld, M. Schmidt, H. Löwen, and P. Tarazona, *Phys. Rev. E* 55 (1997), pp. 4245–4263.
- [96] W.A. Curtin and N.W. Ashcroft, *Phys. Rev. Lett.* 56 (1986), pp. 2775–2778.
- [97] R. Ohnesorge, H. Löwen, and H. Wagner, *Phys. Rev. A* 43 (1991), pp. 2870–2878.
- [98] R. Ohnesorge, H. Löwen, and H. Wagner, *Europhys. Lett.* 22 (1993), pp. 245–249.
- [99] R. Ohnesorge, H. Löwen, and H. Wagner, *Phys. Rev. E* 50 (1994), pp. 4801–4809.
- [100] R. Evans, Density functionals in the theory of nonuniform fluids, in *Fundamentals of Inhomogeneous Fluids*, 1st ed., Marcel Dekker, New York, 1992, pp. 85–176.
- [101] J.P. Hansen and I.R. McDonald, *Theory of Simple Liquids*, 3rd ed., Elsevier Academic Press, Amsterdam, 2006.
- [102] V.I. Kalikmanov, *Statistical Physics of Fluids: Basic Concepts and Applications*, 2nd ed., Springer, Berlin, 2010.
- [103] H. Löwen, *J. Phys.: Condens. Matter* 14 (2002), pp. 11897–11905.
- [104] U.M.B. Marconi and P. Tarazona, *J. Chem. Phys.* 110 (1999), pp. 8032–8044.
- [105] U.M.B. Marconi and P. Tarazona, *J. Phys.: Condens. Matter* 12 (2000), pp. 413–418.
- [106] A.J. Archer and R. Evans, *J. Chem. Phys.* 121 (2004), pp. 4246–4254.
- [107] A.J. Archer, *J. Phys.: Condens. Matter* 17 (2005), pp. 1405–1427.
- [108] H.H. Wensink and H. Löwen, *Phys. Rev. E* 78 (2008), p. 031409.
- [109] M. Rex and H. Löwen, *Phys. Rev. Lett.* 101 (2008), p. 148302.
- [110] M. Rex and H. Löwen, 28 (2009), pp. 139–146.
- [111] M. Rauscher, *J. Phys.: Condens. Matter* 22 (2010), p. J4109.
- [112] M. Rex, H.H. Wensink, and H. Löwen, *Phys. Rev. E* 76 (2007), p. 021403.
- [113] R. Wittkowski and H. Löwen, *Mol. Phys.* 109 (2011), pp. 2935–2943.
- [114] S. van Teeffelen, C.N. Likos, N. Hoffmann, and H. Löwen, *Europhys. Lett.* 75 (2006), pp. 583–589.
- [115] J.L. Barrat, *Europhys. Lett.* 3 (1987), pp. 523–526.
- [116] J.L. Barrat, J.P. Hansen, and G. Pastore, *Phys. Rev. Lett.* 58 (1987), pp. 2075–2078.
- [117] J.L. Barrat, J.P. Hansen, and G. Pastore, *Mol. Phys.* 63 (1988), pp. 747–767.
- [118] R. van Roij, P. Bolhuis, B. Mulder, and D. Frenkel, *Phys. Rev. E* 52 (1995), pp. R1277–R1280.
- [119] C.N. Likos, N. Hoffmann, H. Löwen, and A.A. Louis, *J. Phys.: Condens. Matter* 14 (2002), pp. 7681–7698.
- [120] C.N. Likos, A. Lang, M. Watzlawek, and H. Löwen, *Phys. Rev. E* 63 (2001), p. 031206.
- [121] A.A. Louis, *Phil. Trans. R. Soc. Lond. A* 359 (2001), pp. 939–960.
- [122] W.A. Curtin and N.W. Ashcroft, *Phys. Rev. A* 32 (1985), pp. 2909–2919.
- [123] A.R. Denton and N.W. Ashcroft, *Phys. Rev. A* 39 (1989), pp. 4701–4708.
- [124] H. Hansen-Goos and K. Mecke, *J. Phys.: Condens. Matter* 22 (2010), p. 364107.

- [125] Y. Rosenfeld, M. Schmidt, H. Löwen, and P. Tarazona, *J. Phys.: Condens. Matter* 8 (1996), pp. L577–L581.
- [126] P. Tarazona, *Phys. Rev. Lett.* 84 (2000), pp. 694–697.
- [127] Y. Rosenfeld, *Phys. Rev. E* 50 (1994), pp. R3318–R3321.
- [128] M. von Smoluchowski, *Ann. Phys. (Leipzig)* 353 (1916), pp. 1103–1112.
- [129] S. van Teeffelen, C.N. Likos, and H. Löwen, *Phys. Rev. Lett.* 100 (2008), p. 108302.
- [130] H. Löwen, *J. Phys.: Condens. Matter* 13 (2001), pp. R415–R432.
- [131] H. Löwen, T. Beier, and H. Wagner, *Europhys. Lett.* 9 (1989), pp. 791–796.
- [132] H. Löwen, T. Beier, and H. Wagner, *Z. Phys. B* 79 (1990), pp. 109–118.
- [133] J.F. Lutsko, *Physica A* 366 (2006), pp. 229–242.
- [134] M. Oettel, S. Dorosz, M. Berghoff, B. Nestler, and T. Schilling, *Phys. Rev. E* 86 (2012), p. 021404.
- [135] S.R.d. Groot and P. Mazur, *Non-Equilibrium Thermodynamics*, 1st ed., Dover Publications, New York, 1984.
- [136] P.C. Martin, O. Parodi, and P.S. Pershan, *Phys. Rev. A* 6 (1972), pp. 2401–2420.
- [137] L.E. Reichl, *A Modern Course in Statistical Physics*, 2nd ed., Wiley, New York, 1998.
- [138] P.K. Galenko, D.A. Danilov, and V.G. Lebedev, *Phys. Rev. E* 79 (2009), p. 051110.
- [139] S. Majaniemi and M. Grant, *Phys. Rev. B* 75 (2007), p. 054301.
- [140] S. Majaniemi, M. Nonomura, and M. Grant, *Eur. Phys. J. B* 66 (2008), pp. 329–335.
- [141] B.P. Athreya, N. Goldenfeld, and J.A. Dantzig, *Phys. Rev. E* 74 (2006), p. 011601.
- [142] A. Jaatinen, C.V. Achim, K.R. Elder, and T. Ala-Nissila, *Phys. Rev. E* 80 (2009), p. 031602.
- [143] A. Jaatinen and T. Ala-Nissila, *J. Phys.: Condens. Matter* 22 (2010), p. 205402.
- [144] K. Wu, A. Adland, and A. Karma, *Phys. Rev. E* 81 (2010), p. 061601.
- [145] M. Greenwood, N. Provatas, and J. Rottler, *Phys. Rev. Lett.* 105 (2010), p. 045702.
- [146] M. Greenwood, J. Rottler, and N. Provatas, *Phys. Rev. E* 83 (2011), p. 031601.
- [147] K. Wu, M. Plapp, and P.W. Voorhees, *J. Phys.: Condens. Matter* 22 (2010), p. 364102.
- [148] R. Prieler, J. Hubert, D. Li, B. Verleye, R. Haberkern, and H. Emmerich, *J. Phys.: Condens. Matter* 21 (2009), p. 464110.
- [149] M.A. Choudhary, D. Li, H. Emmerich, and H. Löwen, *J. Phys.: Condens. Matter* 23 (2011), p. 265005.
- [150] M.A. Choudhary, J. Kundin, and H. Emmerich, *Philos. Mag. Lett.* (2012). Available at <http://www.tandfonline.com/doi/abs/10.1080/09500839.2012.686173>.
- [151] G.I. Tóth, G. Tegze, T. Pusztai, and L. Gránásy, *Phys. Rev. Lett.* 108 (2012), p. 025502.
- [152] P. Meakin, H. Metiu, R.G. Petschek, and D.L. Scalapino, *J. Chem. Phys.* 79 (1983), pp. 1948–1954.
- [153] R.G. Petschek and H. Metiu, *J. Chem. Phys.* 79 (1983), pp. 3443–3456.
- [154] A. Karma and W.J. Rappel, *Phys. Rev. E* 60 (1999), pp. 3614–3625.
- [155] D.J.B. Lloyd, B. Sandstede, D. Avitabile, and A.R. Champneys, *SIAM J. Appl. Dyn. Syst.* 7 (2008), pp. 1049–1100.
- [156] M.J. Robbins, A.J. Archer, U. Thiele, and E. Knobloch, *Phys. Rev. E* 85 (2012), p. 061408.
- [157] P.G. de Gennes, *Mol. Cryst. Liq. Cryst.* 12 (1971), pp. 193–214.
- [158] P.G. de Gennes and J. Prost, *The Physics of Liquid Crystals*, 2nd ed., Oxford University Press, Oxford, 1995.
- [159] H.R. Brand and K. Kawasaki, *J. Phys. C* 19 (1986), pp. 937–942.
- [160] R. Wittkowski, H. Löwen, and H.R. Brand, *Phys. Rev. E* 83 (2011), p. 061706.
- [161] P. Bolhuis and D. Frenkel, *J. Chem. Phys.* 106 (1997), pp. 666–687.
- [162] H. Löwen, *Phys. Rev. E* 50 (1994), pp. 1232–1242.
- [163] D. Frenkel, B.M. Mulder, and J.P. McTague, *Phys. Rev. Lett.* 52 (1984), pp. 287–290.
- [164] Th. Kirchhoff, H. Löwen, and R. Klein, *Phys. Rev. E* 53 (1996), pp. 5011–5022.
- [165] H. Löwen, *J. Chem. Phys.* 100 (1994), pp. 6738–6749.
- [166] H. Löwen, *Phys. Rev. Lett.* 72 (1994), pp. 424–427.
- [167] D.J. Cleaver, C.M. Care, M.P. Allen, and M.P. Neal, *Phys. Rev. E* 54 (1996), pp. 559–567.
- [168] H. Fukunaga, J.I. Takimoto, and M. Doi, *J. Chem. Phys.* 120 (2004), pp. 7792–7800.
- [169] L. Muccioli and C. Zannoni, *Chem. Phys. Lett.* 423 (2006), pp. 1–6.
- [170] S. Chandrasekhar, *Liquid Crystals*, 2nd ed., Cambridge University Press, Cambridge, 1992.
- [171] S. Yabunaka and T. Araki, *Phys. Rev. E* 83 (2011), p. 061711.

- [172] T. Hirouchi, T. Takaki, and Y. Tomita, *Comput. Mater. Sci.* 44 (2009), pp. 1192–1197.
- [173] S.M. Wise, C. Wang, and J.S. Lowengrub, *SIAM J. Numer. Anal.* 47 (2009), pp. 2269–2288.
- [174] C. Wang and S.M. Wise, *SIAM J. Numer. Anal.* 49 (2011), pp. 945–969.
- [175] Z. Hu, S.M. Wise, C. Wang, and J.S. Lowengrub, *J. Comp. Phys.* 228 (2009), pp. 5323–5339.
- [176] M. Cheng and J.A. Warren, *J. Comp. Phys.* 227 (2008), pp. 6241–6248.
- [177] G. Tegze, G. Bansel, G.I. Tóth, T. Pusztai, Z. Fan, and L. Gránásy, *J. Comp. Phys.* 228 (2009), pp. 1612–1623.
- [178] R. Backofen, A. Rätz, and A. Voigt, *Philos. Mag. Lett.* 87 (2007), pp. 813–820.
- [179] G.I. Tóth and G. Tegze, (2012), to be published.
- [180] Y. Shiwa, *Phys. Rev. E* 79 (2009), p. 013601.
- [181] D. Yeon, Z. Huang, K.R. Elder, and K. Thornton, *Philos. Mag.* 90 (2010), pp. 237–263.
- [182] G.F. Kendrick, T.J. Sluckin, and M.J. Grimson, *Europhys. Lett.* 6 (1988), pp. 567–572.
- [183] A. de Candia, E. Del Gado, A. Fierro, N. Sator, M. Tarzia, and A. Coniglio, *Phys. Rev. E* 74 (2006), p. 010403R.
- [184] M. Bestehorn and H. Haken, *Z. Phys. B* 57 (1984), pp. 329–333.
- [185] C. Kubstrup, H. Herrero, and C. Pérez-García, *Phys. Rev. E* 54 (1996), pp. 1560–1569.
- [186] P. Cremer, M. Marechal, and H. Löwen, *Europhys. Lett.* 99 (2012), p. 38005.
- [187] A.F. Demirörs, P.M. Johnson, C.M. van Kats, A. van Blaaderen, and A. Imhof, *Langmuir* 26 (2010), pp. 14466–14471.
- [188] S.J. Gerbode, U. Agarwal, D.C. Ong, C.M. Liddell, F. Escobedo, and I. Cohen, *Phys. Rev. Lett.* 105 (2010), p. 078301.
- [189] M. Marechal and M. Dijkstra, *Phys. Rev. E* 77 (2008), p. 061405.
- [190] T.J. Stasevich, H. Gebremariam, T.L. Einstein, M. Giesen, C. Steimer, and H. Ibach, *Phys. Rev. B* 71 (2005), p. 245414.
- [191] V.V. Hoang, *Nanotechnology* 20 (2009), p. 295703.
- [192] Y. Wang, X. Wang, and H. Wang, *Trans. Nonferrous Met. Soc. China* 16 (2006), pp. s327–s331.
- [193] M. Cheng, J. Kundin, D. Li, and H. Emmerich, *Philos. Mag. Lett.* 92 (2012), pp. 517–526.
- [194] H. Emmerich, *The Diffuse Interface Approach in Material Science: Thermodynamic Concepts and Applications of Phase-Field Models*, Lecture Notes in Physics Monographs M 73, Springer, Berlin, 2003, pp. 1–186.
- [195] S. Praetorius and A. Voigt, *Macromol. Theory Simul.* 20 (2011), pp. 541–547.
- [196] M. Rauscher, A. Domínguez, M. Krüger, and F. Penna, *J. Chem. Phys.* 127 (2007), p. 244906.
- [197] F. Penna, J. Dzubiella, and P. Tarazona, *Phys. Rev. E* 68 (2003), p. 061407.
- [198] D. Li, H.L. Yang, and H. Emmerich, *Coll. Polym. Sci.* 289 (2011), pp. 513–521.
- [199] R. Backofen, M. Gräf, D. Potts, S. Praetorius, A. Voigt, and T. Witkowski, *Multiscale Model. Simul.* 9 (2011), pp. 314–334.
- [200] H. Löwen, *J. Phys.: Condens. Matter* 15 (2003), pp. V1–V3.
- [201] A.J. Archer and M. Rauscher, *J. Phys. A* 37 (2004), pp. 9325–9333.
- [202] M. Haataja, L. Gránásy, and H. Löwen, *J. Phys.: Condens. Matter* 22 (2010), p. 360301.
- [203] M. Plapp, *Philos. Mag.* 91 (2011), pp. 25–44.
- [204] G.H. Fredrickson and K. Binder, *J. Chem. Phys.* 91 (1989), pp. 7265–7275.
- [205] N.A. Gross, M. Ignatiev, and B. Chakraborty, *Phys. Rev. E* 62 (2000), pp. 6116–6125.
- [206] M. Asta, C. Beckermann, A. Karma, W. Kurz, R. Napolitano, M. Plapp, G. Purdy, M. Rappaz, and R. Trivedi, *Acta Mater.* 57 (2009), pp. 941–971.
- [207] J.Q. Broughton and G.H. Gilmer, *J. Chem. Phys.* 84 (1986), pp. 5759–5768.
- [208] K.F. Kelton and A.L. Greer (eds.), *Nucleation in Condensed Matter: Applications in Materials and Biology*, 1st ed., Pergamon Press, Oxford, 2005.
- [209] A.L. Greer, A.M. Bunn, A. Tronche, P.V. Evans, and D.J. Bristow, *Acta Mater.* 48 (2000), pp. 2823–2835.
- [210] K. Sandomirski, E. Allahyarov, H. Löwen, and S. Egelhaaf, *Soft Matter* 7 (2011), pp. 8050–8055.
- [211] Z.F. Huang, K.R. Elder, and N. Provatas, *Phys. Rev. E* 82 (2010), p. 021605.
- [212] L.Q. Chen, Y. Wang, and A.G. Khachaturyan, *Philos. Mag. Lett.* 65 (1992), pp. 15–23.
- [213] Y. Wang and A.G. Khachaturyan, *Acta Mater.* 45 (1997), pp. 759–773.

- [214] J. Kundin, D. Raabe, and H. Emmerich, *J. Mech. Phys. Solids* 59 (2011), pp. 2082–2102.
- [215] A. Artemev, Y. Jin, and A.G. Khachatryan, *Acta Mater.* 49 (2001), pp. 1165–1177.
- [216] A. Artemev, Y. Jin, and A.G. Khachatryan, *Philos. Mag.* 82 (2002), pp. 1249–1270.
- [217] M. Ortiz and L. Stainier, *Comput. Methods Appl. Mech. Eng.* 171 (1999), pp. 419–444.
- [218] Y.U. Wang, Y.M. Jin, A.M. Cuitiño, and A.G. Khachatryan, *Acta Mater.* 49 (2001), pp. 1847–1857.
- [219] M. Koslowski, *J. Mech. Phys. Solids* 50 (2002), pp. 2597–2635.
- [220] J. Kundin, H. Emmerich, and J. Zimmer, *Philos. Mag.* 90 (2010), pp. 1495–1510.
- [221] F. Roters, D. Raabe, and G. Gottstein, *Acta Mater.* 48 (2000), pp. 4181–4189.
- [222] A. Ma and F. Roters, *Acta Mater.* 52 (2004), pp. 3603–3612.
- [223] F. Roters, P. Eisenlohr, L. Hantcherli, D.D. Tjahjanto, T.R. Bieler, and D. Raabe, *Acta Mater.* 58 (2010), pp. 1152–1211.
- [224] K.A. Wu and P.W. Voorhees, *Acta Mater.* 60 (2012), pp. 407–419.
- [225] D. Pilipenko, M. Fleck, and H. Emmerich, *Eur. Phys. J. Plus* 126 (2011), pp. 100/1–100/16.
- [226] F.F. Abraham, *Phys. Rev. Lett.* 77 (1996), pp. 869–872.
- [227] F. Cleri, S. Yip, D. Wolf, and S.R. Phillpot, *Phys. Rev. Lett.* 79 (1997), pp. 1309–1312.
- [228] S.J. Zhou, D.M. Beazley, P.S. Lomdahl, and B.L. Holian, *Phys. Rev. Lett.* 78 (1997), pp. 479–482.
- [229] M.J. Buehler and H. Gao, *Nature* 439 (2006), pp. 307–310.
- [230] J.A. Hauch, D. Holland, M.P. Marder, and H.L. Swinney, *Phys. Rev. Lett.* 82 (1999), pp. 3823–3826.
- [231] L.B. Freund, *Dynamic Fracture Mechanics*, 1st ed., Cambridge Monographs on Mechanics and Applied Mathematics, Vol. 2, Cambridge University Press, New York, 1998.
- [232] K.A. Wu and P.W. Voorhees, *Phys. Rev. B* 80 (2009), p. 125408.
- [233] M.J. Aziz, *J. Appl. Phys.* 53 (1982), pp. 1158–1168.
- [234] K.A. Jackson, K.M. Beatty, and K.A. Gudgel, *J. Cryst. Growth* 271 (2004), pp. 481–494.
- [235] M.J. Aziz and T. Kaplan, *Acta Metall.* 36 (1988), pp. 2335–2347.
- [236] P.K. Galenko, E.V. Abramova, D. Jou, D.A. Danilov, V.G. Lebedev, and D.M. Herlach, *Phys. Rev. E* 84 (2011), p. 041143.
- [237] J. Li, S. Sarkar, W.T. Cox, T.J. Lenosky, E. Bitzek, and Y. Wang, *Phys. Rev. B* 84 (2011), p. 054103.
- [238] A. Karma, personal communication.
- [239] S. Alexander and J. McTague, *Phys. Rev. Lett.* 41 (1978), pp. 702–705.
- [240] P.R. ten Wolde, M.J. Ruiz-Montero, and D. Frenkel, *Phys. Rev. Lett.* 75 (1995), pp. 2714–2717.
- [241] C. Desgranges and J. Delhommelle, *Phys. Rev. Lett.* 98 (2007), p. 235502.
- [242] G.I. Tóth, J.R. Morris, and L. Gránásy, *Phys. Rev. Lett.* 106 (2011), p. 045701.
- [243] O. Galkin and P.G. Vekilov, *Proc. Nat. Acad. Sci.* 97 (2000), pp. 6277–6281.
- [244] P.R. ten Wolde and D. Frenkel, *Science* 277 (1997), pp. 1975–1978.
- [245] J.F. Lutsko and G. Ncolis, *Phys. Rev. Lett.* 96 (2006), p. 046102.
- [246] T. Schilling, H.J. Schöpe, M. Oettel, G. Opletal, and I. Snook, *Phys. Rev. Lett.* 105 (2010), p. 025701.
- [247] T.H. Zhang and X.Y. Liu, *J. Am. Chem. Soc.* 129 (2007), pp. 13520–13526.
- [248] H.J. Schöpe, G. Bryant, and W. van Meegen, *Phys. Rev. Lett.* 96 (2006), p. 175701.
- [249] P. Dillmann, G. Maret, and P. Keim, *J. Phys.: Condens. Matter* 20 (2008), p. 404216.
- [250] W. Schommers, *Phys. Rev. A* 28 (1983), pp. 3599–3605.
- [251] J.P. Doye, D.J. Wales, F.H.M. Zetterling, and M. Dzugasov, *J. Chem. Phys.* 119 (2003), pp. 2792–2799.
- [252] O. Mishima and H.E. Stanley, *Nature* 392 (1998), pp. 164–168.
- [253] M. Shimoji, *Liquid Metals: An Introduction to the Physics and Chemistry of Metals in the Liquid State*, 1st ed., Academic Press, London, 1977.
- [254] M. Castro, *Phys. Rev. B* 67 (2003), p. 035412.
- [255] W.B. Russel, P.M. Chaikin, J. Zhu, W.V. Meyer, and R. Rogers, *Langmuir* 13 (1997), pp. 3871–3881.
- [256] A.T. Skjeltorp, *Phys. Rev. Lett.* 58 (1987), pp. 1444–1447.
- [257] L. Gránásy, G. Tegze, G.I. Tóth, F. Podmaniczky, and T. Pusztai, *Phase-field crystal modeling of nucleation, patterning, and early-stage growth in colloidal systems in two and three dimensions*, Abstract Booklet, TMS Annual Meeting, 14–18 February 2010, Seattle.
- [258] J. Maurer, P. Bouissou, B. Perrin, and P. Tabeling, *Europhys. Lett.* 8 (1989), pp. 67–72.
- [259] Z. Cheng, P.M. Chaikin, J. Zhu, W.B. Russel, and W.V. Meyer, *Phys. Rev. Lett.* 88 (2001), p. 015501.
- [260] I. Lee, H. Zheng, M.F. Rubner, and P.T. Hammond, *Adv. Mater.* 14 (2002), pp. 572–577.

- [261] C. Reichhardt and C.J. Olson, *Phys. Rev. Lett.* 88 (2002), p. 248301.
 [262] A. Mathur, A. Brown, and J. Erlebacher, *Langmuir* 22 (2006), pp. 582–589.
 [263] J. Sun, Y.Y. Li, H. Dong, P. Zhan, C.J. Tang, M.W. Zhu, and Z.L. Wang, *Adv. Mater.* 20 (2008), pp. 123–128.
 [264] N.V. Dziomkina, M.A. Hempenius, and G.J. Vancso, *Adv. Mater.* 17 (2005), pp. 237–240.
 [265] K. Dholakia, G. Spalding, and M. MacDonald, *Phys. World* 15 (2002), pp. 31–35.
 [266] M. Hermes, E.C.M. Vermolen, M.E. Leunissen, D.L.J. Vossen, P.D.J. van Oostrum, M. Dijkstra, and A. van Blaaderen, *Soft Matter* 7 (2011), pp. 4623–4628.
 [267] G.I. Tóth and L. Gránásy, (2012), to be published.
 [268] T.C. Lubensky, D. Petey, N. Currier, and H. Stark, *Phys. Rev. E* 57 (1998), pp. 610–625.
 [269] A.A. Verhoeff, R.H.J. Otten, P. van der Schoot, and H.N.W. Lekkerkerker, *J. Phys. Chem. B* 113 (2009), pp. 3704–3708.
 [270] J. Dzubiella, M. Schmidt, and H. Löwen, *Phys. Rev. E* 62 (2000), pp. 5081–5091.
 [271] J.A. Moreno-Razo, E.J. Sambriski, N.L. Abbott, J.P. Hernandez-Ortiz, and J.J. de Pablo, *Nature* 485 (2012), pp. 86–89.
 [272] T. Schilling and D. Frenkel, *J. Phys.: Condens. Matter* 16 (2004), pp. S2029–S2036.
 [273] A. Härtel and H. Löwen, *J. Phys.: Condens. Matter* 22 (2010), p. 104112.
 [274] R. Wittkowski, H. Löwen, and H.R. Brand, *Phys. Rev. E* 84 (2011), p. 041708.
 [275] C.G. Gray and K.E. Gubbins, *Theory of Molecular Fluids: Fundamentals*, 1st ed., Oxford University Press, Oxford, 1984.

Appendix. Coefficients in the PFC models for liquid crystals

A.1 PFC model for liquid crystals in 2D

In the contributions (94)–(96) of the local scaled excess free-energy density, the coefficients

$$A_1 = 8M_0^0(1), \quad A_2 = -2M_0^0(3), \quad A_3 = \frac{1}{8}M_0^0(5) \quad (\text{A1})$$

are associated with a gradient expansion of $\psi^2(\mathbf{r})$. These coefficients also appear in a different form in the original PFC model [26]. The further coefficients are given by [160,274]

$$B_1 = 4(M_{-1}^1(2) - M_1^0(2)), \quad (\text{A2})$$

$$B_2 = 2(M_1^1(2) - M_{-1}^2(2)), \quad (\text{A3})$$

$$B_3 = -M_{-2}^2(3) - M_2^0(3), \quad (\text{A4})$$

$$C_1 = 4M_0^1(1), \quad C_2 = M_0^1(3) - \frac{1}{2}M_{-2}^1(3), \quad C_3 = -M_{-2}^1(3), \quad (\text{A5})$$

and

$$D_1 = 2M_0^2(1), \quad D_2 = -M_0^2(3). \quad (\text{A6})$$

So far, all these coefficients can also be obtained by using the second-order Ramakrishnan-Yussouff functional for the excess free energy. The remaining coefficients, however, result from higher-order contributions in the functional Taylor expansion [160]. In third order, one obtains for the homogeneous terms the coefficients

$$E_1 = 32\hat{M}_{00}^{00}, \quad (\text{A7})$$

$$E_2 = 16(\hat{M}_{00}^{-11} + 2\hat{M}_{00}^{01}), \quad (\text{A8})$$

$$E_3 = 8(\hat{M}_{00}^{-22} + 2\hat{M}_{00}^{02}), \quad (\text{A9})$$

$$E_4 = 8(2\hat{M}_{00}^{-21} + \hat{M}_{00}^{11}) \quad (\text{A10})$$

and for the terms containing a gradient the coefficients

$$F_1 = 16(\tilde{M}_{01}^{-10} - 2\tilde{M}_{01}^{0-1} + \tilde{M}_{01}^{00}), \quad (\text{A11})$$

$$F_2 = 16(\tilde{M}_{01}^{-21} - \tilde{M}_{01}^{0-2} + \tilde{M}_{01}^{01} - \tilde{M}_{01}^{1-2}), \quad (\text{A12})$$

$$F_3 = -16(\tilde{M}_{01}^{-20} - \tilde{M}_{01}^{-21} - \tilde{M}_{01}^{01} + \tilde{M}_{01}^{10}), \quad (\text{A13})$$

$$F_4 = -8(\tilde{M}_{01}^{-1-1} - 2\tilde{M}_{01}^{-11} + \tilde{M}_{01}^{1-1}), \quad (\text{A14})$$

$$F_5 = -4(\tilde{M}_{01}^{-2-1} - \tilde{M}_{01}^{-22} - \tilde{M}_{01}^{-12} + \tilde{M}_{01}^{2-1}), \quad (\text{A15})$$

$$F_6 = 8(\tilde{M}_{01}^{-22} - \tilde{M}_{01}^{-1-2} + \tilde{M}_{01}^{-12} - \tilde{M}_{01}^{2-2}). \quad (\text{A16})$$

In fourth order, only homogeneous terms are kept. The corresponding coefficients are

$$G_1 = 128 \hat{M}_{000}^{000}, \quad (\text{A17})$$

$$G_2 = 192(\hat{M}_{000}^{-101} + \hat{M}_{000}^{001}), \quad (\text{A18})$$

$$G_3 = 96(\hat{M}_{000}^{-202} + \hat{M}_{000}^{002}), \quad (\text{A19})$$

$$G_4 = 96(2\hat{M}_{000}^{-201} + \hat{M}_{000}^{-211} + \hat{M}_{000}^{011}), \quad (\text{A20})$$

$$G_5 = 48(\hat{M}_{000}^{-212} + \hat{M}_{000}^{-112}), \quad (\text{A21})$$

$$G_6 = 48\hat{M}_{000}^{-111}, \quad (\text{A22})$$

$$G_7 = 12\hat{M}_{000}^{-222}. \quad (\text{A23})$$

All the coefficients from above are linear combinations of moments of the Fourier expansion coefficients of the direct correlation functions. These moments are defined through

$$\mathbf{M}_{\mathbf{p}}^{\mathbf{m}^n}(\boldsymbol{\alpha}^n) = \pi^{2n+1} \rho_{\text{ref}}^{n+1} \left(\prod_{i=1}^n \int_0^\infty dr_i r_i^{\alpha_i} \right) \tilde{c}_{\mathbf{p}, \mathbf{m}^n}^{(n+1)}(\mathbf{r}^n) \quad (\text{A24})$$

with the multi-index notation $\mathbf{X}^n = (X_1, \dots, X_n)$ for $X \in \{l, m, r, 1, \alpha, \phi, \phi_R\}$ and the abbreviations $\hat{M}_{\mathbf{p}}^{\mathbf{m}^n} = M_{\mathbf{p}}^{\mathbf{m}^n}(\mathbf{1}^n)$ and $\tilde{M}_{l_1 l_2}^{m_1 m_2} = M_{l_1 l_2}^{m_1 m_2}(1, 2)$. The expansion coefficients of the direct correlation functions are given by

$$\tilde{c}_{\mathbf{p}, \mathbf{m}^n}^{(n+1)}(\mathbf{r}^n) = \frac{1}{(2\pi)^{2n}} \int_0^{2\pi} d\phi_{\mathbf{R}}^n \int_0^{2\pi} d\phi^n c^{(n+1)}(\mathbf{r}^n, \phi_{\mathbf{R}}^n, \phi^n) e^{-i(\mathbf{l}^n \cdot \phi_{\mathbf{R}}^n + \mathbf{m}^n \cdot \phi^n)} \quad (\text{A25})$$

with $\mathbf{r}_1 - \mathbf{r}_{i+1} = R_i \hat{\mathbf{u}}(\varphi_{R_i})$, $\hat{\mathbf{u}}_i = \hat{\mathbf{u}}(\varphi_i)$, $\phi_{R_i} = \varphi_1 - \varphi_{R_i}$, and $\phi_i = \varphi_1 - \varphi_{i+1}$.

When the system is apolar, the modulus $P(\mathbf{r})$ of the polarization $\mathbf{P}(\mathbf{r})$ is zero and its orientation $\hat{\mathbf{p}}(\mathbf{r})$ is not defined, while the direction $\hat{\mathbf{n}}(\mathbf{r})$ associated with quadrupolar order still exists. Then, symmetry considerations lead to the equalities

$$\tilde{c}_{-1,1}^{(2)}(R) = \tilde{c}_{1,0}^{(2)}(R), \quad \tilde{c}_{-1,2}^{(2)}(R) = \tilde{c}_{1,1}^{(2)}(R), \quad \tilde{c}_{-2,2}^{(2)}(R) = \tilde{c}_{2,0}^{(2)}(R) \quad (\text{A26})$$

between expansion coefficients of the direct pair-correlation function and to the equations

$$M_{-1}^1(2) = M_1^0(2), \quad M_{-1}^2(2) = M_1^1(2), \quad M_{-2}^2(2) = M_2^0(2) \quad (\text{A27})$$

for the generalized moments. A consequence of these equations is that the coefficients B_1 and B_2 vanish and B_3 becomes more simple.

A.2 PFC model for liquid crystals in 3D

The coefficients in Equation (105) appear in three different groups. The first group consists of the three coefficients

$$A_1 = 8 \Omega_{000}(0), \quad A_2 = -\frac{4}{3} \Omega_{000}(2), \quad A_3 = \frac{1}{15} \Omega_{000}(4), \tag{A28}$$

that are already known from the original PFC model [26] and belong to the gradient expansion of the translational density. In the next group, the two coefficients

$$B_1 = \frac{16}{15\sqrt{5}} \Omega_{220}(0), \quad B_2 = -\frac{16}{15} \Omega_{022}(2), \tag{A29}$$

that go along with the nematic tensor and the coupling of its gradient with the gradient of the translational density, are collected. The last group contains the Frank constants

$$\tilde{K}_1 = \frac{16}{15} \sqrt{\frac{2}{35}} \Omega_{222}(2), \quad \tilde{K}_2 = \frac{8}{45\sqrt{5}} \Omega_{220}(2) + \frac{1}{3} \tilde{K}_1, \tag{A30}$$

that appear in the Frank free-energy density [158,170]. All these coefficients are expressed in terms of the generalized moments

$$\Omega_{l_1 l_2 l}(n) = \pi^{3/2} \rho_{\text{ref}}^2 \int_0^\infty dr r^{n+2} \omega_{l_1 l_2 l}(r) \tag{A31}$$

with the expansion coefficients

$$\begin{aligned} \omega_{l_1 l_2 l}(r) &= \sqrt{\frac{4\pi}{2l+1}} \sum_{m=-\min\{l_1, l_2\}}^{\min\{l_1, l_2\}} C(l_1, l_2, l, m, -m, 0) \\ &\times \int d\hat{\mathbf{u}}_1 \int d\hat{\mathbf{u}}_2 c^{(2)}(r\hat{\mathbf{e}}_3, \hat{\mathbf{u}}_1, \hat{\mathbf{u}}_2) \bar{Y}_{l_1 m}(\hat{\mathbf{u}}_1) \bar{Y}_{l_2 -m}(\hat{\mathbf{u}}_2), \end{aligned} \tag{A32}$$

where the symbol $C(l_1, l_2, l, m_1, m_2, m)$ denotes a Clebsch-Gordan coefficient [275], $Y_{lm}(\hat{\mathbf{u}})$ is a spherical harmonic, $\hat{\mathbf{e}}_3$ stands for the Cartesian unit vector co-directional with the x_3 -axis, and $\bar{\cdot}$ denotes complex conjugation.

As before, equalities between generalized moments with different index-combinations, that can be derived using symmetry considerations [68], have been taken into account in order to reduce the set of generalized moments in Equation (105) to its seven independent members.